

STRENGTHENING OF L-SHAPED COMPOSITE LAMINATES USING  
CARBON NANOTUBE REINFORCEMENT AND  
THIN PLY NON-CRIMP FABRICS

A THESIS SUBMITTED TO  
THE GRADUATE SCHOOL OF NATURAL AND APPLIED SCIENCES  
OF  
MIDDLE EAST TECHNICAL UNIVERSITY

BY

MIRAY AYDAN ARCA

IN PARTIAL FULFILLMENT OF THE REQUIREMENTS  
FOR  
THE DEGREE OF MASTER OF SCIENCE  
IN  
AEROSPACE ENGINEERING

SEPTEMBER 2014



Approval of the thesis:

**STRENGTHENING OF L-SHAPED COMPOSITE LAMINATES USING  
CARBON NANOTUBE REINFORCEMENT AND THIN PLY NON-CRIMP  
FABRICS**

submitted by **MİRAY AYDAN ARCA** in partial fulfillment of the requirements for  
the degree of **Master of Science in Aerospace Engineering Department, Middle  
East Technical University** by,

Prof. Dr. Canan Özgen  
Dean, Graduate School of **Natural and Applied Sciences**

Prof. Dr. Ozan Tekinalp  
Head of Department, **Aerospace Engineering**

Assoc. Prof. Dr. Demirkan Çöker  
Supervisor, **Aerospace Engineering Dept., METU**

Assoc. Prof. Dr. Melih Papila  
Co-Supervisor, **Materials Science & Engineering, Sabanci Uni.**

**Examining Committee Members**

Prof. Dr. Altan Kayran  
Aerospace Engineering Dept., METU

Assoc. Prof. Dr. Demirkan Çöker  
Aerospace Engineering Dept., METU

Prof. Dr. Levend Parnas  
Mechanical Engineering Dept., METU

Assoc. Prof. Dr. Melih Papila  
Materials Science & Engineering, Sabanci Uni.

Assist. Prof. Dr. Ercan Gürses  
Aerospace Engineering Dept., METU

Date: 05.09.2014

**I hereby declare that all information in this document has been obtained and presented in accordance with academic rules and ethical conduct. I also declare that, as required by these rules and conduct, I have fully cited and referenced all material and results that are not original to this work.**

Name, Last name: Miray Aydan Arca

Signature:

## ABSTRACT

### STRENGTHENING OF L-SHAPED COMPOSITE LAMINATES USING CARBON NANOTUBE REINFORCEMENT AND THIN PLY NON-CRIMP FABRICS

Arca, Miray Aydan

M.S., Department of Aerospace Engineering

Supervisor: Assoc. Prof. Dr. Demirkan Çöker

Co-Supervisor: Assoc. Prof. Dr. Melih Papila

September 2014, 99 pages

The advances in manufacturing technologies have increased the use of composite materials in complex shapes such as curved beams. However, use of composites in complex geometries creates a weakness at the curvature and causes delamination failure. Major objective is to provide solution for this problem without degrading properties or increasing the weight of the structure. In this study, the effect of CNTs in the resin and the use of non-crimp fabric on the fracture toughness and curved beam strength of laminates are investigated experimentally. Curved beam composite laminates were subjected to four-point bending loading according to ASTM D6415. Double cantilever beam (DCB) tests and end notch flexure (ENF) tests were conducted to determine mode-I and mode-II fracture toughness, respectively. In the first part, mode-I and mode-II fracture toughness of 3% CNT added laminates are found to be 25% and 10% higher, respectively, compared to prepreg-fabric laminates. However, detrimental effect on the curved beam strength was found. In the second part, changing the material type from unidirectional to thin-ply non-crimp fabric material increased the mode I, mode II fracture toughness and curved beam strength of the laminates. It is observed that the manufacturing defects are the potential failure initiation sides.

**Keywords:** composite materials, fracture mechanics, carbon nanotubes, polymer nanofibers, non-crimp fabric.

## ÖZ

### L-SEKİLLİ KOMPOZİT LAMİNANLARIN KARBON NONOTÜP VE İNCE KATMAN DOKUSUZ KUMASLARLA GÜÇLENLENDİRİLMESİ

Arca, Miray Aydan

Yüksek Lisans, Havacılık ve Uzay Mühendisliği

Tez Yöneticisi: Doç. Dr. Demirkan Çöker

Yardımcı Tez Yöneticisi: Doç Dr. Melih Papila

Eylül 2014, 99 sayfa

Üretim teknolojilerindeki gelişim ile birlikte kompozit malzemelerin bükümlü yapılar gibi kompleks şekillerde kullanımını arttırmaktadır. Bununla beraber, kompozitlerin bükümlü yapılarda kullanılması bükümlü bölgede zayıflık yaratarak delaminasyona neden olmaktadır. Bu çalışmadaki temel amaç bu probleme malzeme özelliklerinde kayba neden olmayan ya da ağırlığı arttırmayan çözüm yöntemleri araştırmaktır. Bu çalışmada reçinesine Karbon Nanotüp eklenmiş kompozit malzemelerin ve ince katmanlı dokusuz karbon fiber kompozit malzemelerin bükümlü kiriş deneyleri ve kırılma tokluğu deneyleri yapılarak güçlendirmeye etkileri deneysel olarak araştırılmıştır. Reçinesine %3 KNT eklenmiş laminantların Mod-I ve Mod-II kırılma tokluğunun benzer örgü laminantlara göre sırasıyla %25 ve %10 daha fazla olduğu gözlemlenmiştir. Bununla birlikte bükümlü kiriş dayanımına etkileri üretim ve malzeme farklılıkları nedenleriyle tam olarak anlaşılabilmiştir. Ayrıca, malzeme yapısının ince katmanlı dokusuz malzemeyle değiştirilmesinin mod-I ve mod II kırılma tokluğunu ve bükümlü kiriş dayanımını arttırdığı, üretim sırasında oluşan kusurların potansiyel kırılma yerlerini oluşturduğu hızlı kameralarla gözlemlenmiştir. Kusurlu numunelerde yük taşıma kapasitesi yüksek olsa dahi kırılma mekanizmasının kompleks hale geldiği saptanmıştır.

**Anahtar Kelimeler:** kompozit malzemeler, çatlak mekaniği, karbon nanotüp, polimer nanofiber, non-crimp fabric

I would like to dedicate my thesis to my mother, Afet.

## ACKNOWLEDGEMENTS

First and most of all, I would like to thank my advisor Dr. Demirkan Coker for his expertise, assistance, guidance and patience throughout my studies. I would like to thank my advisor Dr. Melih Papila for his motivation and scientific contributions and supports to my studies.

I would like to thank Dr. Ercan Gürses, Dr. Levend Parnas, Dr. Altan Kayran and for their critics and suggestions in my thesis committee. I would like to thank Kubilay Demiralan from TAI for his great effort to have our specimens manufactured at all cost. I would like to thank Irfan Karaali form METKON for his support and effort for microscopic studies. I also would like to thank Nanografi Company for providing materials for CNT studies. I would like to thank Asst. Prof. Oguz Uzol and Ruzgem for their help and support to our studies.

I would like to thank Coker Group, Imren Uyar, Başar Kütükoğlu, Burak Gözlüklü, Denizhan Yavaş and Aydın Amireghbali. It was a great pleasure to work with them.

I would like to thank Imren Uyar and Emre Yilmaz for their friendship, encouragement, help and support for all sleepness nights. I also give special thanks to Erman Ataygöl for his support, encouragement, help and love for all the time.

I would like to acknowledge the Ministry of Science, Industry and Technology and Turkish Aerospace Industries (TAI) (Grant# 00785.STZ.2011-1) for the financial support of this work.

## TABLE OF CONTENTS

ABSTRACT.....	v
ÖZ.....	vi
ACKNOWLEDGEMENTS.....	viii
TABLE OF CONTENTS.....	ix
LIST OF TABLES.....	xii
LIST OF FIGURES.....	xiii
LIST OF SYMBOLS.....	xxvii
ABBREVIATIONS.....	xxxiv
CHAPTERS	
1. INTRODUCTION.....	1
1.1. Applications of curved composite laminates.....	1
1.2. Delamination Failure of Curved Composite Laminates.....	3
1.2.1. Loads on Curved Composite laminates.....	3
1.2.2. Delamination Problem of Curved Composite laminates ...	4
1.2.3. Relations between Curved Beam Strength and Delamination Initiation.....	6
1.2.4. Relations between Fracture Toughness and Delamination Growth.....	7
1.3. Two Approaches to Strengthen L-Shaped Laminates.....	7
1.3.1. Carbon Nanotubes.....	8
1.3.2. Novel Material – Thin Ply Non-Crimp Fabric.....	13

1.4.	Scope of the Study .....	15
2.	EXPERIMENTAL METHOD.....	17
2.1.	Fracture Toughness Test.....	17
2.1.1.	DCB Test for Mode-I Fracture Toughness .....	17
2.1.2.	Mode-II Fracture Toughness Test .....	24
2.2.	Four Point Bending Test for Curved Beam Strength.....	29
2.2.1.	Experimental Setup and Procedure.....	29
2.2.2.	Frictional Effects on 4-Point Bending Tests.....	30
2.2.3.	Curved Beam Strength Calculation .....	32
3.	EFFECT OF CARBON NANOTUBES ON THE FRACTURE TOUGHNESS AND CURVED BEAM STRENGTH OF FABRIC COMPOSITE LAMINATES .....	35
3.1.	Specimen Preparation .....	35
3.1.1.	Material.....	35
3.1.2.	Specimen Geometry.....	38
3.1.3.	Manufacturing: .....	39
3.2.	Prepreg-Fabric Laminates.....	42
3.2.1.	Mode-I Fracture Toughness.....	42
3.2.2.	Mode-II Fracture Toughness .....	43
3.2.3.	Curved Beam Strength.....	44
3.3.	CNT-Fabric Laminates: .....	49
3.3.1.	Mode-I Fracture Toughness.....	49
3.3.2.	Mode-II Fracture Toughness .....	51
3.3.3.	Curved Beam Strength.....	52
3.4.	Discussion.....	55
3.4.1.	Fracture Toughness Results.....	55
3.4.2.	Curved Beam Strength Results .....	57

3.4.3. Final Discussions .....	59
<b>4. COMPARISON OF THE FAILURE OF THIN PLY NON-CRIMP FABRIC AND UNIDIRECTIONAL LAMINATES .....</b>	<b>61</b>
4.1. Specimen Preparation .....	61
4.1.1. Material.....	61
4.1.2. Specimen Geometry .....	64
4.1.3. Manufacturing: .....	65
4.2. [0] and [0/45/-45/0] Unidirectional Laminates .....	67
4.2.1. Mode-I Fracture Toughness.....	67
4.2.2. Mode-II Fracture Toughness .....	69
4.2.3. Curved beam strength.....	70
4.3. [0/45/-45/0] Thin Ply NCF .....	78
4.3.1. Mode-I Fracture Toughness.....	78
4.3.2. Mode-II Fracture Toughness .....	79
4.3.3. Curved Beam Strength.....	80
4.4. Results and discussions.....	85
4.4.1. Fracture Toughness Results.....	85
4.4.2. Curved Beam Strength Results.....	86
<b>5. SUMMARY AND CONCLUSIONS .....</b>	<b>89</b>
5.1. Summary.....	89
5.2. Conclusions.....	90
5.3. Future Work.....	92
<b>REFERENCES .....</b>	<b>95</b>

## LIST OF TABLES

### TABLES

Table 1 Advantages and disadvantages of available test method to determine the Mode-II fracture toughness .....	24
Table 2 AS4/8552 PrepregLaminate Properties .....	36
Table 3 Properties of NANOCYL™ NC7000 CNTs [2] .....	37
Table 4 Dimensions and number of specimens used in each type of tests.....	39
Table 5 properties of thin ply NCF .....	62
Table 6 properties of [0] unidirectional fiber .....	62

## LIST OF FIGURES

### FIGURES

Figure 1 Types of materials used in 787 aircraft structure in weight percent [6].	2
Figure 2 Applications of curved composite laminates (a) in wing internal structure [10] (b) wind turbine blade internal structure [8].	3
Figure 3(a) Types of loads applied on a typical rib box structure [9] (b) reaction forces on the curved section of the composite laminate.	4
Figure 4 Sources of delamination failure of composite materials [14].	5
Figure 5 (a) Reaction forces and stress state on the curved region, (b) representation of the contributions of opening, shear and longitudinal stresses leading to delamination.	6
Figure 6 Fracture modes (a) Mode-I (opening), (b) Mode-II (sliding shear) and (c) Mode-III tearing	7
Figure 7 Example TEM photo of a multi walled CNT with outside diameter, inside diameter and wall thickness indicated [23].	8
Figure 8 Example products of CNT applications [22]	10
Figure 9 (a) Schematic of methodology to distribute the fibers, (b) carbon fiber tows before spreading 6mm in width, after spreading 12 mm and 20 mm in width [44].	14
Figure 10 (a) plain weave spread tow fabric, (b) thin ply NCF	14
Figure 11 Experimental Setup of double cantilever beam test	18
Figure 12 Load-Displacement curve of brittle matrix CRFP from the DCB test	19
Figure 13 Two cantilever beam assumption representation of DCB specimen.	21
Figure 14 MBT correction line, $\Delta$ represents the intersection point of linear fit curve of $C^{1/3}$ - a plot and horizontal axis	21
Figure 15 CC correction line	22
Figure 16 MCC correction line.	23
Figure 17 (a) experimental test setup, (b) specimen geometry of ENF test.	25
Figure 18 ENF test results with no precrack and Mode-I precracks	26
Figure 19 the three parts of deflection of the ENF specimen defined as $\Delta_a$ , $\Delta_b$ , $\Delta_c$ .	26
Figure 20 division of the specimen into 4 regions.	27

Figure 21 (a) positioning of the specimen in the setup, (b) experimental test Setup with high speed camera system.....	29
Figure 22 . Two types of setups used in 4-point bending tests with: (a) bottom part not allowing free rotation of the rollers, (b) bottom part with rollers allowed to freely rotate.....	30
Figure 23 4-point bending test load-displacement curves for 48-ply UD, 12-ply thin ply NCF and 6-ply thin ply NCF: (a) original curves for frictional bottom rollers (thin lines) and friction free bottom rollers (thick lines), (b) modified curves obtained by multiplying the stiffness by a constant of 1.34.....	31
Figure 24 Finite element model and boundary conditions for a 4-point bending test to investigate the effect of friction in the bottom rollers. ....	31
Figure 25 Load-displacement curves obtained from simulations for a friction coefficient of 0.3 representing frictional rollers (red line) and 0.001 representing rolling friction (black line). ....	32
Figure 26 TEM images of NANOCYL™ NC7000 series thin walled CNTs.....	37
Figure 27 Viscosity change of neat base resin and master batch with temperature [3] .....	38
Figure 28 Specimen geometry of prepreg-fabric and CNT added material used for fracture toughness tests and 4-point bending tests .....	39
Figure 29 Laid up preregs on the right handed male tool. ....	40
Figure 30 (a) Placements of release film and breather fabric on the tool (b) vacuum bagging process. ....	40
Figure 31 Temperature and pressure treatment curves for autoclave. ....	41
Figure 32 microscopic view of (a) prepreg-fabric and (b) CNT added materials in the thickness directions. ....	41
Figure 33 DCB test load displacement curves of prepreg-fabric laminates.....	42
Figure 34 (a) Mode-I fracture toughness ( $G_{IC}$ ) initiation and propagation values obtained by MBT, CC and MBT methods (b) corresponding R-curve for prepreg-fabric laminates based on MBT method. ....	43
Figure 35 (a) ENF test Load displacement curves of prepreg-fabric laminates, (b) Mode-II fracture toughness results of prepreg-fabric laminates. ....	43
Figure 36 4-point bending test load displacement curves of three preregs-fabric specimens. ....	44

Figure 37 High speed camera images taken at 15,000 fps for the laminate prepreg-fabric1. ....	45
Figure 38 High speed camera images taken at 300,000 fps for the laminate prepreg-fabric3. ....	46
Figure 39 Micrograph of fracture surface of prepreg-fabric1 after the experiment showing cracked curved region.....	48
Figure 40 Micrograph of fracture surface of prepregs-fabric1 specimen after the experiment showing marked locations on the micrographs of cracked curved region .....	47
Figure 41 DCB test load displacement curves of CNT-fabric laminates.....	49
Figure 42 (a) Mode-I fracture toughness ( $G_{IC}$ ) initiation and propagation values obtained by MBT, CC and MBT methods (b) corresponding R-curve for CNT-prepreg laminates based on MBT. ....	50
Figure 43 SEM images of CNT-fabric2 specimen after DCB test showing (a) general view of fracture surface, (b) closer look at the epoxy region showing the agglomerated CNTs and (c) CNT bridging at the crack tip. ....	50
Figure 44 (a) ENF test Load displacement curves of CNT-fabric laminates, (b) Mode-II fracture toughness results of CNT-fabric laminates. ....	51
Figure 45 4-point bending test load displacement curves of three CNT-fabric specimens .....	52
Figure 46 High speed camera images at 28,000 fps for CNT added laminate at (a) first load drop and (b) second load drop. ....	53
Figure 47 Micrographs of fracture surface after the experiment showing CNT-fabric2 laminate.....	54
Figure 48 Load displacement curves of prepreg-fabric and CNT-fabric laminates obtained from (a) DCB test and (b) ENF test .....	55
Figure 49 $G_{IC}$ Resistance curves for (a) prepreg-fabric and (b) CNT-fabric laminates. ....	56
Figure 50 (a) Mod- I fracture toughness initiation and propagation values (b) Mode-II fracture toughness values of prepreg-fabric and CNT-fabric laminates. ....	57
Figure 51 SEM images of fracture surfaces after DCB test for (a) for prepreg-fabric and (b) CNT-fabric laminates, arrow indicates the crack growth direction.....	57

Figure 52 Load displacement curves of 4-pt bending test for prepreg-fabric and CNT-fabric laminates together.....	58
Figure 53 (a) Curved beam strength, (b) maximum radial stress results of prepreg-fabric and CNT-fabric laminates together.....	59
Figure 54 photos of the prepreg-fabric <sup>3</sup> and CNT <sup>3</sup> laminates after the test showing the cracked curved regions (a) prepreg-fabric specimen, (b) CNT-fabric specimen.	60
Figure 55 (a) Tow spreading device, (b) schematic of tow-spreading process [4] ....	63
Figure 56 (a) The schematic of the machine forming plies in the 45 <sup>0</sup> direction and (b) thin plies obtained with the tow spreading technology at Chomarar. ....	63
Figure 57 Ply combining process schematic of thin ply NCF laminates during manufacturing.....	64
Figure 58 Specimen geometry of thin fiber NCF used for (a) 4-point bending tests and (b) fracture toughness tests.....	65
Figure 59 Tools used for manufacturing of (a) first batch, (b) second batch.....	65
Figure 60 (a) Laid up thin fiber prepregs on the tool used for first batch, (b) oven used for curing process for laid up prepregs in vacuum bag.....	66
Figure 61 Microscopic view of [0/45/-45/0] thin ply NCF (a) in the thickness direction, (b) in the width directions. ....	66
Figure 62 DCB load displacement curves of three tests of (a) [0] UD and two tests of (b) [0/45/-45/0] UD laminates.....	68
Figure 63 Bar graph of Mode-I fracture toughness ( $G_{Ic}$ ) initiation and propagation values obtained by MBT, CC and MCC methods (a) for [0] UD and (c) for [0/45] UD laminates, corresponding resistance curves obtained by MBT (b) for [0] UD laminates and (d) for [0/45] UD laminates.....	69
Figure 64 ENF test load displacement curves of (a) [0] UD laminates, (b) [0/45] UD laminates and (c) bar graph of Mode-II fracture toughness values for [0] UD and [0/45] UD laminates calculated by direct beam theory.....	70
Figure 65 4-point bending test load displacement curves of [0] UD laminates. ....	71
Figure 66 [0] UD specimen HSC photos corresponding to each load drop marked on the load displacement curve. ....	72
Figure 67 4-point bending test load displacement curves of [0/45] UD laminates....	73
Figure 68 Front and back side photos of (a) 2 <sup>nd</sup> and (b) 3 <sup>rd</sup> specimen before and after test. ....	74

Figure 69 [0/45] UD specimen HSC photos taken at 35000 fps corresponding to each load drop marked on the load displacement curve. ....	75
Figure 70 (a) 4 pt bending test load displacement curve of test1 indicating 1 <sup>st</sup> and 2 <sup>nd</sup> load drops, (b) and (c) corresponding HSC photos taken at 100,000 fps . ....	77
Figure 71 (a) 4 pt bending test load displacement curve of batch2 test2 [0/-45/45/0]7T UD and HSC photos corresponding to (b)1st load drop (1), (c) region 2, (d) region 3 e, (e) region 4 corresponding to small load drop, (f) 2nd load drop (5). 77	77
Figure 72 DCB load displacement curves of three tests for [0/45] thin ply NCF laminates. ....	78
Figure 73 Bar graph of Mode-I fracture toughness ( $G_{Ic}$ ) initiation and propagation values obtained by MBT, CC and MCC methods for thin ply NCF laminates, (b) corresponding resistance curves obtained by MBT. ....	79
Figure 74 (a) ENF test load displacement curves of thin ply NCF laminates and (b) bar graph of Mode-II fracture toughness values for TPNCf calculated by DBT. ....	79
Figure 75 4-pt bending test load displacement curves of [0/-45/45/0]12T thin ply NCF 1st and 2nd batch together. ....	80
Figure 76 Front and back side photos of (a) 1 <sup>st</sup> and (b) 3 <sup>rd</sup> specimen before and after test .....	81
Figure 77 TPNCf1 specimen HSC photos taken at 42500 fps. ....	82
Figure 78 High speed photos of TPNCf2 specimen 2 <sup>nd</sup> test (2 <sup>nd</sup> batch), taken at 100,000 fps showing the failure sequence. ....	83
Figure 79 High speed photos of TPNCf3 specimen 3 <sup>rd</sup> test (2 <sup>nd</sup> batch), taken at 300,000 fps showing the failure sequence. ....	83
Figure 80 Micrograph of curved region of TPNCf1 specimen after 4-pt bending test. ....	84
Figure 81 Load displacement curves of NCF, [0/45] UD and [0] UD laminates obtained (a) DCB tests and (b) ENF tests. ....	85
Figure 82 (a) Bar graph of Mode-I fracture toughness ( $G_{Ic}$ ) initiation and propagation values obtained by MBT and (b) bar graph of Mode-II fracture toughness values calculated by direct beam theory for TPNCf, [0] UD and [0/45] UD laminates. ....	86
Figure 83 Four point bending load displacement curves of [0] UD, [0/45] UD and [0/45] thin fiber NCF laminates all together. ....	87

Figure 84 Specimen photos taken before and after test showing the front and back sides of (a) [0]UD specimens, (b) [0/45/-45/0]UD specimens and (c) thin ply NCFspecimens. ....87

## CHAPTER 1

### INTRODUCTION

In this chapter applications of curved composite laminates in aerospace and wind turbine industries are briefly described. Then, loading types on curved composite laminates are defined for a typical wing rib section as an sample application and delamination problem of composite laminates is introduced. The relations between delamination initiation and curved beam strength, and delamination growth and fracture toughness of curved composite laminates are briefly discussed. Next, carbon nanotubes and thin ply non-crimp fabric type laminates are introduced as two approaches to strengthen L-shaped laminates and studies on carbon nanotubes and thin ply non-crimp fabric type laminates are presented. Finally, scope of the study is presented.

#### **1.1. Applications of curved composite laminates**

The term composite material indicates the physical combination of two or more materials having different macroscopic behavior resulting in new material system with superior properties than its constituents. Generally one of the constituents of composite materials which is weaker than other is called matrix phase and other stronger constituents embedded to the matrix phase are called reinforcement. The properties of the final material depend on the properties of its constituents, geometry and dispersion of the reinforcement [1, 2, 3, 4]. Advanced composite materials are generally consist of endless fibers embed in a polymer matrix which can be also called fiber reinforced plastics (FRP). These materials are obtained by stacking the layers (plies/laminates) together in the desired directions.

The concept of composite material dates back to Egyptians with the usage of bamboos as a reinforcement for mud walls and glued laminated woods. Likewise, plant fibers were used to strengthen the bricks and pottery in the ancient Inca and Mayan civilizations. In the 19<sup>th</sup> century steel reinforced structures were established with the iron rod reinforcement of masonries. Modern composite perception was

developed with the usage of the glass fibers as reinforcement in 1930s. In the 1960s development of boron and carbon fibers, composites were applied to the aerospace industry as an advanced materials. Since 1960 interest and demand on the composite materials increases gradually. While advanced composite material usage less than 2% in mass for F-15s in 1070s, in 1990s the usage of composite materials reached 30% in mass for AV-8B and presently new aircrafts have approximately 50% composite materials as shown in Figure 2 [1,2,4,5,7].

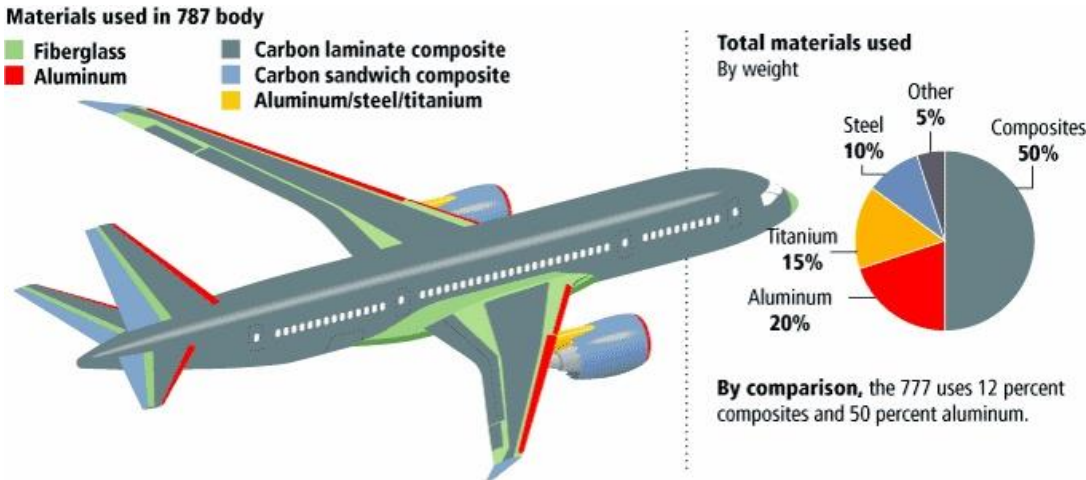


Figure 1 Types of materials used in 787 aircraft structure in weight percent [6].

This demand for composites especially in aircraft and wind turbine industries emerges from the need of light weight structures without any loss of strength and stiffness. Composite materials have superior properties compared to metallic materials such as improved strength, stiffness, fatigue and impact resistance, thermal conductivity, corrosion resistance, etc. [1]. Light weight structures with improved properties of composite materials satisfy the requirements of advanced technologies, leading to increase in the demand for these materials especially carbon fiber reinforced plastics (CFRP) for both industries.

Generally composites are widely used in aerospace and wind turbine structures as a plenary parts. Composite materials are incorporated into complex geometries and curved parts instead of metallic materials with the recent advanced manufacturing technologies. Rib and spar flanges of wing and spar sections of wind turbine blades

(Figure 2a and b) are the main applications of load carrying metallic structures replaced with curved composite materials [8,9,10].

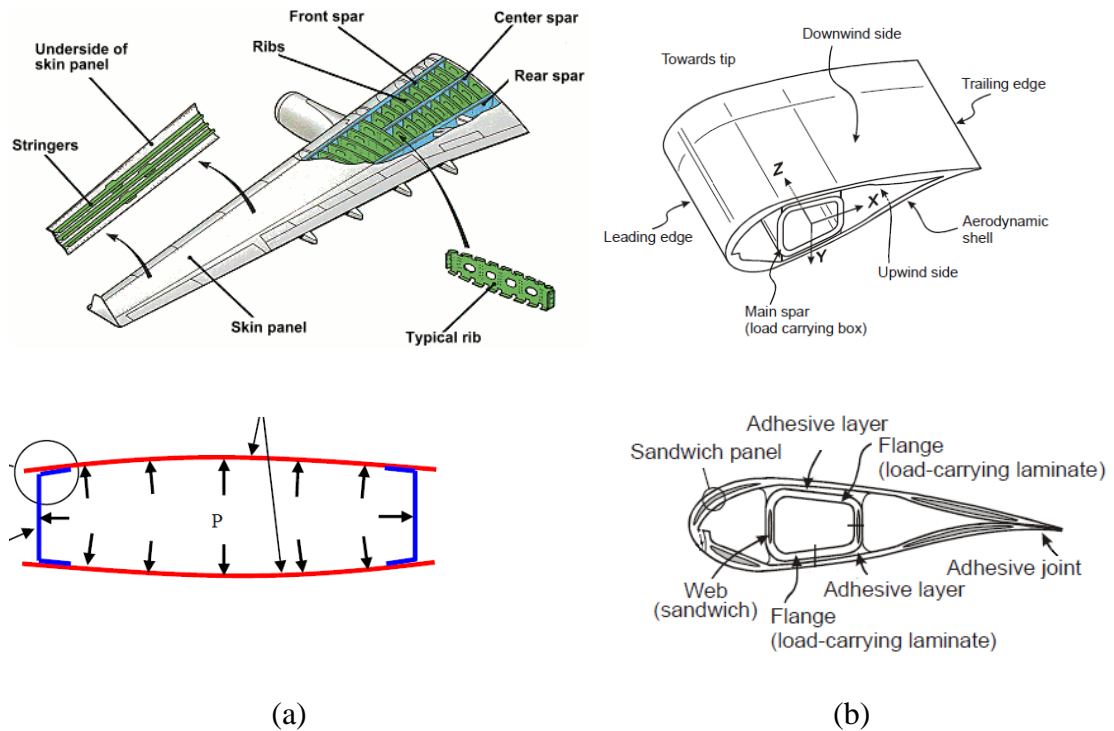


Figure 2 Applications of curved composite laminates (a) in wing internal structure [10] (b) wind turbine blade internal structure [8].

## 1.2. Delamination Failure of Curved Composite Laminates

### 1.2.1. Loads on Curved Composite laminates

Types of load applied on the typical wing rib section are shown in the Figure 3 and can be explained as follows [9]:

1. distributed pressure load at the sides due to the Air and fuel inside the box structure, resulting in moment load at the curved section
2. compression and tension loads in the chord wise direction due to the Poisson's ratio effect and end load at spars
3. concentrated loads due to the control surfaces or shear flows inside the wing, resulting in shear loads at the curved section
4. out of plane pressure loads due to the refuel overflow, creating axial and moment loads at the curved section
5. torsion loads due to the air flow during flight

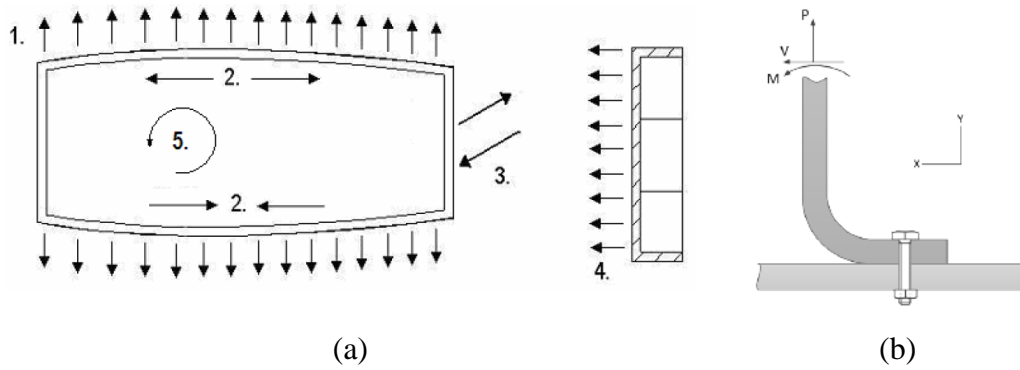


Figure 3(a) Types of loads applied on a typical rib box structure [9] (b) reaction forces on the curved section of the composite laminate.

Curved structures are subjected to three types of forces, namely shear, axial and moment forces (Figure 3b) which are created as a response of these complex loadings described above.

### 1.2.2. Delamination Problem of Curved Composite laminates

Generally three types of failure are observed for composites, namely microcracking, fiber breakage and delamination. Delamination is the most common source of failure of composites [14, 38]. Delamination is basically separation of layers, constraining cracks to grow in resin rich regions between the adjacent plies which can be explained as an interface crack [14].

Delamination is originated due to the mismatch in the properties of matrix and reinforcement of composite materials. Unbalanced properties of matrix and reinforcement creates out of plane stresses. There are a lot of geometrical sources that increases the out of plane stresses of laminated composite materials leading to delamination failure. Free edges, ply drops, interactions, solid-sandwich transitions and corner geometries are some examples of delamination sources as presented in Figure 4. Besides delaminations can also be originated during the manufacturing process or due to impact loadings [14].

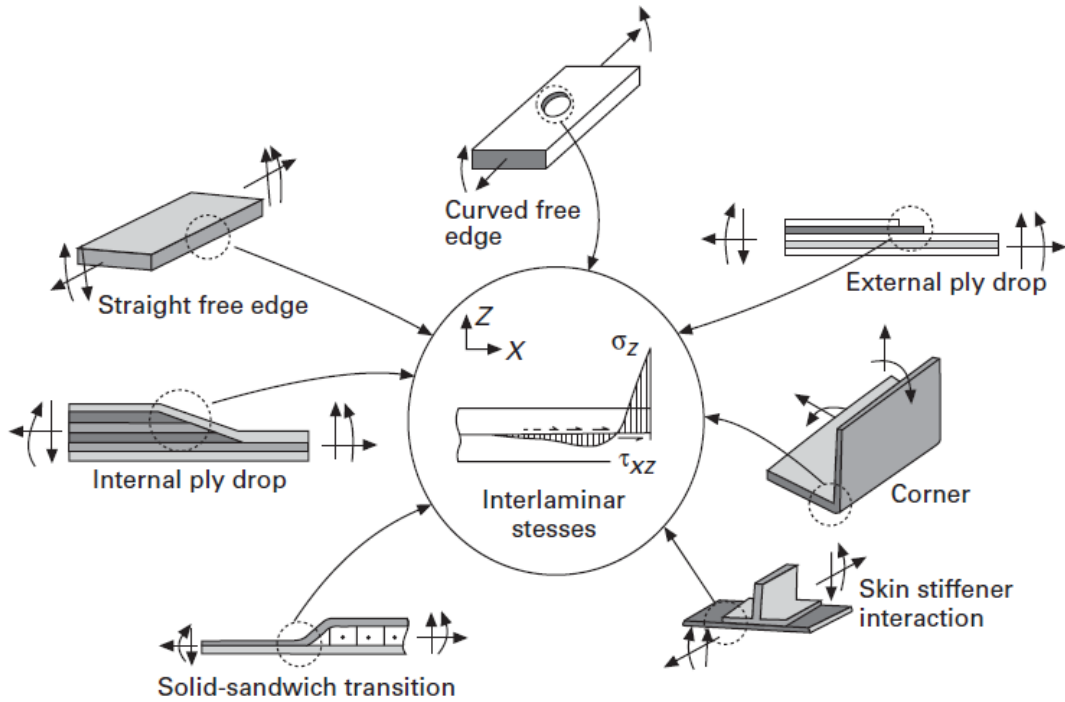


Figure 4 Sources of delamination failure of composite materials [14].

For the curved composite laminates very simple reaction forces namely, shear load, axial load and moment loads as shown in Figure 3b are created due to the external loads explained in section 1.2.1. Although these external loads on the box structure and reaction forces at the curved region are not problematic for metallic structures, for composite materials it is a big concern. Replacing the metal parts with the composite materials results in new structural difficulty, namely poor through thickness strength, which is not encountered with metals [10]. In contrast to the superior in plane properties, composite materials are weak in through the thickness directions due to the low properties of matrix rich regions and mismatch of properties of matrix and reinforcement. Normally unbalanced properties of matrix and reinforcement creates out of plane shear stresses which is common for plenary shapes, and new type of stress state, namely out of plane normal stresses, are originated from the radial geometry of the laminate [11]. Any of these simple reaction forces and their contributions creates out of plane normal stresses together with shear stresses at the curved region which are shown in the analytical model of anisotropic curved laminates driven by Lekhnitskii [12]. This complex stress state generates delamination failure which is separation of layers, constraining cracks to grow in resin rich regions as shown in Figure 5 [11].

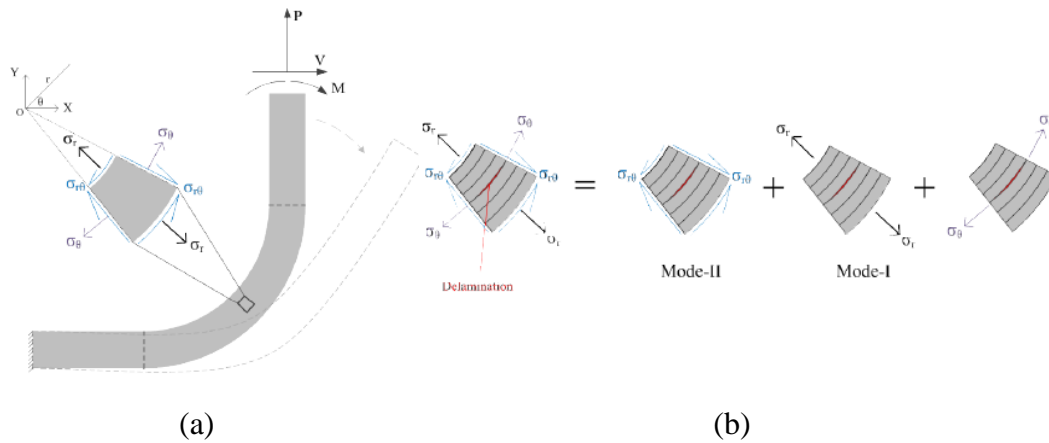


Figure 5 (a) Reaction forces and stress state on the curved region, (b) representation of the contributions of opening, shear and longitudinal stresses leading to delamination.

Delamination failure occurs in parts, firstly delamination initiation forms on the interface and then existing crack grows in the interface which is named as delamination propagation. Different approaches are used for delamination initiation and propagation analyses. While initiation stage is defined by strength of materials approach, propagation stage is defined by the fracture mechanics approach. Further discussions are presented in the sections 1.2.3 and 1.2.4 for initiation and propagation stages, respectively.

### 1.2.3. Relations between Curved Beam Strength and Delamination Initiation

When out of plane stresses at the curved region becomes equal to the through the thickness or transverse strength of the composite material, delamination initiation occurs. Strength in the normal direction (interlaminar tensile strength-through the thickness strength) is generally lower than the transverse direction (interlaminar shear strength). In that manner through the thickness strength is the major concern when determining the strength of curved laminate [11].

In order to gain complete understanding of the mechanisms that affects the strength of curved composite laminate, through the thickness strength and fracture toughness of the material should be properly determined. Standard test procedure in the name of ASTM –D6415 ‘Measuring the Curved Beam Strength of a Fiber-Reinforced Polymer-Matrix Composite’ is used for determining the through the thickness strength of the laminates at the curved region [13].

#### 1.2.4. Relations between Fracture Toughness and Delamination Growth

Energy release rate is the dissipated energy required for extend the initial crack by unit length, and fracture toughness of the material is the critical energy release rate required for propagating a crack. Crack propagation occurs in three modes, namely Mode-I, Mode-II and Mode-III as shown in Figure 6. While delamination propagation occurs the mode I type for metals, generally in the real loading cases failure is mixed mode dominated for composite materials [14]. Generally, Mode I fracture toughness is lower than Mode-II fracture toughness. Interfacial strength or resistance to delamination propagation can be increased by increasing the fracture toughness of the material [11].

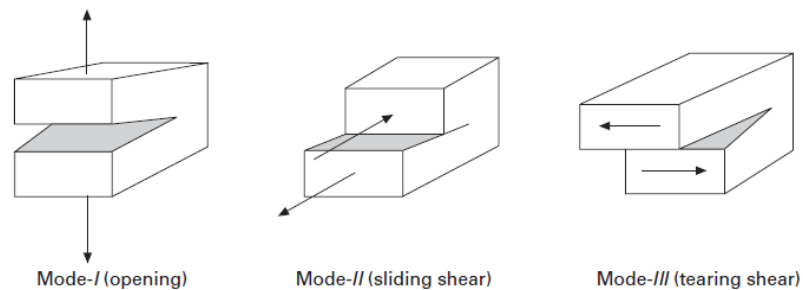


Figure 6 Fracture modes (a) Mode-I (opening), (b) Mode-II (sliding shear) and (c) Mode-III tearing

Standard test procedure in the name of ASTM –D5528 ‘Standard Test Method for Mode I Interlaminar Fracture Toughness of UD Fiber-Reinforced Polymer Matrix Composites’ is used for determining the Mode-I fracture toughness [15]. Although there is no available standard test procedure for determining Mode-II fracture toughness, End Notch Flexure test is widely used and American Society for Testing and Materials are working on standardizing the ENF test under the name ASTM WK22949 [16].

#### 1.3. Two Approaches to Strengthen L-Shaped Laminates

Replacement of the metal curved section with composite materials induced new structural difficulty, delamination problem at the curved region. This problem has become a big issue for Aerospace industry with the applications of curved composite laminates into the main structure as a load carrying members [17]. A lot of study is done on this problem to understand the phenomena. Studies showed that

strengthening can be done by increasing the thickness of the laminate [10,18]. Increasing thickness means increasing the weight and cost. It is argued that enhancing strength is more beneficial than controlling the stress state leading to delamination [19].

Different approaches can be applied to provide solution for delamination problem without degrading properties or increasing the weight of the structure. One approach is enhancements to the brittle matrix of the polymer composites. In order to improve the resistance against delamination failure, through the thickness properties is increased by increasing the fracture toughness and the interfacial strength between matrix and fibers. CNTs are very popular toughening mechanisms due to their extraordinary properties with the nanoscale geometries. The other approach is changing material structure introducing new materials. From the literature it is known that the thinner plies is desirable to increase delamination resistance [20]. Thin ply non crimp fabric materials are new class of material with half of thickness of conventional fibers and fabric like structure with less crimp provides more homogeneity and higher performance.

### 1.3.1. Carbon Nanotubes

The history of carbon nanotubes (CNTs) dates back nearly half a century. Although first discovery of CNTs were documented by Iijima in 1991[21], hollow carbon nanofibers documented in 1950s can be seen as the first examples of CNTs. First industrial synthesis of CNTs was performed in 1980s. Beginning from early 1990s CNTs are very popular research topic due to their excessive properties. Carbon nanotubes are basically hollow cylinders consisting of one or multiple graphene layers, named as single walled or multi walled carbon nanotubes, respectively [22].

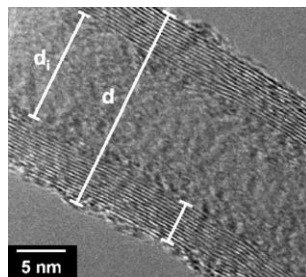


Figure 7 Example TEM photo of a multi walled CNT with outside diameter, inside diameter and wall thickness indicated [23].

Carbon nanotubes can be synthesized by the three methods, namely arc discharge, laser ablation and chemical vapor deposition (CVD) from hydrocarbons. Chemical vapor decomposition is mostly used since it is a well-established industrial process and it enables scaling up the CNT production. In this method uniform gas distribution and heat transfer to the metal catalyst nanoparticles is done by using fluidized bed reactors. Generally CNTs in various lengths and diameters are generated from the precipitated carbons of the supersaturated catalyst particle. Thermally activated CVD process tends to produce CNTs with random and tangled structures of uncontrolled length and diameter [24]. Mass production of CNTs requires large scale CVD methods which yields contaminants on the CNTs that can influence the properties of CNTs and also large energy consumption. Their diameters generally change from 0.8 nm up to 100 nm and lengths can vary from nano-scale to centimeters. Although their diameters are in the nano range their properties are much higher than many materials. For example tensile strength of individual MWCNTs reaches 100 GPa which is 10 times higher than the conventional fibers and thermal conductivity of individual SWCNTs can reach  $3500 \text{ Wm}^{-1}\text{K}^{-1}$  which is higher than the thermal conductivity of diamond [22].

CNTs are used as filler materials in the composite matrices. CNTs are used in the automotive and microelectronics industries in order to enhance the conductivity, in load bearing applications to increase the strength and toughness, in sporting goods to increase the material damping, in fiber reinforced composite parts of wind turbine blades, marine security boat hulls etc. to enhance the mechanical properties. Widespread CNT applications can also be seen in various areas as well as the composite materials. CNTs are used in lithium ion batteries to enhance the rate capability and cycle life by means of increasing the connectivity and mechanical integrity. Usage of CNTs in biosensors and medical devices is in demand due to their compliant properties with the biomolecules. Furthermore, SWCNTs are used in transistors due to their low electron scattering and bandgap. CNTs are also used as coating material and conductors in thin films [22].

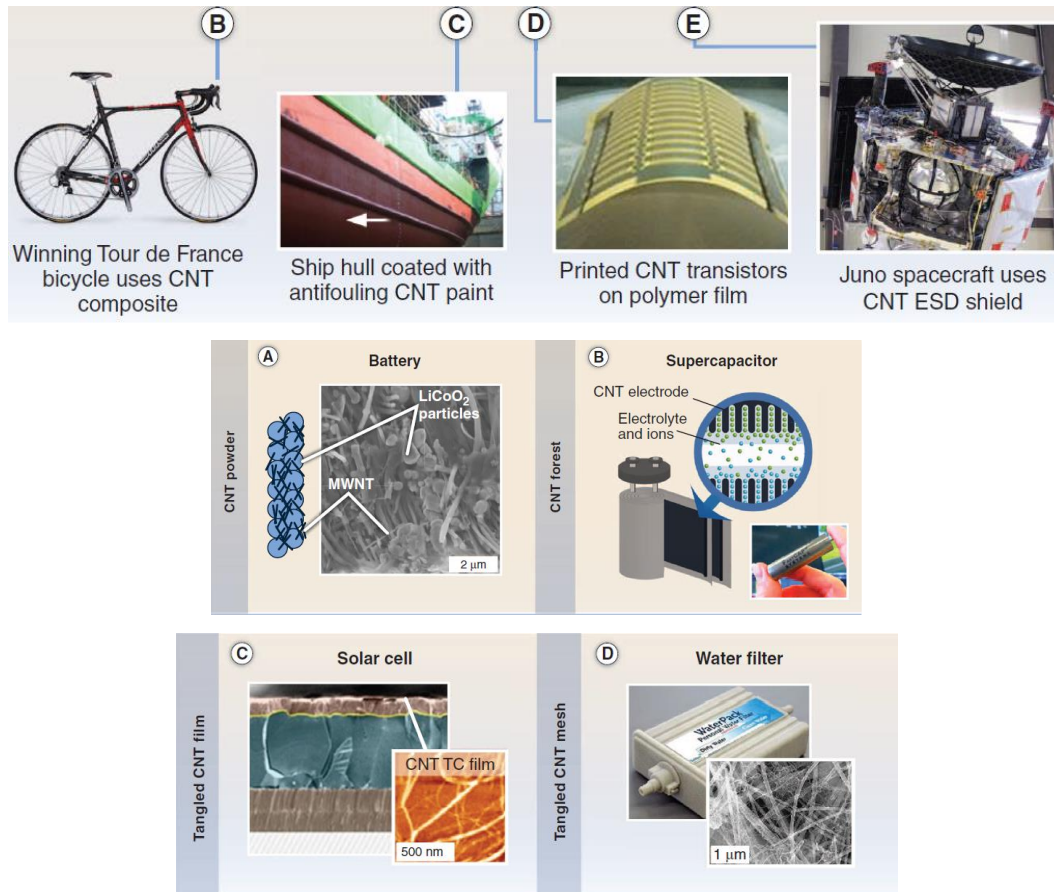


Figure 8 Example products of CNT applications [22].

However, superior properties of CNTs as a have not been realized yet, properties of CNT structures are much lower than predicted values. Improvements in the properties are highly dependent on the not only quality of CNTs but also dispersion quality in the resin [22]. High aspect ratios of CNTs cause high surface interactions and tendency to agglomerate in the matrix. Moreover, CNTs' chemical structures are very stable and absence of functional sites on the surface of CNTs results in poor dispersion quality [23]. A lot of study were conducted on surface treatments to the CNTs and different dispersion techniques in order to provide better dispersion in the matrix [21]. Ultrasonication, ball milling, grinding and high speed shearing are the typical physically dispersion techniques and chemical functionalization of CNTs are thought to be increase the dispersion of CNTs in the matrix [24].

In study of Arai et al. [25] change in Mode-I fracture toughness of CRFP laminates toughened with multi-walled carbon nano-tube (MWCNT) or vapor grown carbon fiber (VGCF) interlayer and Mode-II fracture toughness of CRFP laminates

toughened with vapor grown carbon fiber (VGCF) interlayer for different area densities (interlayer thickness) were investigated by conducting DCB and ENF tests. They showed that there is optimum interlayer thickness which is 20 g/m<sup>2</sup> area density for both DCB and ENF tests. There is 50% increase in GIC compared to base laminates for all interlayer thicknesses. 20 g/m<sup>2</sup> area density increased both maximum load and GIIC nearly two times.

In Garcia, Wardle and Hart's study [26] vertically aligned 60, 120 and 150 μm long CNTs was manufactured and placed 12<sup>th</sup> and 13<sup>th</sup> plies of a 24 ply Cytec IM7/977-3 and Hexcel AS4/8552 unidirectional preregs. The DCB and ENF tests were conducted. A 2 fold and 3 fold improvement of Mode-I and Mode-II fracture toughness, respectively was observed.

Seyhan et al. [21] investigated the change in the Mode-I and Mode-II fracture toughness of glass-NCF composites by 0.1% CNT addition to resin. No change in the Mode-I fracture toughness values was observed. Decrease in the propagation values was observed. They found out that CNT addition increased the Mode-II fracture toughness by 8% and ILSS by 11% as well as the slope of the load displacement curves of both fracture toughness tests.

In the study of Kepple et al. [27] carbon fibers were woven plain weave fabric in the warp and fill directions, and CNTs were grown on carbon fibers sheets. Mode-I fracture toughness and flexural modulus of specimens with and without CNTs were obtained by conducting double cantilever beam and DMA tests, respectively. 46% and 23% increase in the Mode-I fracture toughness was observed for CNT added laminates in the warp and fill direction, respectively. 5% increase in the flexural modulus was also observed for the specimens in the fill direction.

In study of Godara et al [28] effect of different type of 0.5 % wt. CNT addition on the mechanical properties and Mode-I fracture toughness were investigated. They manufactured preregs with CNTs and then generated laminated composites with [0] layup. They showed no significant effect on modulus, strength and ILSS with respect to base materials, however showed 80% increase in Mode-I fracture toughness. They observed CNT bridging and 25% decrease in CTE for TMWCNT and DWCNT.

In the study of Thakre et al. [29], they investigated the effect of pristine and functionalized SWCNTs on the Mode-I fracture toughness of woven carbon fiber epoxy composites using novel spraying method. Slight increase in the fracture toughness with the pristine SWCNTs addition was observed. Propagation values were decreased with both types of SWCNTs. Unstable behavior with large load drops in the load displacement curves for functionalized SWCNTs were attributed to high energy absorption at the CNT rich regions due to the enhanced interfacial bonding.

In the study Davis et al. [30] investigated the change in the strength, stiffness and fatigue properties of woven fabric composite layers with 0.2% and 0.5% amino functionalized CNT addition by the novel spraying method. Increase of 13% and 19% in tensile strength of laminates were observed with 0.2% and 0.5% amino functionalized CNTs and 2 fold increase was seen in fatigue life durability for both of the CNT fractions compared to base material.

Williams et al. [31] investigated the change in the Mode-I fracture toughness of glass fiber unidirectional prepreg composites by the novel CNT coating method for three different CNT fractions. Certain improvement up to 46% was observed for 1.2 g/m<sup>2</sup> CNT fraction and after 1.6 g/m<sup>2</sup> CNT fraction deterioration in the toughness values was observed.

In the study of Lyashenko et al. [32] Mode-II fracture toughness and interlaminar shear strength of woven carbon fiber epoxy prepreg composites were compared with the laminates having epoxy interleafs with pure CNTs, treated CNTs, protein treated CNTs and SP1 proteins. According to results, the protein treated CNTs were most efficient treatment since had the biggest effect on Mode-II fracture toughness and it did not change the ILSS of the composite. Rest of the interleaf types increased the Mode-II fracture toughness and decreased the ILSS slightly.

Avalon and Donaldson [33] investigated the effect of geometry and nanofiber addition to resin on the curved beam strength and failure modes of 900 curved composite laminates. The study was carried out computationally using ABAQUS, experimentally by conducting 4-pt bending tests and analytically using Lekhnitskii's equations. Two different radii and thicknesses of specimens were manufactured with

and without carbon nanofiber addition. Nanofibers were dispersed into chemically staged resin by shear mixing to contain 5% carbon nanofiber on the weight fraction. Results showed that 5% nanofiber addition did not have overall effect on CBS or failure load. In addition, CNT addition decreased the CBS of thinnest and specimen with smallest radius. CNT effect was only seen on the failure mode while comparing curvature ratios. Specimens with CNT tend to fail with stick slip behavior except the lowest curvature while non CNT specimens tend to fail with a rapid load drop except for the highest curvature. It was also observed that increasing radius and thickness increased the CBS. Smaller radius causes single crack and stick slip behavior. As thickness decreases specimens showed rapid load drop with multiple cracks. Another important result is that the radial stress at failure was found to be independent of any above parameters (including CNT), ranging between 30-32 MPa for all configurations and all solutions.

### **1.3.2. Novel Material – Thin Ply Non-Crimp Fabric**

The concept of non-crimp fabric or multiaxial composites was first utilized 90s by basically stitching the conventional unidirectional laminates in different orientations to create fabric type layers with less waviness and more possible orientations in order to reduce required cost and time required for manufacturing the composite laminates with unidirectional preregs. Albeit the reduced in plane properties of the non-crimp fabric composites compared to equivalent UD configuration, they provide reduced waviness and increased mechanical properties in the out-of-plane and impact performance over fabric type composites and also they are more flexible, easy to store and handle with respect to equivalent UD fiber tapes. Besides, stitching can improve through the thickness strength, delamination and impact resistance [35,40,42]. Although starting from late 90s some work done on the reducing of the conventional ply thickness, in early 2000s development of the novel spread tow-thin ply technique eventuated in new class of material called thin ply non-crimp fabric [43]. This method enables producing dry ply thicknesses as low as 0.02 mm. In this method filaments in an original thick tow are spread uniformly by passing through very low, stable airflow between the filaments. The tow sags downward and loses tension with the flow of air. As air passes through the filaments in the downward direction from air duct to vacuum, it creates pressure difference around fibers and distributes them. Schematic of methodology to distribute the fibers and carbon fiber

tows before spreading and after spreading are given in the Figure 9a and b respectively [44].

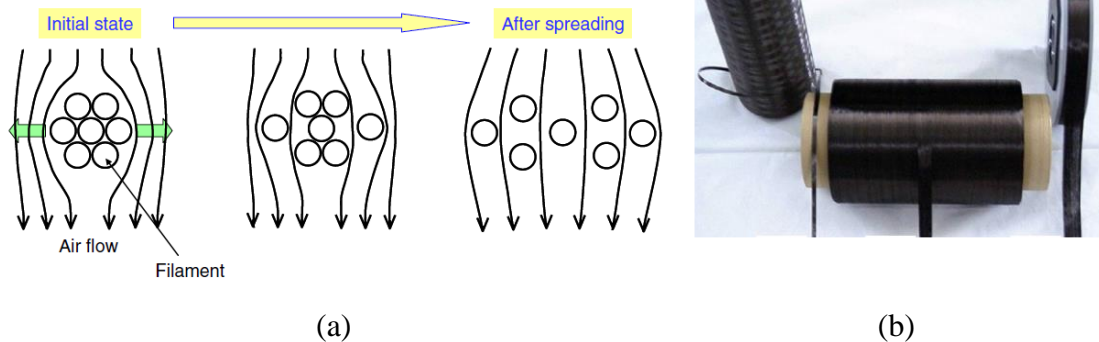


Figure 9 (a) Schematic of methodology to distribute the fibers, (b) carbon fiber tows before spreading 6mm in width, after spreading 12 mm and 20 mm in width [44].

Thin ply non-crimp fabric composites can be either in the form of conventional plain weave pattern with 10 times larger pattern than the conventional fabric (also called plain weave spread tow fabric) or in the form of stitched spread tow UD types in the different orientations as shown in Figure 10a and b respectively [39,40]. In this thesis studies was conducted with the thin ply NCF (stitched) and all the information and background are given based on the thin ply NCF material hereafter.

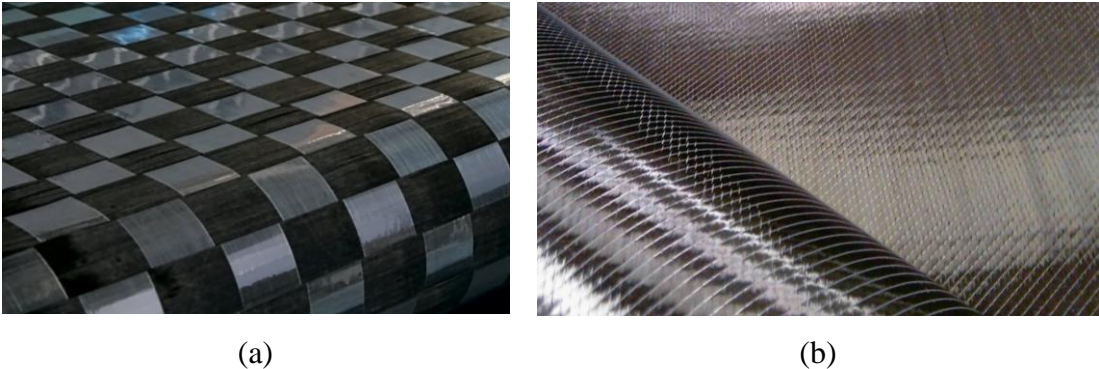


Figure 10 (a) Plain weave spread tow fabric, (b) thin ply NCF.

The production of NCF consists of three phases, namely, spread tow thin-ply technology, ply forming and combining. Firstly large conventional tows are spread down mechanically to the flat shape which is called spreading. Then UD plies are placed on top of one another in the desired directions. Lastly, plies are tied together by stitching and laminate is consolidated as shown in Figure 10 a and b. They can be used as prepregs or textiles [35].

#### **1.4. Scope of the Study**

Carbon fiber reinforced plastics are most widely used composite materials in aerospace and wind turbine industries. Their superior in plane properties with light weight structures and also ability to change and design the structure and form make composites preferable to metallic materials. Composites are applied to the primary load carrying members with complex and curved geometries with the new manufacturing techniques. On the other hand, failure mechanisms of composites are different and complicated than the metallic structures. Out of plane properties of composites are not as good as in plane properties, unbalanced properties of reinforcement and matrix and radial geometry of the curved part creates weakness through the thickness direction leading to delamination failure. Major objective is to provide solution for this problem without degrading properties or increasing the weight of the structure.

In this thesis effect of enhancements to the brittle matrix is investigated by comparing CNT added fabric type composite laminates with similar fabric composite laminates and effect of novel material thin ply non crimp fabric laminates on delamination resistance of carbon fiber reinforced plastics composites are investigated and presented in separate chapters. For this purpose standard test methods are carried out, fracture toughnesses and curved beam strengths of laminates are obtained experimentally. The dynamic delamination propagation and failure sequences under bending is captured using Photron© Fastcam SA5 ultra high speed system.

In chapter 1 applications of the curved composite structures in both aerospace and wind turbine industries are briefly introduced. Delamination problem of curved composite laminates, delamination resistance of a material is discussed by explaining the relations between curved beam strength and delamination initiation, and fracture toughness and delamination growth of material. Carbon nanotubes as an enhancement to the brittle matrix and novel material non crimp fabric are briefly introduced. Literature review is presented for CNT enhancements to the composites and thin ply NCFs.

In chapter 2, standard test methods used for determining the Mode-I and Mode-II fracture toughnesses and curved beam strength are presented. The theory and

procedure of standard fracture toughness tests for determining resistance against delamination failure and curved beam strength test for determining the through the thickness properties used in this study are illustrated. For this purpose, experimental setup and procedures are explained in details and derivations of equations used for calculations of fracture toughness and curved beam strength values are presented.

In chapter 3 experiments conducted with CNTs are presented. Firstly, details and properties of CNTs and laminates used in our studies are presented. Next, manufacturing steps of the CNT added laminates and similar fabric composite laminates are explained. Experimental results are presented for two materials separately and finally failure behavior of CNT added laminates are compared with the similar fabric composite laminates.

In chapter 4 details and properties of thin ply non crimps fabrics and unidirectional laminates ([0] and [0/45/-45/0] stacking sequence) are presented. Manufacturing steps are explained separately. Experimental results are presented for each type of laminate separately. Effect of stacking sequence on the fracture toughness without changing the 0/0 interface is investigated by comparing the results of [0] and [0/45/-45/0] unidirectional laminates. Failure behavior and fracture toughness of thin ply non-crimp fabric laminates are compared with unidirectional laminates.

## CHAPTER 2

### EXPERIMENTAL METHOD

In this chapter, experimental methods of double cantilever beam (DCB), end notch flexure (ENF) and 4-point bending tests used for determining Mode-I, Mode-II fracture toughness and curved beam strength of the material are presented. Experimental setup and procedures are explained in detail and derivations of equations used for calculations of fracture toughness and curved beam strength values are presented.

#### 2.1. Fracture Toughness Test

In this section theory and procedure of standard test methods used for determining the Mode-I and Mode-II fracture toughnesses of a material are presented.

##### 2.1.1. DCB Test for Mode-I Fracture Toughness

Double cantilever beam tests are conducted in order to obtain Mode-I fracture toughness ( $G_{IC}$ ) of laminates according to ASTM D5528-01 standard [13]. Experimental procedure and derivations of equations used for calculations of fracture toughness are given in following two sections.

###### 2.1.1.1. Experimental Setup and Procedure

In the DCB test opening forces are applied to the precracked specimen forcing the initial crack to propagate. Mode-I fracture toughness is obtained by applying opening forces at the precracked end of the laminates and propagating the initial delamination. Opening forces applied to the laminate by gulling piano hinges or loading blocks at end of the laminate [13]. In this study piano hinges, as shown in Figure 11, were used for load transmission since it is easy to obtain and process. Piano hinges were glued to the specimens by Loctite 495 instant low viscosity adhesive. Sandpaper was glued on the surface of the hinges to increase the surface roughness and provide reliable bonding with the specimen surface. DCB test specimen has a flat rectangular shape. In order to demonstrate the initial delamination, Teflon film is inserted at the mid layer of the laminates during

manufacturing. Dimensions and length of the precrack are constrained in the standard.

In the experiments Shimadzu Autograph AGS-J 10 kN displacement controlled, screw driven tensile testing machine were used as the load indicator and load displacement data was recorded by Trapezedium software. Specimen is put into loading machine to be aligned perpendicular to the loading line and experimental setup of DCB test is shown in the Figure 11.



Figure 11 Experimental Setup of double cantilever beam test.

During the loading, when the crack propagates, load,  $P$ , and displacement,  $d$ , values are recorded and crack extension is measured. The peaks of the load displacement curve are used as the load values of crack propagations in the calculations according to the max load theory as shown in Figure 12. The crack extension is obtained by capturing the photos of the specimen during the test. Tip of the crack is monitored and captured as crack propagates. Corresponding load and displacement values are recorded at the same time. After the test photos are analyzed and crack extensions are determined. For the CNT studies Canon 1DX 24 MP full frame Machine with Canon L135-80 100mm macro lens were used for capturing the crack length during the experiments. For the thin fiber NCF studies Photron AS4 high speed cameras were used.

Mode-I fracture toughness obtained from the first crack propagation and first load drop gives the initiation value. Since initiation value obtained from the precrack

propagation gives higher values, DCB test is conducted in two parts. At the first part initial crack is propagated about 2 mm to obtain real sharp crack. Then test is stopped and specimen is unloaded at 25 mm/min constant cross head speed and data is recorded. At the second part this procedure is continued up to 45 mm crack growth to obtain fracture toughness resistance curves (R-curves). Then at the end of the test specimen is unloaded at 25 mm/min constant cross head speed and data is recorded. Cross head speed of loading machine should be between 0.5 mm/min to 5 mm/min according to standard. Since delamination growth is rate dependent and higher values can cause unstable delamination growth specimens are loaded at 0.5 mm/min cross head speed.

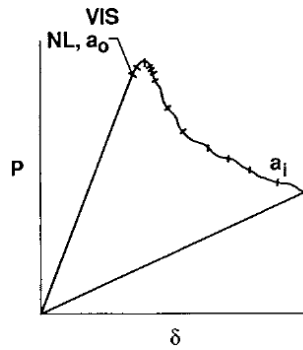


Figure 12 Load-Displacement curve of brittle matrix CRFP from the DCB test.

#### 2.1.1.2. Mode-I Fracture Toughness Calculations

Four different methods are available to calculate the Mode-I fracture toughness, namely beam theory, modified beam theory, compliance calibration and modified compliance calibration. The detail and derivations of equations are given as follows. All of the three methods are based on beam theory which assumes DCB specimen as a perfect beam.

Interlaminar fracture toughness which is critical energy release rate is obtained from compliance by

$$G = \frac{P^2}{2b} \left( \frac{dC}{da} \right) \quad (1)$$

where P is the applied load, a is the crack length and C is the compliance.

## Beam theory

Compliance of DCB specimen is defined as

$$C = \frac{8a^3}{Ebh^3} \quad (2)$$

where E is the stiffness of the laminate, b is the width and h is the thickness of the specimen.

Putting eqn. (2) into (1) gives:

$$G_{IC} = \frac{P^2 24a^2}{2Ebh^3} = \frac{3P^2 C}{2ba} \quad (3)$$

Since compliance is also defined as displacement over load ( $C=\delta/P$ ), fracture toughness obtained by the beam theory is:

$$G_{IC} = \frac{3P\delta}{2ba} \quad (4)$$

In this relation composite beam is considered as perfectly build-in and  $G_{IC}$  value is overestimated since there rotation at the crack tip. For more coherent estimation of  $G_{IC}$  value a correction factor based on specimen compliance and crack length is implemented by the modified beam theory method.

## Modified Beam theory

In this method precracked part of the DCB specimen is assumed to be two cantilever beams built-in at a distance  $\Delta$  in front of the crack tip as shown in Figure 13 and the distance  $\Delta$  is called correction factor.

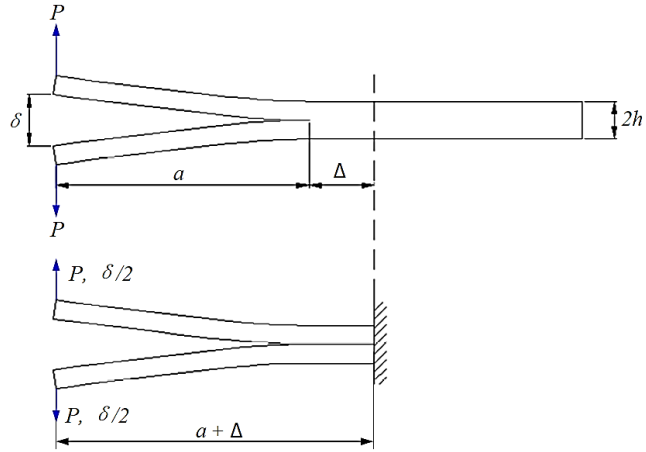


Figure 13 Two cantilever beam assumption representation of DCB specimen.

Alternative representation of Eqn. (2) can be written as follows

$$C^{1/3} = ma \tag{5}$$

where  $\Delta$  corresponds the intersection point of linear fit curve of  $C^{1/3}$  - a plot and horizontal axis as shown in Figure 14.

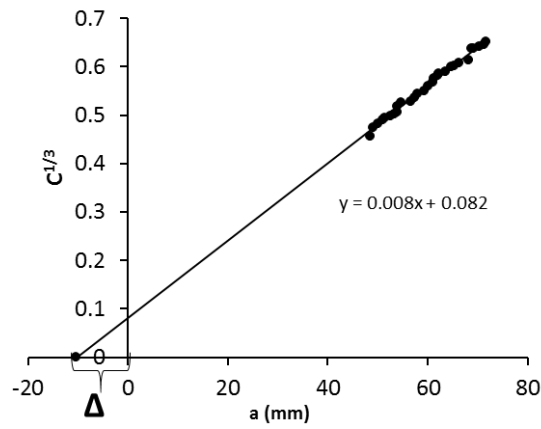


Figure 14 MBT correction line,  $\Delta$  represents the intersection point of linear fit curve of  $C^{1/3}$  - a plot and horizontal axis.

Corrected formula for Fracture toughness is then defined as following:

$$G_{IC} = \frac{3P\delta}{2b(a + |\Delta|)} \tag{6}$$

## Compliance calibration

From the simple beam theory model, the deflection,  $v$ , of the tip of a cantilever beam with length  $a$  can be written as:

$$\vartheta = \frac{Pa^3}{3EI} \quad (7)$$

For a double cantilever beam, the end deflection is assumed to be:

$$\frac{\delta}{2} = RPa^n \quad (8)$$

Instead of Eqn. (2) predicted compliance of the DCB specimen can be assumed as:

$$C = Ra^n \quad (9)$$

In Eqn. (9) unknown values  $R$  and  $n$  can be found by using linear trend line of measured data of compliance and crack length in logarithmic scale as presented in Figure 15. The slope of this line gives unknown term  $n$ . The term  $R$  describes the geometrical and material properties of the specimen.

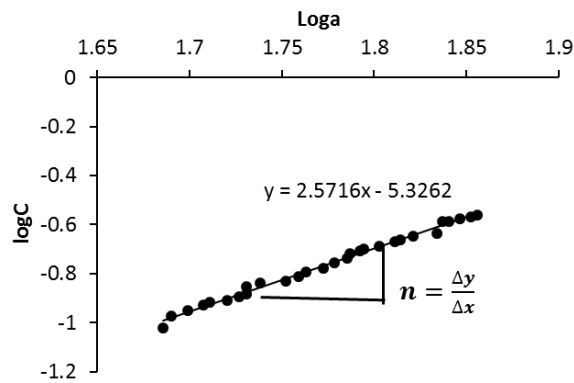


Figure 15 CC correction line.

Mode-I fracture toughness based on compliance calibration method is obtained by putting Eqn. (9) into Eqn. (2) as shown in Eqn. (10).

$$G_{IC} = \frac{nP\delta}{2ba} \quad (10)$$

### Modified compliance calibration

In This method compliance is normalized with the specimen thickness and compliance can be written as:

$$\frac{a}{h} = A_1 C^{\frac{1}{3}} + A_0 \quad (11)$$

The slope  $A_1$  is found from the linear fit of  $a/h$  versus  $C^{1/3}$  points as shown in the Figure 16.

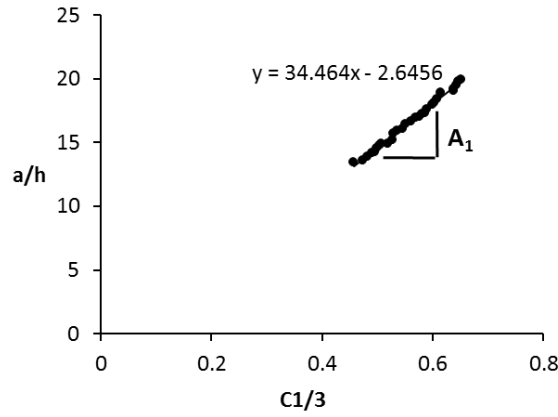


Figure 16 MCC correction line.

Putting eqn. (11) into eqn. (2) gives the fracture toughness according to modified compliance calibration by:

$$G_{IC} = \frac{3P^2 C^{\frac{2}{3}}}{2A_1 b h} \quad (12)$$

### Large displacement corrections

For the ratio of the opening displacement at delamination onset,  $\delta$ , to the delamination length,  $a$ ,  $(\delta/a)$  values greater than 0.4, a correction parameter  $F$  is used to correct large displacement effects for the case where piano hinges are used. The correction factor  $F$  is defined by:

$$F = 1 - \frac{3}{10} \left( \frac{\delta}{a} \right)^2 - \frac{3}{2 \left( \frac{\delta t}{a^2} \right)} \quad (13)$$

In which  $t = th + h/4$

where  $t$  is the thickness of piano hinges,  $h$  is the specimen thickness,  $\delta$  is the displacement,  $a$  is the crack length.

### 2.1.2. Mode-II Fracture Toughness Test

End Notch Flexure tests are conducted in order to obtain Mode-II fracture toughness of laminates. There are several types of test to determine Mode-II fracture toughness as shown in Table 1, however, most widely used test method is ENF test. Table below [51] shows the advantage and disadvantage of the test methods.

Table 1 Advantages and disadvantages of available test method to determine the Mode-II fracture toughness.

	<b>Advantage</b>	<b>Disadvantage</b>
End notch flexure ( <b>ENF</b> )	simple, most used	unstable
Stabilized End Notched Flexure ( <b>SENF</b> )	stable	complicated, special equipment
End loaded split test ( <b>ELS</b> )	stable	clamping variability
4-point end notch flexure test ( <b>4ELS</b> )	stable	little experience

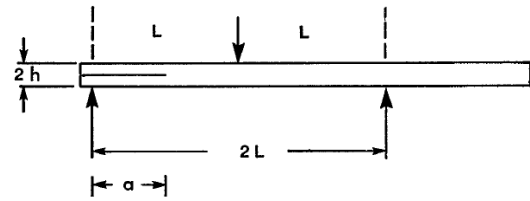
There is no available standard method for Mode-II fracture toughness test yet, due to the problems such as type of starter defect, definition of initiation, stability, and friction and data analysis. ASTM committee is working on standardization in the name of ‘ASTM WK22949 - New Test Method for Determination of the Mode-II Interlaminar Fracture Toughness of Unidirectional Fiber-Reinforced Polymer Matrix Composites Using the End-Notched Flexure (ENF) Test’ [51]. Experimental procedure and derivations of equations used for calculations of fracture toughness are given in following two sections.

#### 2.1.2.1. Experimental Setup and Procedure

ENF test is basically 3 point bending test. Mode-II fracture toughness is obtained by applying concentrated load at the mid plane of the laminate creating shear force at the precracked end of the laminates and propagating the initial delamination. ENF test specimen has a flat rectangular shape. In order to demonstrate the initial delamination, Teflon film is inserted at the mid layer of the laminates during manufacturing. Experimental setup of ENF test is shown in Figure 17a.



(a)



(b)

Figure 17 (a) Experimental test setup, (b) specimen geometry of ENF test.

ENF test specimen is very similar to the DCB test specimen, it has a flat rectangular shape. In order to demonstrate the initial delamination, Teflon film is inserted at the mid layer of the laminates during manufacturing as shown in Figure 17b.  $2L$  is the span length is usually 100 mm,  $2h$  is the thickness and generally between 3-5 mm,  $b$  is the specimen width and generally between 20-25 mm and  $a$  is the delamination length. There is no restriction on delamination length, however generally crack length to span length ratio is lower or equal to 0.5 ( $a/L \leq 0.5$ ).

In the ENF test specimen is deflected by a concentrated load applied at the mid part until propagation occurs. Since delamination propagation in ENF test is unstable, test is stopped after first load drop. Only one fracture toughness ( $G_{IIC}$ ) value is obtained. Similar to the DCB test, whether precracking or not before the ENF test is another issue besides the problems related nature of the test given above. Testing the specimens without precracking generally results in higher values than with precracked specimens since film insert creates resin rich region and acts like obstacle against delamination yielding higher energy absorption as shown in Figure 18 [51], which shows the results of ENF test with no precrack and Mode-I precracks. Wedge precracking or Mode-I test precracking are advised prior to ENF test in order to create sharp crack tip. As the film is inserted during manufacturing to demonstrate the resin rich region is created at tip of the crack [50].

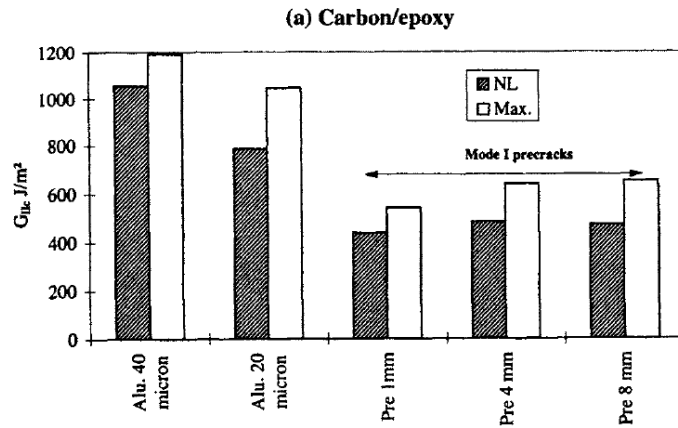


Figure 18 ENF test results with no precrack and Mode-I pracracks [50].

### 2.1.2.2. Mode-II Fracture Toughness Calculation

The derivation of Mode-II Fracture toughness is made based on the Strain energy release rate equation [50].

$$G = \frac{P^2}{2b} \frac{dC}{da} \quad (14)$$

Figure 19 represents the three parts of deflection (in the figure  $\Delta a$ ,  $\Delta b$ ,  $\Delta c$ ) of the ENF specimen during the test.  $\Delta a$  is due to curvature in the in the boundary condition,  $\Delta b$  is due to slope at point B in the figure and  $\Delta c$  is due to the curvature in the section AB. For the case of small deflection these three deflections summed and result is the total deflection of the right part of the beam.

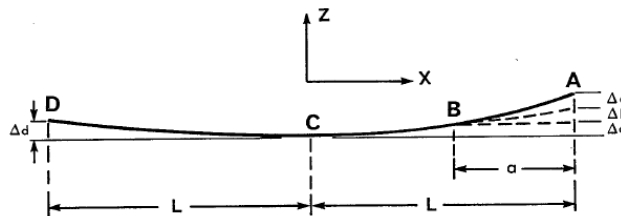


Figure 19 Three parts of deflection of the ENF specimen defined as  $\Delta a$ ,  $\Delta b$ ,  $\Delta c$ .

The deflection of the right half of the specimen which involves delamination calculated as follows.

The curvature for the anisotropic materials is:

$$\begin{bmatrix} k_1 \\ k_2 \\ k_6 \end{bmatrix} = \begin{bmatrix} d_{11} & d_{12} & d_{16} \\ d_{21} & d_{22} & d_{26} \\ d_{61} & d_{62} & d_{66} \end{bmatrix} \begin{bmatrix} M_1 \\ M_2 \\ M_6 \end{bmatrix} \quad (15)$$

Where  $[d_{ij}]$  is the compliance matrix and  $[M_{ij}]$  is the moment.

Beam is divided into 4 regions as shown in Figure 20 below and deformations are obtained separately.

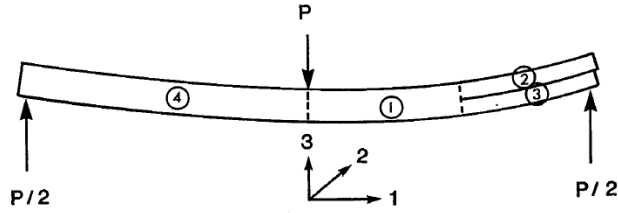


Figure 20 Division of the specimen into 4 regions.

In the first region curvature is:

$$k_1^{(1)} = d_{11}^{(1)} M_1^{(1)} = d_{11}^{(1)} \frac{P(L-x)}{2b} \quad (16)$$

Deflections of  $\Delta_a$  and  $\Delta_b$  are calculated as

$$\Delta_a = \int_0^{L-a} \int_0^x \frac{d_{11}^{(1)}}{2b} P(L-x) dx dx = \frac{d_{11}^{(1)}}{12b} P[2L^3 - 3aL^2 + a^3] \quad (17)$$

$$\Delta_b = a \frac{dz}{dx} \Big|_{x=L-a} = a \int_0^{L-a} \frac{d_{11}^{(1)}}{2b} P(L-x) dx = \frac{d_{11}^{(1)}}{4b} P[aL^2 - a^3] \quad (18)$$

$\Delta_c$  is calculated curvature of region 2 or 3 and then integrating twice between  $L-a$  and  $a$ . the result is:

$$k_1^{(2)} = \frac{d_{11}^{(2)}}{b} P_2(L-x) \quad (19)$$

$$\Delta_c^{(2)} = P_2 d_{11}^{(2)} \frac{a^3}{3b} \quad (20)$$

$$\Delta_c = \frac{Pa^3}{6b} \left[ \frac{d_{11}^{(2)} d_{11}^{(3)}}{(d_{11}^{(2)} + d_{11}^{(3)})} \right] \quad (21)$$

Total deflection of the specimen defined as follows:

$$\Delta = \Delta_a + \Delta_b + \Delta_c = \frac{P}{12b} \left[ 2(L^3 - a^3) d_{11}^{(1)} + a^3 \left( \frac{d_{11}^{(2)} d_{11}^{(3)}}{d_{11}^{(2)} + d_{11}^{(3)}} \right) \right] \quad (22)$$

$$\Delta = \frac{P}{12b} [2L^3 + a^3(4\alpha - 1)] \quad (23)$$

$$\alpha = \frac{d_{11}^{(2)} d_{11}^{(3)}}{4d_{11}^{(1)} [d_{11}^{(2)} + d_{11}^{(3)}]} \quad (24)$$

The compliance of the specimen is defined as  $\Delta/P$

$$c = \frac{d_{11}^{(1)}}{12b} [2L^3 + a^3(4\alpha - 1)] \quad (25)$$

Taking derivative of compliance with respect to a, and putting result into energy release rate equation gives:

$$G = \frac{P^2}{2b} \frac{dC}{da} = \frac{a^2 P^2 d_{11}^{(1)} (4\alpha - 1)}{8b^2} = \frac{3a^2 P^2 c (4\alpha - 1)}{2b(2L^3 + (4\alpha - 1)a^3)} \quad (26)$$

For unidirectional specimens

$$d_{11}^{(2)} = d_{11}^{(3)} = 8d_{11}^{(1)} \quad (27)$$

This gives  $\alpha=1$

Inserting  $\alpha=1$  and  $C=\delta/P$  into Eqn. (26) gives

$$G_{IIC} = \frac{9a^2 P \delta}{2b(2L^3 + 3a^3)} \quad (28)$$



### 2.2.2. Frictional Effects on 4-Point Bending Tests

Two different test setup configurations were used in the 4-pt bending tests as shown in Figure 22a and b, respectively. For both setup configurations upper part consists of rollers which used for applying the load on the specimen with freedom to rotate. For the first configuration bottom part has rollers, however rollers are not allowed to rotate freely which creates frictional forces at the contact point. In the Second configuration rollers of the bottom part are allowed to rotate freely.

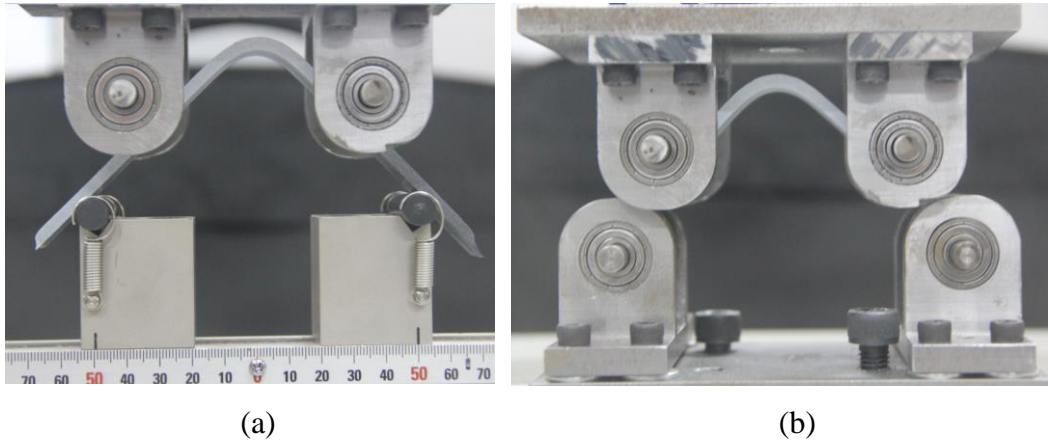


Figure 22 . Two types of setups used in 4-point bending tests with: (a) bottom part not allowing free rotation of the rollers, (b) bottom part with rollers allowed to freely rotate.

In the Figure 23 a 4-point bending load displacement curves of all types of specimens are given together. Thin lines indicate the results from the old test setup. Thicker lines correspond to results obtained with the new setup. Higher stiffness is observed with the old setup even though same loading rate and material were used. When load displacement curves of all types of materials were compared, it is noticed that the increase in the stiffness depends on a constant. Displacements are shifted by multiplying the curves by a constant of 1.34 and load displacement curves obtained from both test configurations are found to overlap for all materials as shown in Figure 23b. Since loading rate is constant for all of the tests and constant of 1.34 value does not change with the material type, the only parameter left was the boundary condition of the bottom part of the setup. The increase in the stiffness of load displacement curve is attributed to the roller effect. Since rollers are not allowed to rotate freely in the first configuration, it creates frictional forces at the contact point resulting in resistance to sliding of the beam and restricting the free movement.

This argument was investigated computationally using ANSYS software by modeling homogeneous curved specimen in 3D. Finite element model and boundary conditions for a 4-point bending test to investigate the effect of friction in the bottom rollers are given in the Figure 24. In the first case the bottom boundary modeled with friction coefficient of 0.3 and at the second case friction coefficient was chosen as 0.001 which means roller type of boundary [52].

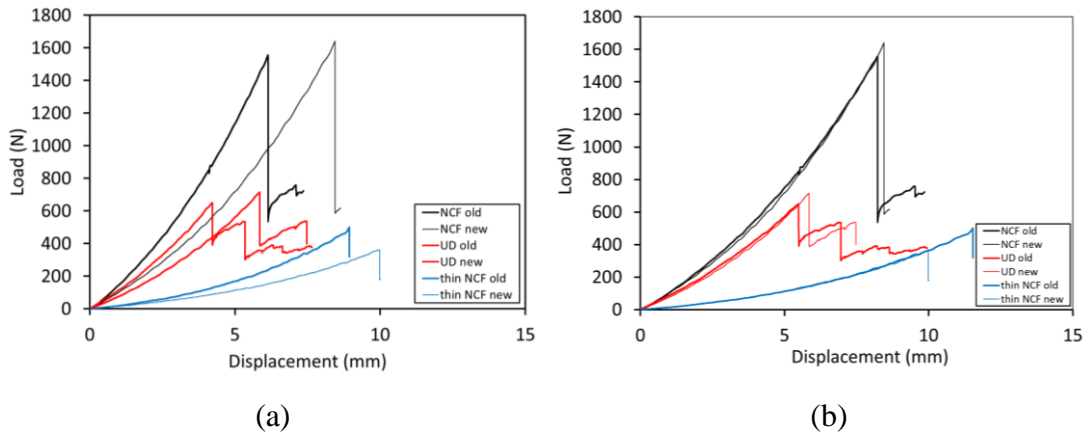


Figure 23 4-point bending test load-displacement curves for 48-ply UD, 12-ply thin ply NCF and 6-ply thin ply NCF: (a) original curves for frictional bottom rollers (thin lines) and friction free bottom rollers (thick lines), (b) modified curves obtained by multiplying the stiffness by a constant of 1.34.

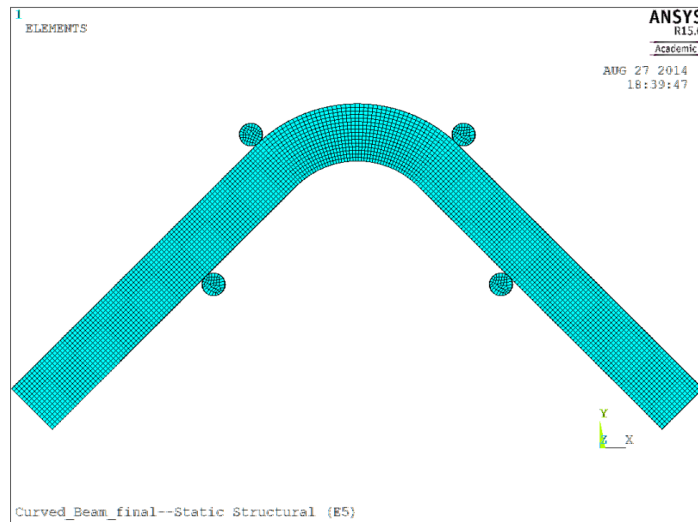


Figure 24 Finite element model and boundary conditions for a 4-point bending test to investigate the effect of friction in the bottom rollers.

Load-displacement curves obtained from simulations for a friction coefficient of 0.3 representing frictional rollers (red line) and 0.001 representing rolling friction (black line) are given Figure 25. It is clearly seen that for the same material, loading rate and geometry, changing friction coefficient from 0.001 to 0.3 increases the stiffness of the load displacement curve. The coefficient for displacement shifting of curve of 0.3 friction coefficient to overlap with the curve of 0.001 friction coefficient is found to be 1.37 which is very close to experimental curve coefficient, it concluded that with changing the bottom boundary conditions directly affects the stiffness of the curve and friction coefficient of the first test setup configuration is very close to 0.3.

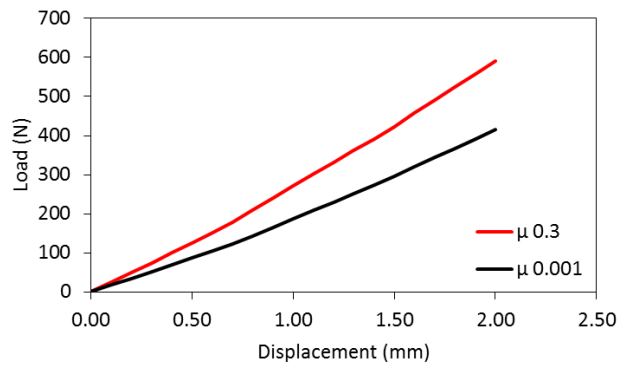


Figure 25 Load-displacement curves obtained from simulations for a friction coefficient of 0.3 representing frictional rollers (red line) and 0.001 representing rolling friction (black line).

### 2.2.3. Curved Beam Strength Calculation

Curved beam strength is calculated using relation given below, which is basically moment per unit length. The moment on the curved section of the specimen is the product of the force exerted by one of the cylindrical loading bars and the distance, 10, between two bars along one leg [13].

$$CBS = \frac{Pl_0}{w} \quad (29)$$

Where the bar force is calculated from the total force exerted on specimen P, at the first force drop and the distance between two bars along one leg is calculated from geometries of the loading fixture and test specimen.

$$CBS = \frac{P}{2w \cos(\varphi)} \left( \frac{d_x}{\cos(\varphi)} + (D + t) \tan(\varphi) \right) \quad (30)$$

Where P refers to applied force, w to width and t to thickness of specimen. Other unknowns are shown on the experimental setup picture in figure 1(a).

There are two variables in CBS equation, namely load (P) and deflection ( $\phi$ ). P value is read directly from measuring machine.  $\phi$  value is determined from its stroke as follows:

$$d_y = d_{yi} - \Delta \quad (31)$$

Where  $d_{yi}$  is measured initial vertical distance between bottom and upper rollers and  $\Delta$  is stroke of measuring machine.

$$\phi = \sin^{-1} \frac{-d_x(D + t) + d_y * (d_x^2 + d_y^2 - D^2 - 2Dt - t^2)^{0.5}}{d_x^2 + d_y^2} \quad (32)$$

Interlaminar stress calculation was developed by Lekhnitskii as given in Eqn. 32.

$$\sigma_r = -\frac{CBS}{r_o^2 g} \left( 1 - \frac{1 - \rho^{k+1}}{1 - \rho^{2k}} \left( \frac{r_m}{r_o} \right)^{k-1} - \frac{1 - \rho^{k-1}}{1 - \rho^{2k}} \left( \frac{r_m}{r_o} \right)^{k+1} \rho^{k+1} \right) \quad (33)$$

Where  $r_o$  is inner radius, g is defined as follows:

$$g = \frac{1 - \rho^2}{2} - \frac{k}{k+1} \frac{(1 - \rho^{k+1})^2}{1 - \rho^{2k}} + \frac{k\rho^2}{k-1} \frac{(1 - \rho^{k-1})^2}{1 - \rho^{2k}} \quad (34)$$

k is the ratio of Young's modulus in between perpendicular directions and  $\rho$  is ratio between inner and outer radius

$$g = \left( \frac{E_\phi}{E_r} \right)^{0.5} \quad \rho = \frac{r_i}{r_o}$$

Finally maximum radial stress location is given as:

$$r_m = \frac{(1 - \rho^{k-1})(k+1)(r_o\rho)^{k+1}}{(1 - \rho^{k+1})(k-1)r_o^{1-k}} \quad (35)$$



## CHAPTER 3

### **EFFECT OF CARBON NANOTUBES ON THE FRACTURE TOUGHNESS AND CURVED BEAM STRENGTH OF FABRIC COMPOSITE LAMINATES**

In this chapter, fracture toughness and curved beam strength results are presented for CNT added dry 0/90 fabric CFRP laminates. These results are then compared with the results of prepreg 0/90 fabric laminates which are chosen due to the availability of this material in the lab. However, the conclusions are not only dependent on the addition of CNT but also can be a function of the different manufacturing techniques used to produce prepreg vs. dry fabric specimens. In the future, a comparison should be made with dry 0/90 fabric as a baseline material when it becomes available to isolate the effect of CNT addition.

In section 3.1.1 materials, and in sections 3.1.2 and 3.1.3 specimen geometry and manufacturing process to obtain the specimens for both CNT added dry 0/90 fabric and prepreg 0/90 fabric laminates are presented. In sections 3.2 and 3.3 the results are presented for prepreg-fabric and CNT-fabric material, respectively. The results are presented in the following order for each material: Mode-I and Mode-II fracture toughness tests, curved beam strength tests, high speed camera images of failure process, and micrographs of failed specimens. Finally, the results for the two specimens are discussed in section 3.4.

#### **3.1. Specimen Preparation**

##### **3.1.1. Material**

For the CNT studies 5 Harness Satin plain weave [0/90] carbon Fabric type composite material is chosen since it is easy to process. 5 harness satin weave is formed by being woven of the fiber to float over four bundles then under one, this method provides less crimp and easily to be draped over the most complex shapes which is very suitable for manufacturing L-shaped geometry. As a baseline material HexPly® AS4/8552 3K, 5HS plain weave [0/90] carbon fabric/epoxy prepreps were

used. This material is amine cured, high performance, designed for primary aerospace applications with 280 gsm weight, 1.77 g/cm<sup>3</sup> fiber density, 1.57 g/cm<sup>3</sup> laminate density, 55% nominal fiber volume and 0.28 mm cured ply thickness and other properties are given in Table 1 [41].

Table 2 AS4/8552 Prepreg Laminate Properties

<b>E<sub>11</sub>= E<sub>22</sub> (GPa)</b>	<b>E<sub>33</sub> (GPa)</b>	<b>G<sub>12</sub> (GPa)</b>	<b>v<sub>13</sub></b>	<b>Density (kg/m<sup>3</sup>)</b>	<b>Cured Ply Thickness (mm)</b>
55.7	8.5	3.7	0.3	1570	0.28

HexForce® AS4/AH370-5H 6K, 5HS plain weave [0/90] carbon dry fabrics providing strength and stiffness in two directions with very good handling characteristics and good drape were used for the CNT added material. This material is balanced high performance woven fabrics and high drape makes easier to lay up over complex forms and use for non-autoclave processing with 370 gsm weight and 0.37 mm ply thickness [42]. For the resin system of CNT added laminates Araldite® LY 5052 epoxy resin with Aradur® LY 5052 hardener and high CNT fraction bisphenol-A type liquid epoxy resin were used together. Araldite® LY 5052 epoxy resin is low viscosity matrix system suitable wet layup and designed for aerospace applications [43]. Premixed high fraction CNTs in liquid bisphenol-A type base resin in the brand name Epocyl™ NCR128-02 (also called master batch) produced by Nanocyl (Namur, Belgium) was used for CNT addition to the laminates. The base epoxy resin Epon 828 itself is a classical diglycidyl ether bisphenol-A (DGEBA) material which is generally used for fiber reinforced composites, construction, electrical and aerospace adhesives and marine coatings [44]. NANOCYL™ NC7000 series thin multi-walled carbon nanotubes in the purity of 90%, produced by the catalytic carbon vapor deposition (CCVD) process are used in the master batch [45]. The properties of CNTs are given in and TEM images of CNT bundles in the powder form are given in the Figure 26 TEM images of NANOCYL™ NC7000 series thin walled CNTs.

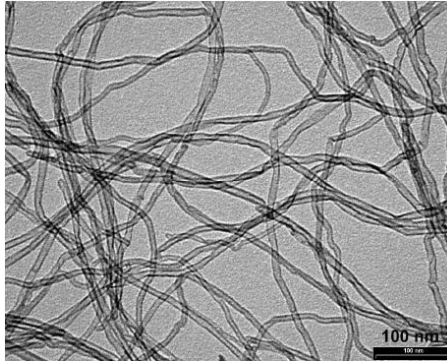


Figure 26 TEM images of NANOCYL™ NC7000 series thin walled CNTs

Table 3 Properties of NANOCYL™ NC7000 CNTs [45]

	Value	Method of measurement
Average diameter	9.5 nm	TEM
Average length	1.5 $\mu\text{m}$	TEM
Carbon purity	90 %	TGA
Metal oxide	10 %	TGA
Amorphous carbon	-	HRTEM
Surface area	$\text{m}^2/\text{g}$	BET

High shear dispersion process and functionalization techniques are used in order to exfoliate the CNT bundles in the resin and CNT fraction in the master batch is 20% on the weight basis according to the information retrieved from the company. SEM pictures of neat master batch is given in the Figure 27 Viscosity change of neat base resin and master batch with temperature [46]. Recommended mixing ratio of master batch and the matrix epoxy is 1 to 6. The viscosity change of final form of master batch and the base epoxy as a function temperature are shown in the Figure 27. Since CNT addition to the resin slightly changes the viscosity the processability of the master batch does not change [46].

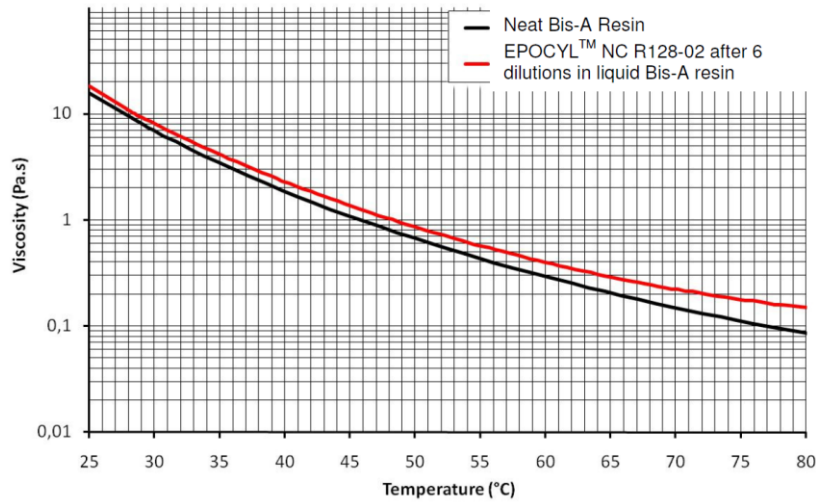


Figure 27 Viscosity change of neat base resin and master batch with temperature [46]

### 3.1.2. Specimen Geometry

For both prepreg-fabric and CNT-fabric laminates both the fracture toughness and 4-point bending test specimens were manufactured at the same time in one specimen geometry as shown in Figure 28 Specimen geometry of prepreg-fabric and CNT added material used for fracture toughness tests and 4-point bending tests. L-shaped specimen's shorter leg length was 100 mm and the other leg was 240 mm long containing a 75 mm teflon film at the mid layer in order to demonstrate the initial delamination for the fracture toughness tests (DCB and (ENF). prepreg-fabric laminates are made of 12 plies with 3 mm thickness. In order to have 3 mm thickness CNT added laminates are made of 8 plies, however after manufacturing CNT added specimens' thicknesses are measured 4 mm. Four point bend specimens and fracture toughness tests specimens' were obtained by cutting the longer leg of the manufactured specimen 90 mm away from the end of the curved part by using diamond saw cutting machine. Final dimensions and specimen number are given in the Table 4.

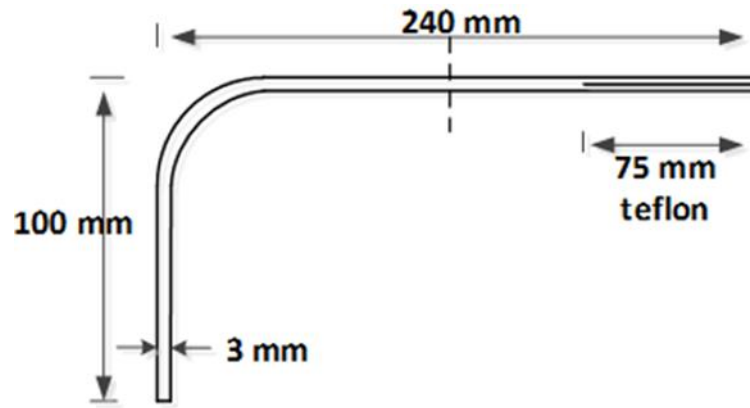


Figure 28 Specimen geometry of prepreg-fabric and CNT added material used for fracture toughness tests and 4-point bending tests.

Table 4 Dimensions and number of specimens used in each type of tests.

	DCB		ENF		4-pt bending	
	prepreg	CNT	prepreg	CNT	prepreg	CNT
Ply #	12	8	12	8	12	8
Dimensions (mm)	L=135 w=25 t=3	L=135 w=25 t=4	L=135 w=25 t=3	L=135 w=25 t=4	L1=L2=100 w=25 t=3	L1=L2=100 w=25 t=4
# of specimens	2	2	2	2	3	3

### 3.1.3. Manufacturing:

For CNT studies specimen manufacturing process was done in TAI facilities. Prepregs-fabric and CNT-fabric L-shaped laminates were manufactured by hand layup technique. Aluminum right angled male tool with a very fine surface finish was used to give specimens L shape. At the first step tool was cleaned with 770-NC release agent. HexPly® 8552 5H satin weave fabric prepregs and HexPly® 8552 5H satin weave dry fabrics, properties are given in the previous section, were laid up on the tool as shown in the Figure 29.

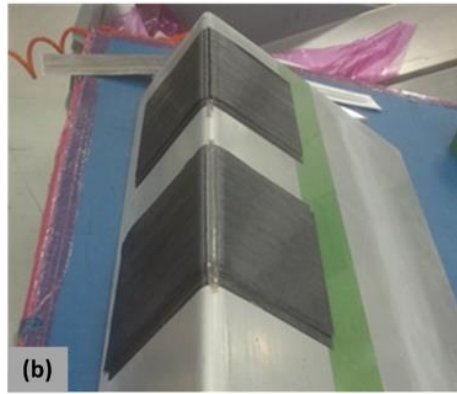


Figure 29 Laid up prepregs on the right handed male tool.

After the layup process tool was wrapped with release film and then breather fabric for absorbing the extra resin on the laminate. Finally tool was placed in a vacuum bag and closed with sealant tape. Vacuum ports were placed into bag to control the pressure and then the bag was vacuumed to 21 mm-Hg.

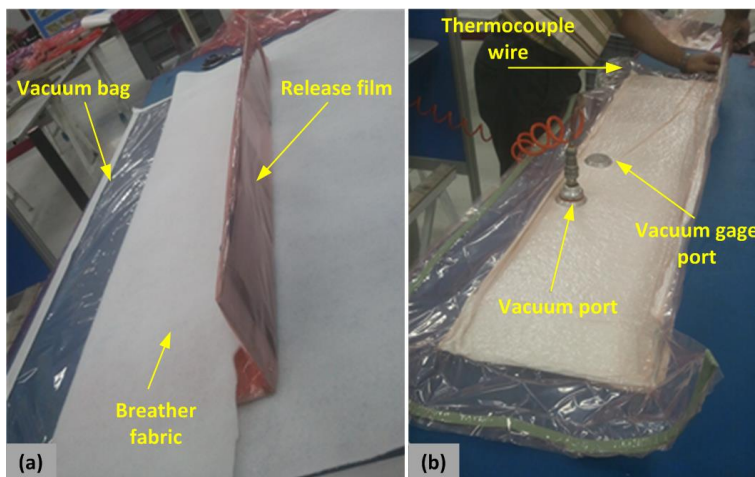


Figure 30 (a) Placements of release film and breather fabric on the tool (b) vacuum bagging process.

After vacuum bagging process was completed, CNT added laminates were left in the vacuum for 10 hours for curing and autoclave technique was used to cure the prepreg-fabric laminates. The pressure of autoclave was 6.9 bar and temperature was increased to 1800 at the rate of 0.5-30C/min. Laminates were cured at autoclave for 3 hours and after curing cycle was completed temperature and pressure were decreased to the room conditions. The total autoclave process was completed in almost 10 hours and whole process is shown in Figure 31.

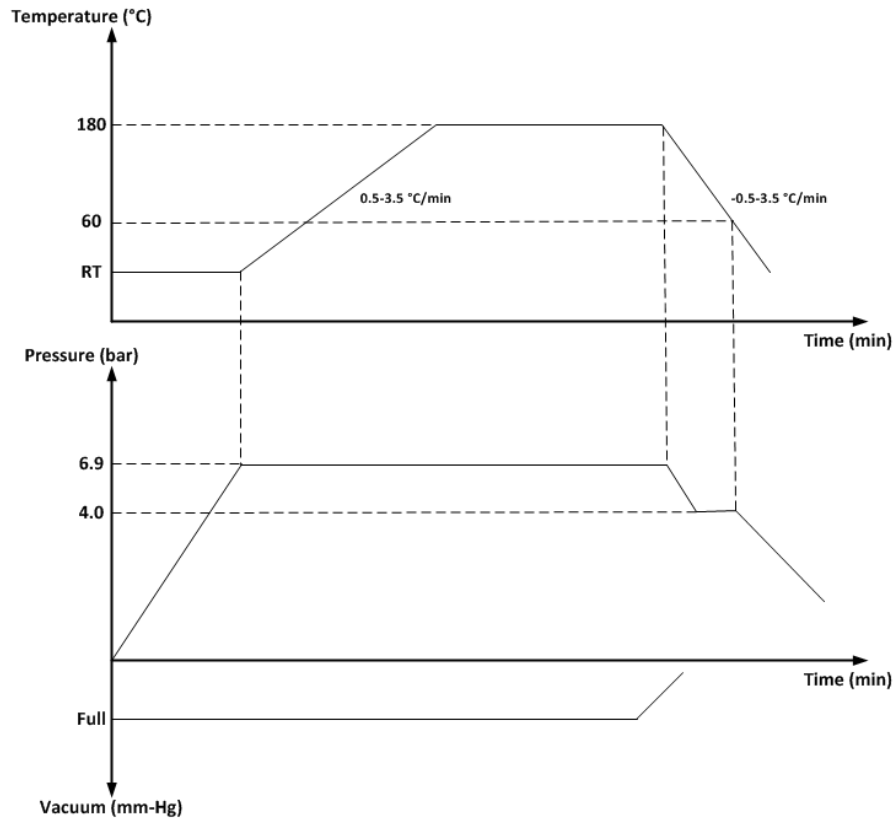
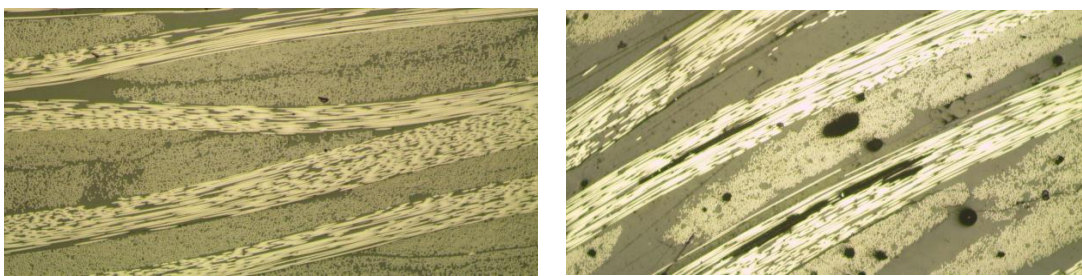


Figure 31 Autoclave curing cycle [41].

Figure 32a and b presents the microscopic view of prepreg-fabric and CNT added materials in the thickness directions after manufacturing.



(a)

(b)

Figure 32 microscopic view of (a) prepreg-fabric and (b) CNT added materials in the thickness directions.

## 3.2. Prepreg-Fabric Laminates

### 3.2.1. Mode-I Fracture Toughness

DCB test load displacement curves of prepregs-fabric laminates are given in Figure 33. Stiffness and behavior of the curves are very similar, classic fabric type behavior is observed. Maximum load reaches 70 N. around 55 N small load drop is observed. Big unstable load drops are observed after the maximum load value has been reached.

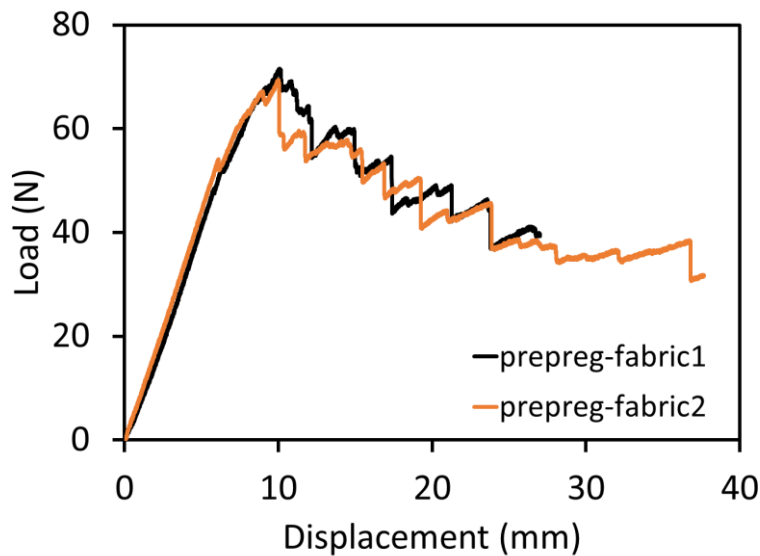


Figure 33 DCB test load displacement curves of prepreg-fabric laminates.

Mode-I fracture toughness initiation and propagation values calculated by MBT, CC and MCC methods and corresponding Resistance curves (R-curves) obtained by modified beam theory are given in the Figure 34a and b, respectively. Both initiation and propagation values obtained by these three methods are very close. Since toughness values are slightly changes with the method used for calculations, results and corresponding calculated Resistance curves are shown only for MBT method. The corresponding R-curve has very smooth behavior. Initiation value is very close to  $370 \text{ J/m}^{1/2}$  and propagation values goes up to  $750 \text{ J/m}^{1/2}$  very smoothly.

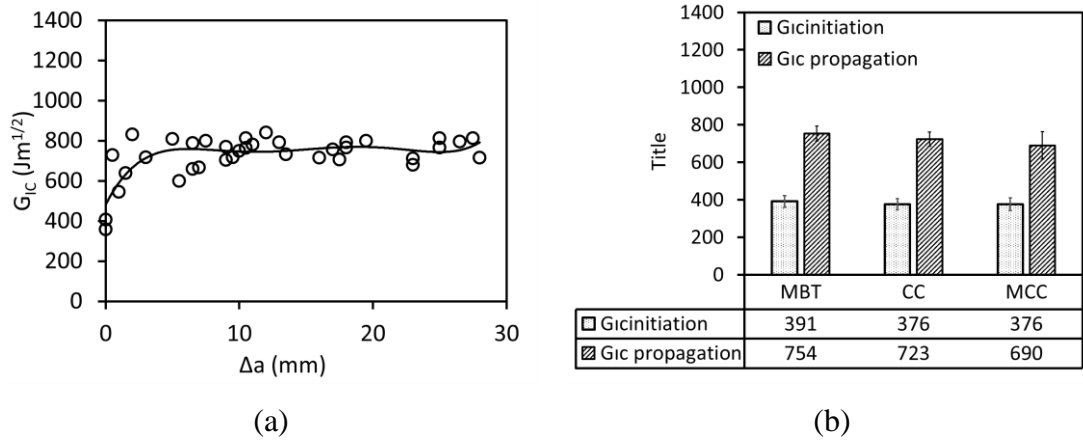


Figure 34 (a) Mode-I fracture toughness ( $G_{IC}$ ) initiation and propagation values obtained by MBT, CC and MBT methods (b) corresponding R-curve for prepreg-fabric laminates based on MBT method.

### 3.2.2. Mode-II Fracture Toughness

Mode-II fracture toughness of the material is obtained by 3-point bending/end notch flexure test. Only  $G_{IIC}$  initiation value is obtained since the test is unstable. In this section load displacement curves and  $G_{IIC}$  values are given for prepreg-fabric laminates.

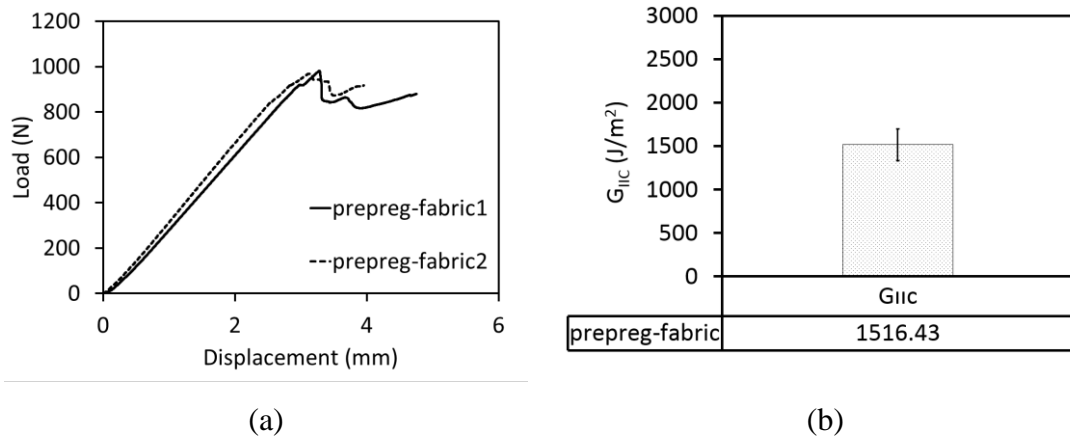


Figure 35 (a) ENF test Load displacement curves of prepreg-fabric laminates, (b) Mode-II fracture toughness results of prepreg-fabric laminates.

Load displacement curves of prepreg-fabric and are given in the Figure 35a. For prepreg-fabric material stiffness slightly changes in two tests. Nonlinearities in the load displacement curves are observed after about 900 N. Crack propagation occurs at nearly 1000 N for prepregs-fabric laminates. Mode-II fracture toughness value

obtained from ENF tests for prepreg-fabric laminates is given as bar graph in Figure 35b.  $G_{IIC}$  value is obtained around  $1500 \text{ J/m}^2$ .

### 3.2.3. Curved Beam Strength

Figure 36 represents 4-point bending load displacement curves of the three prepreg-fabric laminates together. Single load drop is observed for all of the three laminates in the 4-point bending test. Stiffness of the load displacement curve is very close for all of the three tests. Maximum load value prior to failure is very close for the first two tests which is around 2700 N. Failure occurs at 2200 N in the third test. After the load drop load, laminate loses most of its load carrying capacity, which decreases to around 600 N.

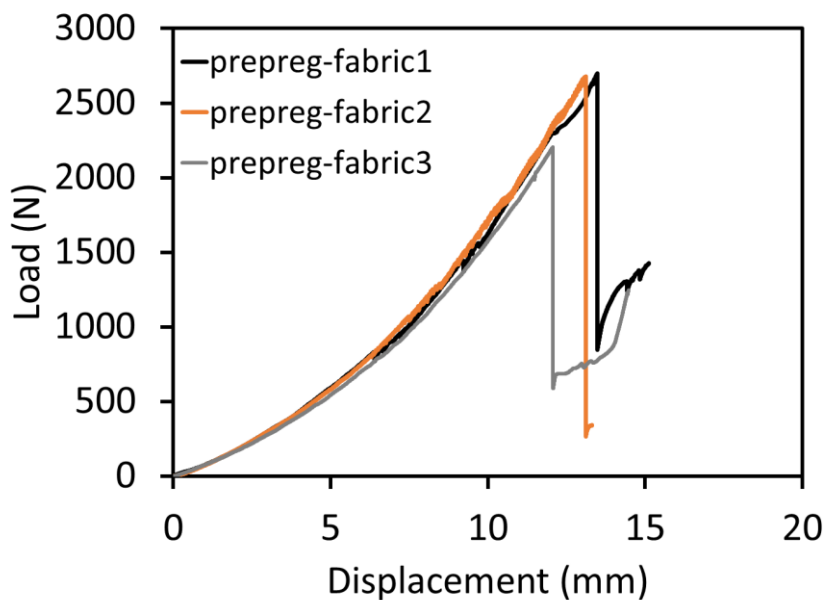


Figure 36 4-point bending test load displacement curves of three prepregs-fabric specimens.

High-speed camera photos captured during delamination initiation and progression for first and third tests are given in Figure 37 and Figure 38, respectively. At the first test images were recorded at 15,000 fps and at the third test images were recorded at 300,000 fps.

Figure 37 shows the failure sequence of prepregs-fabric laminates recorded during the first load drop in which catastrophic failure occurs. First photo in Figure 37 shows the initial view of the specimen prepregs-fabric1. Irregular profile can be seen

at left part of the outer radius. First delamination initiation is observed at this side close to the outer radius between 3<sup>rd</sup> and 4<sup>th</sup> plies which is unusual since maximum stress location under bending at the corner is just below the center line. It is thought that the first delamination initiation can be located at the defect of manufacturing in the specimen. After the first delamination propagates to the both arms, 2<sup>nd</sup> delamination followed by a 3<sup>rd</sup> delamination occur sequentially from the outer radius to the inner radius with a spacing of 3 plies during this single load drop (Figure 36). Discontinuities can be observed in the delamination process due to the waviness of the interfaces in the plain weave fabric plies. Whole process is completed in 2.5 ms. at the last scheme multiple crack are seen at the curved part.

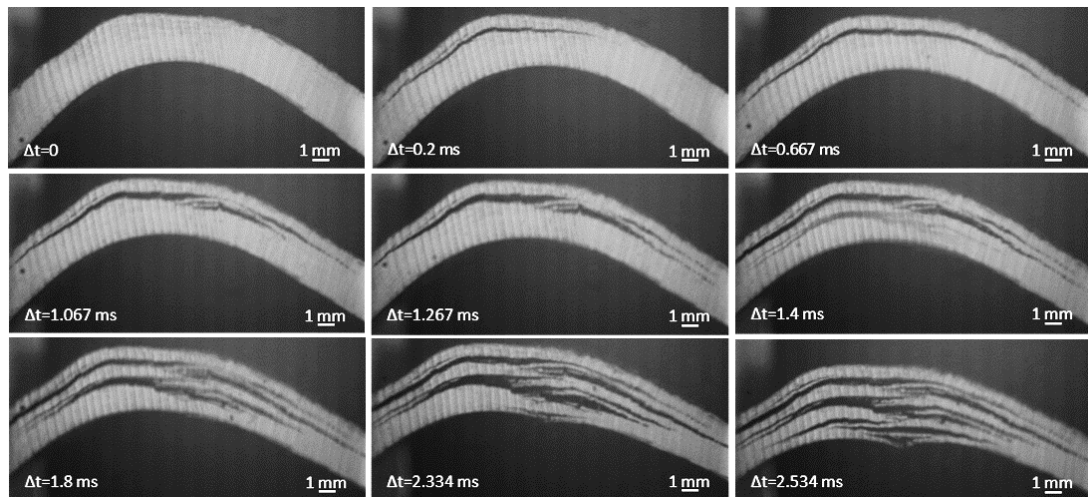


Figure 37 High speed camera images taken at 15,000 fps for the laminate prepreg-fabric1.

In Figure 38 high speed images of prepreg-fabric3 taken at 300,000 fps are shown. First picture of Figure 38 shows the initial state of the specimen. In 3.33  $\mu$ s first delamination occurs between 2<sup>nd</sup> and 3<sup>rd</sup> plies from the inner radius in the left part of the specimen. In the next 3.33  $\mu$ s first crack propagates to the left arm and center of the curved region. In addition to this a second crack initiates one ply above the first crack. For the next 50  $\mu$ s both two cracks continue propagation. After 109  $\mu$ s 3<sup>rd</sup> delamination occurs one ply above the 2<sup>nd</sup> crack at the right part of the specimen. Kinking of the 3<sup>rd</sup> crack to the above ply at the right crack tip is also observed and 2<sup>nd</sup> crack continues propagating to the left side. 4<sup>th</sup> crack is seen at the left part of the specimen at the same ply of the 3<sup>rd</sup> crack after 133  $\mu$ s. 3<sup>rd</sup> and 4<sup>th</sup> crack propagate and

merge. New merged crack splits into two new crack at the right tip and upper part propagates to the right arm. Last crack initiates between 3<sup>rd</sup> and 4<sup>th</sup> ply from the outer radius at the left part of the curved region and propagates for the next 10  $\mu$ s. Whole process takes 476  $\mu$ s and specimen loses most of its stiffness. Although the failure sequences are different, the last schemes of prepreg-fabric1 and prepreg-fabric3 laminates are very similar. Multiple cracks are seen at the curved part and some of the crack propagates through the arms.

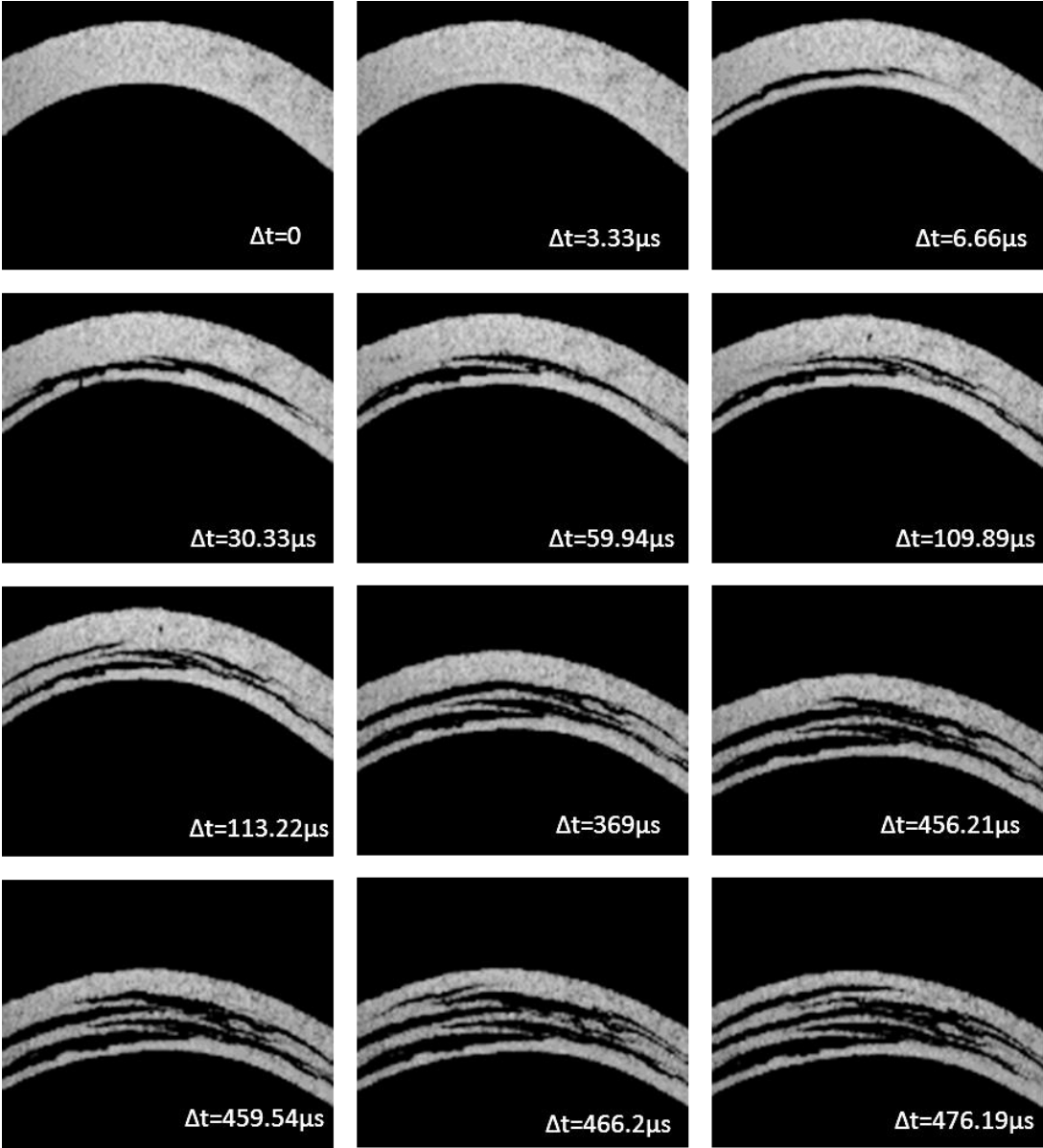


Figure 38 High speed camera images taken at 300,000 fps for the laminate prepreg-fabric3.

In Figure 40 micrograph prepreg-fabric1 laminate is shown. Total failure surface at the curved region is obtained by stitching 60 micrographs together. Many matrix cracks between  $90^0$  fiber filaments can be seen. Different matrix cracks merge between layers. Especially at the mid of the curved region crack kinking is seen clearly. Crack meandering can be observed in the general picture of the curved part.

Figure 39 shows micrographs of the marked locations on the micrograph of curved region. Matrix cracks in the  $90^0$  layers and fiber breakage in the  $0^0$  layers are clearly seen especially at the curved part. The third and fourth pictures splitting of the crack in the  $0^0$  layer into two cracks is observed.

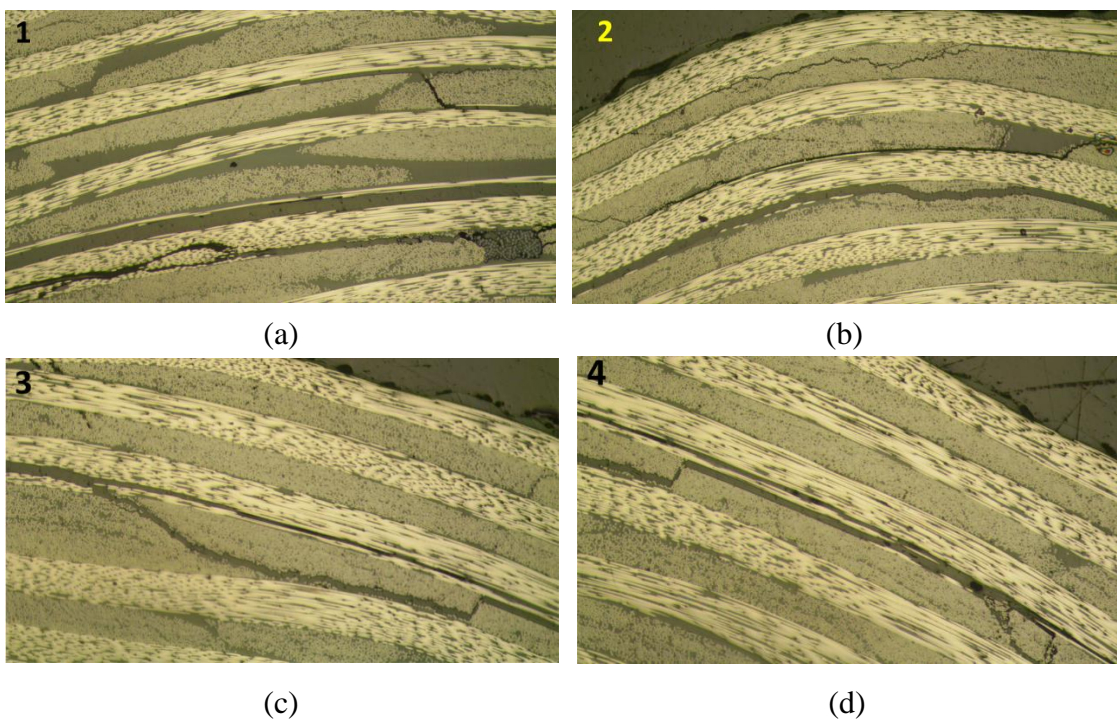


Figure 39 Micrograph of fracture surface of prepregs-fabric1 specimen after the experiment showing marked locations on the micrographs of cracked curved region

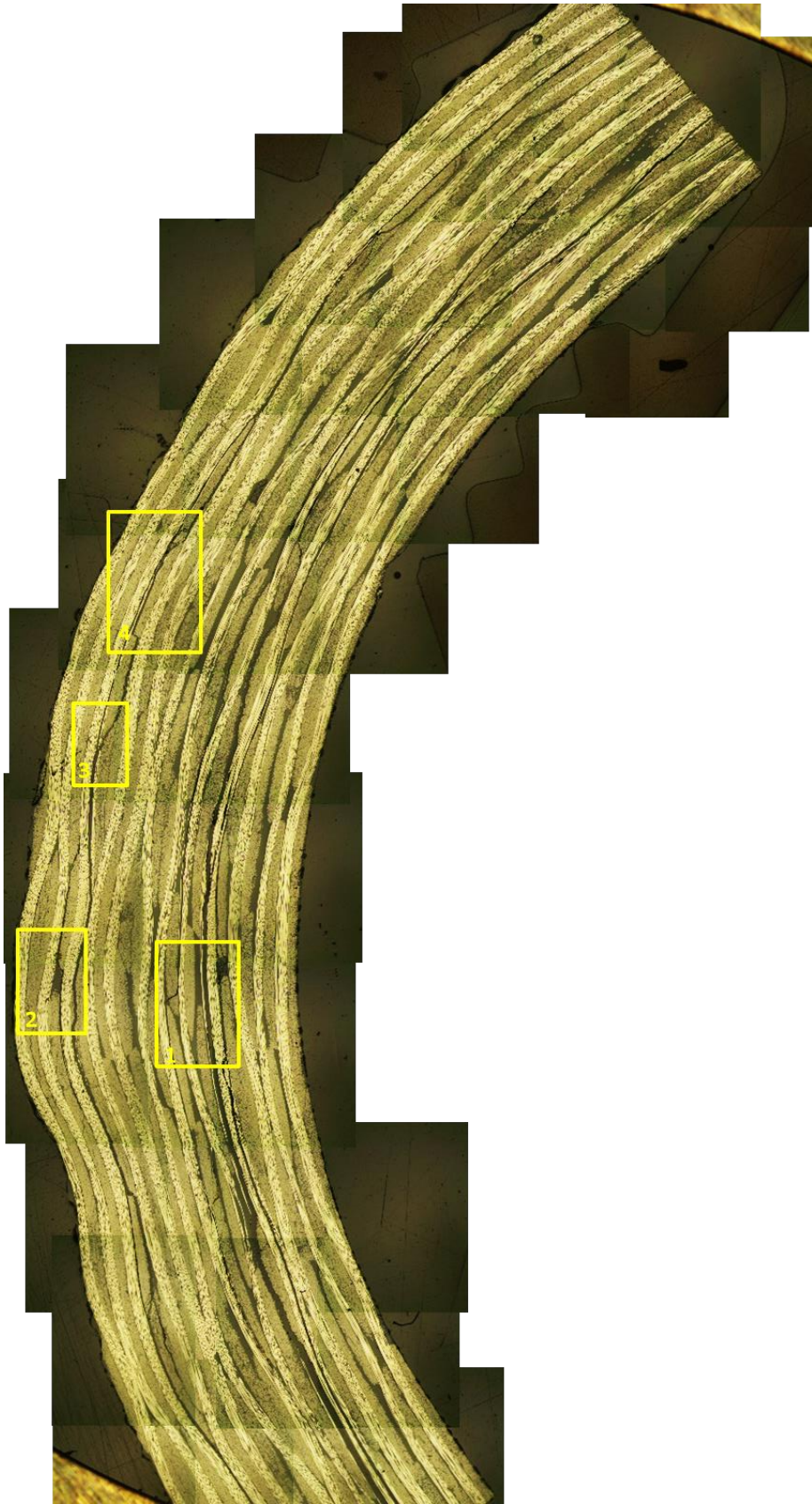


Figure 40 Micrograph of fracture surface of prepreg-fabric1 after the experiment showing cracked curved region

### 3.3. CNT-Fabric Laminates:

#### 3.3.1. Mode-I Fracture Toughness

In Figure 41, load displacement curves obtained in DCB test are presented for CNT-fabric laminates. Variation in stiffness and the maximum loads are observed when load displacement curves of two tests are compared. Around 55 N small load drop is observed for both of the tests. Maximum load varies 80 N to 90 N. Unstable load drops are observed for the first test. After the maximum load, load value at every crack propagation decreases slightly for both of the tests.

Mode-I fracture toughness initiation and propagation values calculated by MBT, CC and MCC and corresponding R-curve obtained by MBT are given in the Figure 42a and b, respectively. Both initiation and propagation values obtained by these three methods are very close and results and corresponding calculated R-curves are shown only for MBT method. In the corresponding R-curve large variation observed for the propagation values. Initiation value is very close to  $450 \text{ J/m}^{1/2}$  and propagation values varies  $600 \text{ J/m}^{1/2}$  to  $1300 \text{ J/m}^{1/2}$ . High scatter in R-curve and propagation values are attributed to dispersion quality of CNTs in the epoxy resin. During resin covering process of hand layup CNTs might be concentrated in clusters and agglomerated with high density which can result in heterogeneity in laminate and non-isotropic mechanical properties.

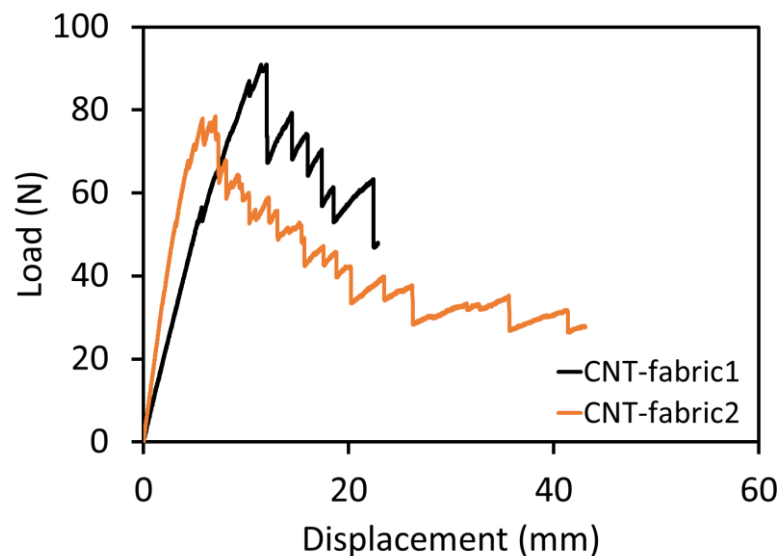
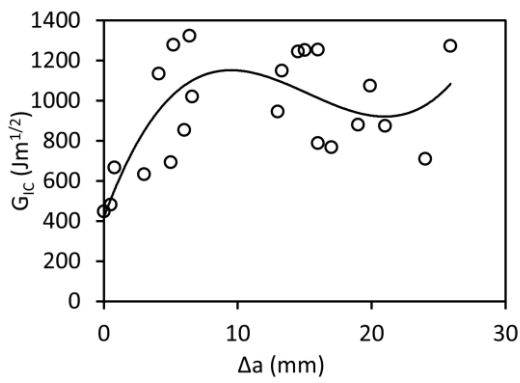
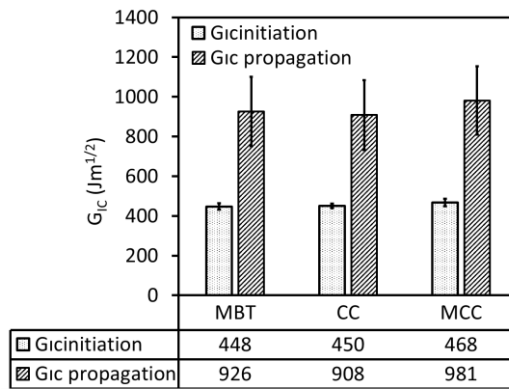


Figure 41 DCB test load displacement curves of CNT-fabric laminates.

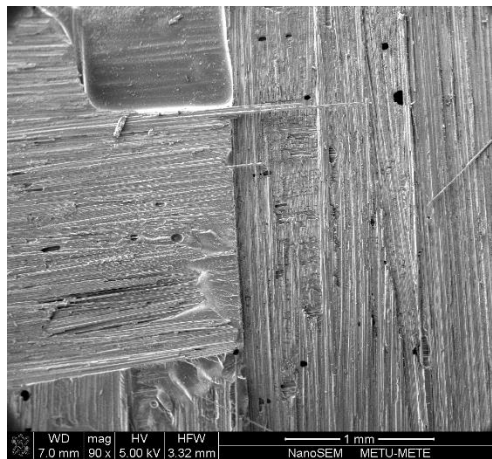


(a)

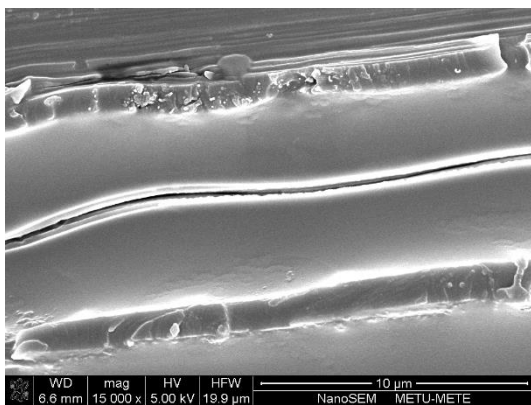


(b)

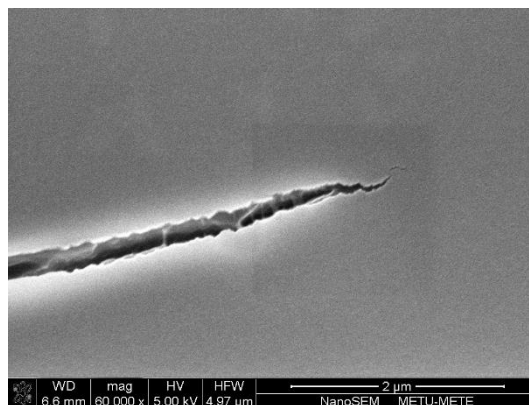
Figure 42 (a) Mode-I fracture toughness ( $G_{IC}$ ) initiation and propagation values obtained by MBT, CC and MBT methods (b) corresponding R-curve for CNT-prepreg laminates based on MBT.



(a)



(b)



(c)

Figure 43 SEM images of CNT-fabric2 specimen after DCB test showing (a) general view of fracture surface, (b) closer look on the epoxy region showing the agglomerated CNTs and (c) CNT bridging at the crack tip.

In Figure 43 SEM images of CNT-fabric2 specimen after DCB test is presented. Fracture surface of CN-fabric laminate has rough behavior. Local defects and fiber breakage is observed in Figure 43a. In Figure 43b microcracks in the epoxy region are observed and agglomerated CNTs can be seen. In Figure 43c tip of the microcrack is presented. At the crack tip CNT bridging is seen which can improve the resistance against crack propagation.

### 3.3.2. Mode-II Fracture Toughness

Mode-II fracture toughness of the material is obtained by 3-point bending/end notch flexure test. Only  $G_{IIC}$  initiation value is obtained since the test is unstable. In this section load displacement curves and calculates  $G_{IIC}$  values are given for CNT-fabric laminates.

Load displacement curves of CNT-fabric laminates are given in Figure 44a. For CNT-fabric material stiffness slightly changes in two tests. For the CNT-fabric laminates failure occurs at 1200 N. For the CNT-prepreg laminates sudden load drop are observed. Delamination propagation occurs at different displacement values. Mode-II fracture toughness values obtained from ENF tests for CNT-fabric laminates are given as bar graph in Figure 44b. 22% higher Mode-II fracture toughness value is obtained for CNT-fabric laminates. High scatter is seen for the CNT-fabric laminates compared to prepreg-fabric laminates.

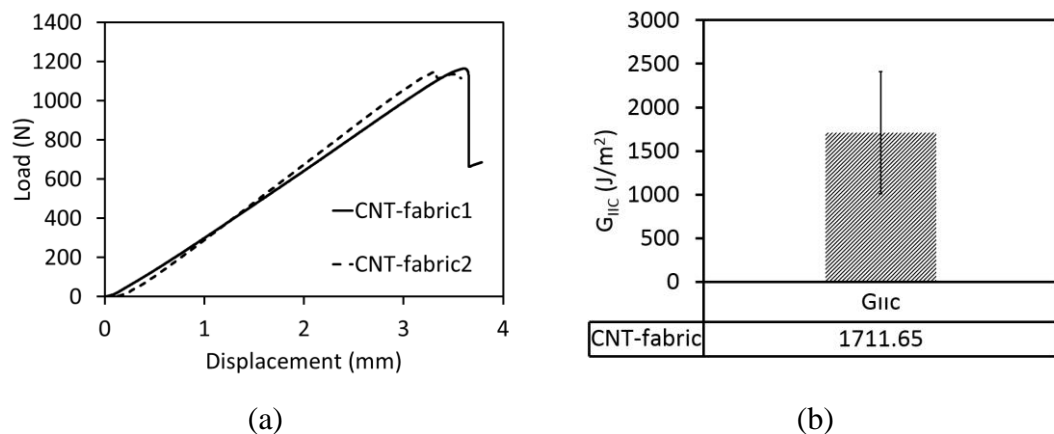


Figure 44 (a) ENF test Load displacement curves of CNT-fabric laminates, (b) Mode-II fracture toughness results of CNT-fabric laminates.

**3.3.3. Curved Beam Strength**

Figure 45 represents 4-point bending load displacement curves of the three [0/90] fabric CNT added laminates. Stiffness of the load displacement curve of three tests are very close. Maximum load value prior to catastrophic failure is varying between 1300N and 1800N. In the 4-point bending load displacement curve of CNT added laminates two load drops are observed for all of the three tests. First load drop occurs at different values for each test. After the first load drop specimens continue carrying load without changing their stiffnesses up to certain point. After the second load drop load carrying capacity decreases to 400N.

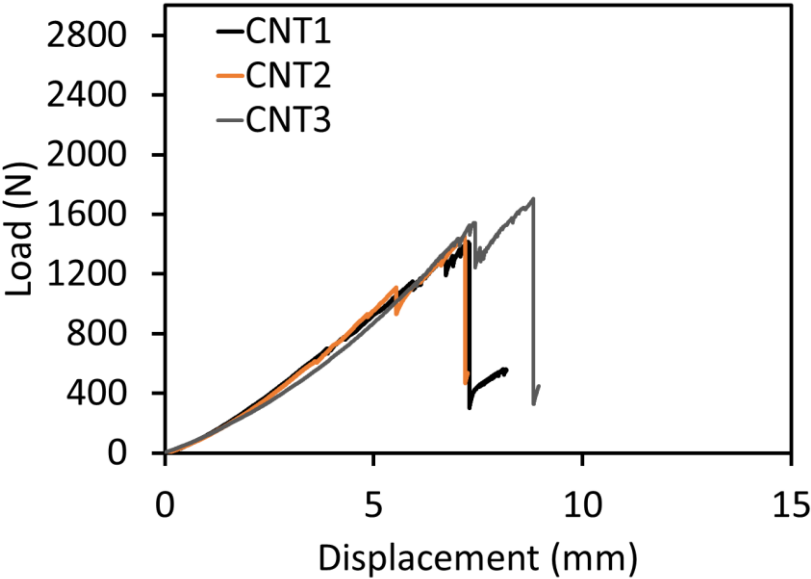
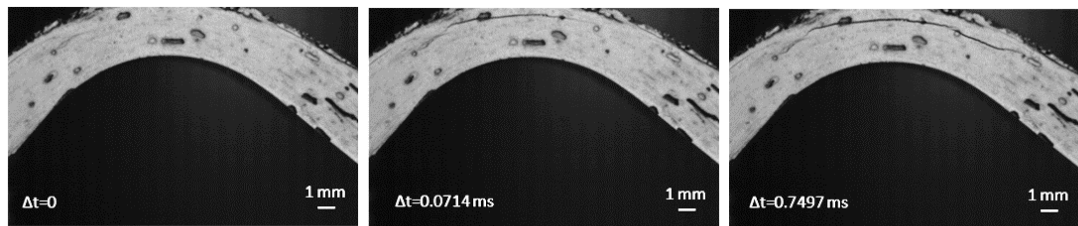


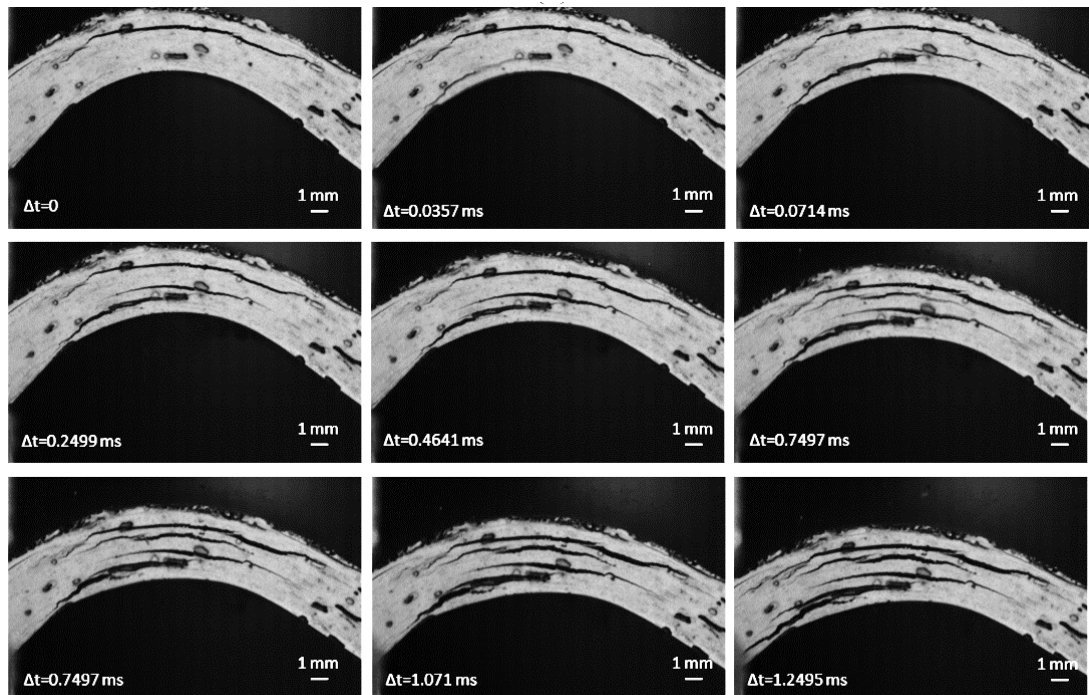
Figure 45 4-point bending test load displacement curves of three CNT-fabric specimens

In Figure 46a and Figure 46b, failure sequence of CNT-fabric laminates, captured at 28,000 fps, at first and second load drop are given, respectively. At the first load drop single delamination initiation is observed between 2nd and 3rd plies from to the outer radius. At this small load drop crack propagates slightly through both arms before arresting. After loading the material again, further delamination sequence is observed at the second load drop as shown in Figure 46b. During this load drop, initial delamination continues to propagate and a second crack initiates at the last ply and propagates diagonally between different laminates. Third crack occurs above the second crack close to mid layer. Fourth crack initiates between first and third

delamination and kinking can be clearly seen. However, between the major cracks, secondary cracks tend to mend. This behavior is attributed to the weak CNT clustered regions which can change the interlaminar crack paths. No merging cracks or fiber bridging is observed and total delamination sizes are smaller compared to prepregs-fabric laminates possibly due to arresting of cracks in the corner region by the CNT clusters or manufacturing defects.



(a)



(b)

Figure 46 High speed camera images at 28,000 fps for CNT added laminate at (a) first load drop and (b) second load drop.

In Figure 47 micrograph of CNT added laminate after the test is shown. In this case it is thought that cracks between layers originate from the vacancies in the specimens. Reposition and concentration of CNTs in clusters with high density may cause the heterogeneity in the epoxy resin corresponding vacancies.



Figure 47 Micrographs of fracture surface after the experiment showing CNT-fabric2 laminate.

### 3.4. Discussion

In this section experimental results of prepregs-fabric and CNT-fabric laminates are given together for comparison. Firstly, fracture toughness test load displacement curves and calculated  $G_{IC}$  and  $G_{IIC}$  values are presented together. Then 4-pt bending load displacement curves are given together for comparison. Curved beam strength and maximum radial stress values are presented. At the last section final discussion are made by comparing photos of failed specimens according to the information obtained throughout the comparison.

#### 3.4.1. Fracture Toughness Results

Figure 48 a and b shows the load displacement curves of DCB and ENF tests for prepregs-fabric and CNT fabric laminates together. For the DCB test, stiffness of the CNT-fabric laminate is higher than the prepregs-fabric laminate and similar behavior is observed for both material. Load displacement curves for ENF tests of prepreg-fabric and CNT-fabric laminates are given in Figure 48b. In the load displacement curves small stiffness change in between two materials is observed. 20% higher maximum load values are observed for the CNT-fabric laminate. When load displacement curves of two materials are compared, maximum load at delamination propagation is higher for CNT-fabric laminate.

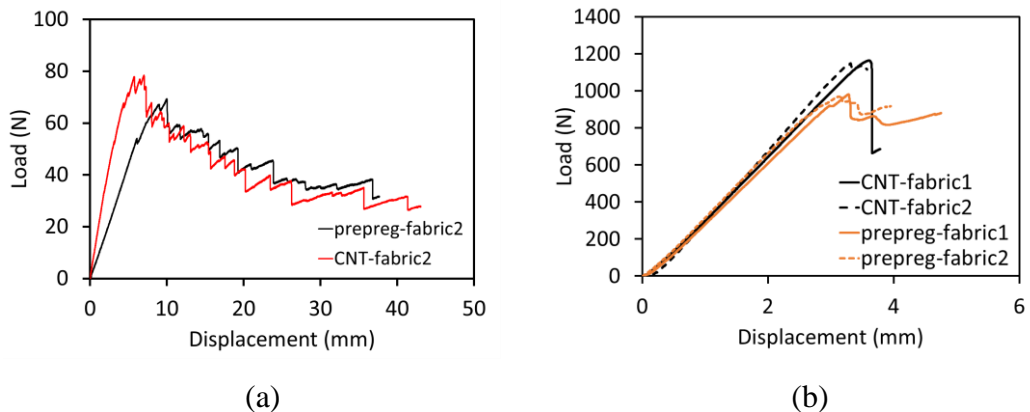


Figure 48 Load displacement curves of prepreg-fabric and CNT-fabric laminates obtained from (a) DCB test and (b) ENF test

In Figure 49a and b effect of load displacement behavior can be seen in R-curve given for prepreg-fabric and CNT-fabric laminates, respectively. R-curve of prepreg-fabric laminate (Figure 49) is uniform and regular with low variation while in the resistance curve of CNT-fabric specimen has irregular rough behavior and high

variation can be seen. Possible reason for higher toughness seen in CNT-fabric laminates could be that clusters act as crack arresters when it first initiated the load increased to a very high value before delamination proceeded again. A lot of energy stored before crack propagates dynamically with a high stored energy released leading to significant load drop. This reason can cause variation in R-curve.

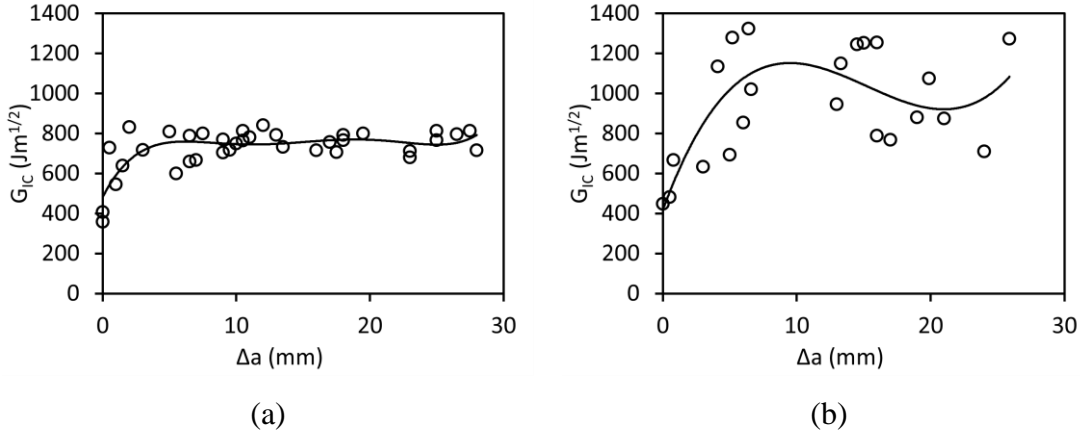


Figure 49  $G_{IC}$  Resistance curves for (a) prepreg-fabric and (b) CNT-fabric laminates.

The bar graph of Mode-I fracture toughness initiation ( $G_{ICinitiation}$ ) and propagation ( $G_{ICpropagation}$ ) values obtained by modified compliance calibration method for prepreg-fabric and CNT-fabric laminates are given in Figure 50 a and b, respectively. For the CNT-fabric specimen 25% and 33% higher Mode-I fracture toughness initiation propagation values are observed, respectively. Bar graph of Mode I fracture toughness values of prepregs-fabric and CNT-fabric laminates obtained using direct beam theory are given in Figure 50a. 10% higher values of Mode-II fracture toughness is observed CNT-fabric laminates with much higher scatter in the Mode-II toughness values as was also observed in DCB tests. The large scatter and the increase in fracture toughness value for CNT added laminates can be attributed to scatter in the interface properties of the CNT-fabric laminates caused by the agglomerations of CNTs along the interface.

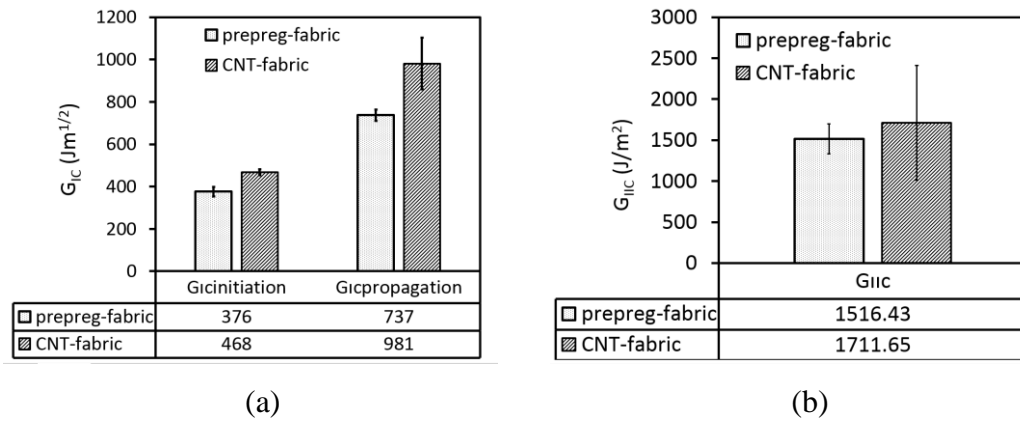


Figure 50 (a) Mode- I fracture toughness initiation and propagation values (b) Mode-II fracture toughness values of prepreg-fabric and CNT-fabric laminates.

In Figure 51a and b SEM images of fracture surfaces after the DCB test is shown for prepreg-fabric and CNT-fabric laminates, respectively. The fracture surface of prepreg-fabric laminate is uniformly separating between the fabric layers. In the CNT-fabric laminate surface holes are observed in epoxy region and in some cases local regions of fiber separation are observed. Thus, in the CNT added laminate, heterogeneity of delamination is observed increasing the area of fracture.

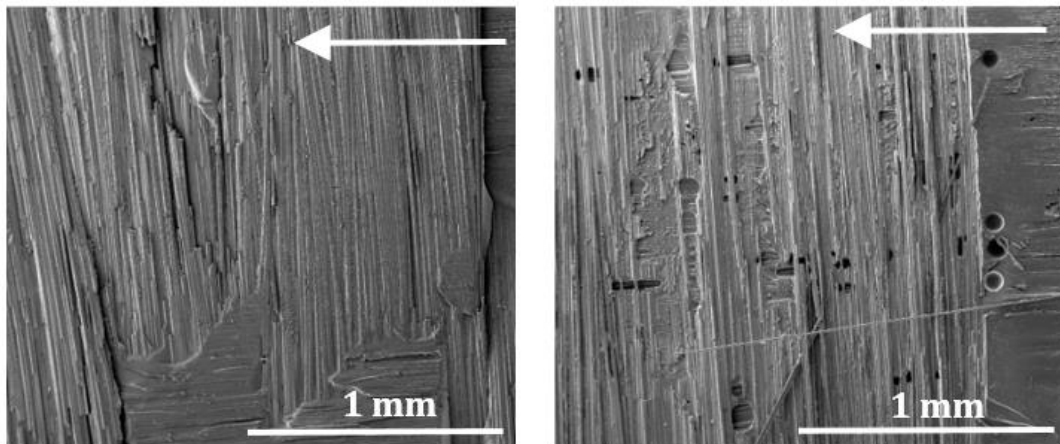


Figure 51 SEM images of fracture surfaces after DCB test for (a) for prepreg-fabric and (b) CNT-fabric laminates, arrow indicates the crack growth direction.

### 3.4.2. Curved Beam Strength Results

Load-displacement curves of the 4-pt bending test for both the prepreg-fabric material (red line) and CNT-fabric material (black line) are shown in Figure 52. Results for two prepreg-fabric materials and three CNT added materials are shown. In comparison with prepreg-fabric material, stiffness is found to be higher for CNT-

fabric laminate, however, the failure load is found to be less for CNT-fabric laminate. Prepreg-fabric laminates can stand up to 2700 N and failure occurs at one load drop. In contrast to prepreg-fabric material, two load drops are observed for the CNT-fabric laminates. At the first load drop initial delamination occurs close to the upper edge of the specimen and it continues carrying load up to the second load drop without changing slope. For CNT-fabric laminates maximum load prior to failure is lower than the prepreg-fabric material, varying between 1500 and 1700 N. Scatter in the maximum load value of first and second load drop for the CNT-fabric laminates supports the claim that non-uniform dispersion of CNTs during manufacturing might be leading to heterogeneous distribution and clumping of CNTs in the resin and property variation between different specimens.

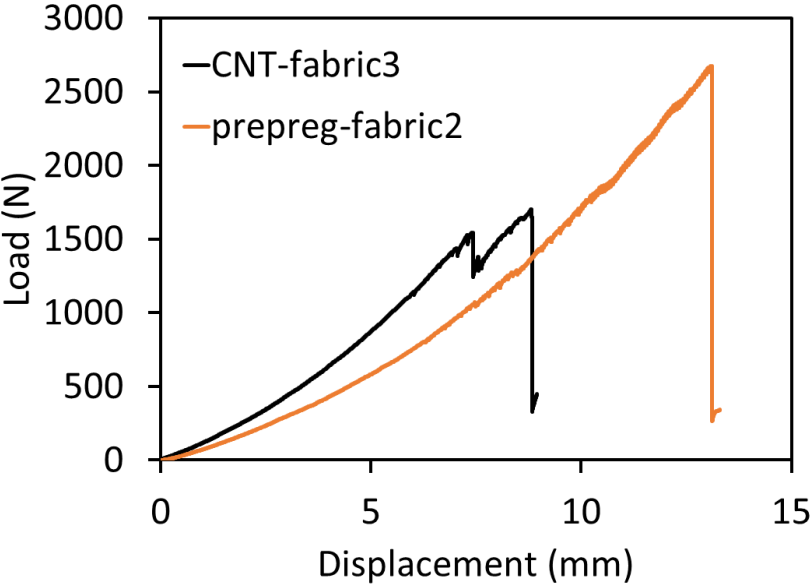


Figure 52 Load displacement curves of 4-pt bending test for prepreg-fabric and CNT-fabric laminates together.

Curved beam strength (CBS) and maximum radial stress calculations for prepreg-fabric and CNT-fabric laminates together are shown in Figure 53a and b, respectively. The CBS value and the radial stress value are found to be 64% and 50% percent less than the prepreg-fabric laminates for the CNT-fabric laminates. These results are in contrast to Avalon’s study [33] where no effect of CNT addition on CBS and radial stress was observed. Mean value of curved beam strength of prepreg-fabric laminate is about 800 N-mm/mm while CNT additions decreases the strength

to 400 N-mm/mm. Large scatter for the CNT-fabric laminates compared to the prepreg-fabric laminates is also seen in 4-point rest results. Decrease in the maximum load decreases the strength and variation in maximum load leads to scatter in the results. These results also support the claim that reposition and concentration of CNTs in clusters with high density can lead to heterogeneities in the plies and non-isotropic mechanical properties that leads to variation and degradation in strength. In addition, decrease in the maximum radial stress is higher than CBS.

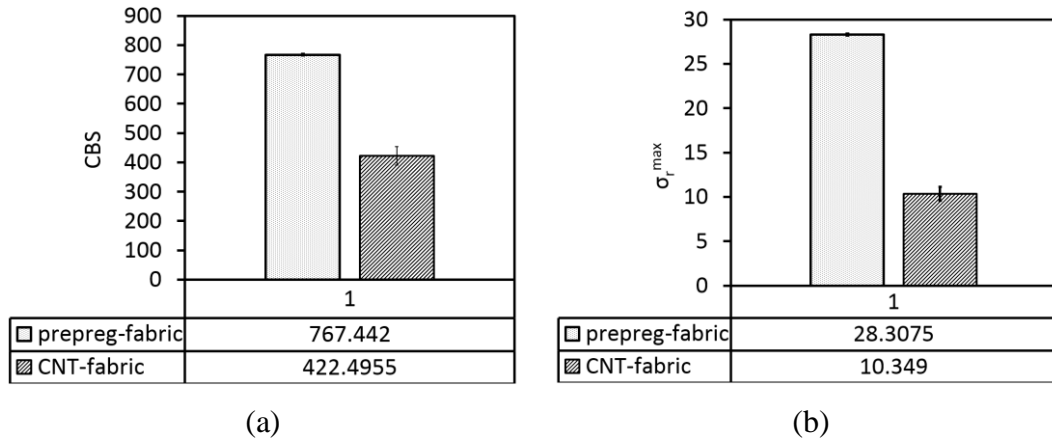


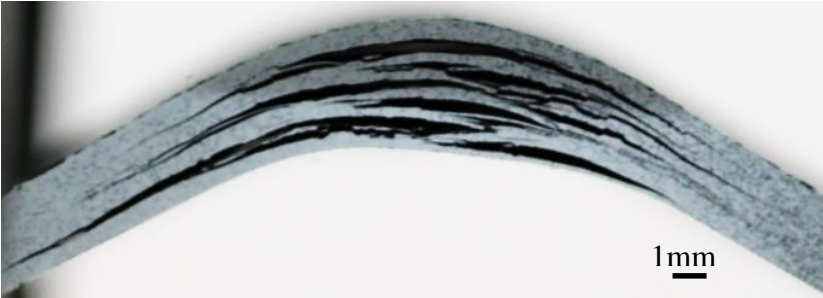
Figure 53 (a) Curved beam strength, (b) maximum radial stress results of prepreg-fabric and CNT-fabric laminates together.

### 3.4.3. Final Discussions

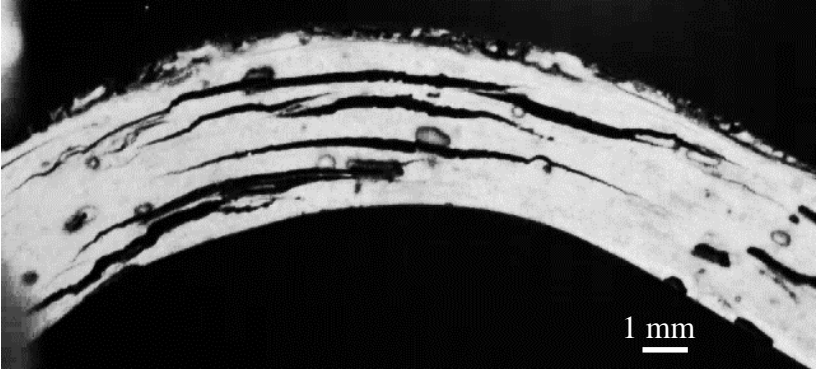
In this section final conclusions are made based on the comparison of the photos of failed specimens for prepreg-fabric and CNT-fabric materials. All the information obtained up to this point are combined and some further discussions are made in order to gain more understanding of this study.

Final cracked surfaces of prepreg-fabric and CNT-fabric laminates are given in Figure 54a and b, respectively. Totally cracked curved region is observed for the prepreg-fabric material. Cracks exceed the curved part and extend to the arms. For the CNT-fabric laminates less delamination is seen compared to prepreg-fabric laminate. The most significant difference is that the crack lengths in the CNT-fabric laminate is smaller than prepreg-fabric material. For the CNT-fabric laminates cracks reach up to end of the curvature. Smaller crack lengths can be associated to the fracture toughness of the material. Since fracture toughness values of the CNT-fabric material (Figure 50) is higher than the prepreg-fabric material, more energy is

required to propagate the crack and cracks propagate slower. However, the conclusions are not only dependent on the addition of CNT but also can be a function of the different manufacturing techniques used to produce prepreg vs. dry fabric specimens. In the future, a comparison should be made with dry 0/90 fabric as a baseline material when it becomes available to isolate the effect of CNT addition.



(a)



(b)

Figure 54 Photos of the prepreg-fabric3 and CNT3 laminates after the test showing the cracked curved regions (a) prepreg-fabric specimen, (b) CNT-fabric specimen.

## CHAPTER 4

### COMPARISON OF THE FAILURE OF THIN PLY NON-CRIMP FABRIC AND UNIDIRECTIONAL LAMINATES

In this chapter, Mode-I and Mode-II fracture toughness and curved beam strength results are presented for thin ply NCF and unidirectional CFRP composite laminates. Effect of stacking sequence on the fracture toughness of same delamination interface is discussed by comparing the results of [0/45/-45/0] and [0] unidirectional composite laminates. Fracture toughness and curved beam strength results are then compared with the results of thin ply non-crimp fabric laminates.

Firstly, the materials and manufacturing process to obtain the specimens for two types of unidirectional and thin ply non-crimp fabric laminates are presented. The results are presented in the following order for each material: Mode-I and Mode-II fracture toughness tests, curved beam strength tests, high speed camera images of failure process, and micrographs of failed specimens. Finally, the results of all types of laminates are compared in the discussion section.

#### 4.1. Specimen Preparation

##### 4.1.1. Material

The term thin ply non-crimp fabric is used for fabric type layers with less waviness and reduced ply thickness. Thin ply NCF are formed by stitching the tow spread thin UD layers in the desired configuration instead of weaving the filaments. In this study thin ply NCFs are composed of 12 plies and each one of these plies is composed of 4 plies stitched together in the [0/45/-45/0] configuration.

For thin ply non crimp fabric studies Choromat C-Ply (carbon fiber T700) NCF and UD prepregs with AR2527 epoxy resin produced by Aldita composite materials are used. C-Ply NCFs have 0.0625 mm ply thickness which is half of the common UD ply thickness. Material properties of non crimp fabric prepregs and equivalent UD prepregs are given in Table 4 and table 5, respectively [48]. Toray T800 carbon fiber

tows are used for C-Ply NCF material . The term thin ply non-crimp fabric is used for fabric type layers with less waviness and reduced ply thickness. Thin ply NCF are formed by stitching the tow spread thin UD layers in the desired configuration instead of weaving the filaments. In this study thin ply NCFs are composed of 24 plies and each having 2 thin plies tied together by stitching in the [0/45] configuration. And this NCF plies are stacked in the order of [0/45/-45/0]<sub>12T</sub> stacking sequence. Material properties of [0] thin ply NCF and [0] UD laminates are given in the NC and table 6, respectively [49].

Table 5 properties of thin ply NCF

**HR40-AR2527-80/40 [0] prepreg Properties**

<b>E<sub>11</sub></b> <b>(GPa)</b>	<b>E<sub>22</sub></b> <b>(GPa)</b>	<b>G<sub>12</sub></b> <b>(GPa)</b>	<b>v<sub>13</sub></b>	<b>Density (kg/m<sup>3</sup>)</b>	<b>Cured ply thickness (mm)</b>
206.8	40.6	14	0.30	1820	(0.0828mm)

Table 6 properties of [0] unidirectional fiber

**34-700-AR2527-190/35 [0] prepreg Properties**

<b>E<sub>11</sub></b> <b>(GPa)</b>	<b>E<sub>22</sub></b> <b>(GPa)</b>	<b>G<sub>12</sub></b> <b>(GPa)</b>	<b>v<sub>13</sub></b>	<b>Density (kg/m<sup>3</sup>)</b>	<b>Cured ply thickness (mm)</b>
180.6	37	21	0.30	1800	(0.178mm)

The production of C-Ply NCF consists of three phases as follows [47]:

Tow spreading: In this method filaments in an original thick tow are spread uniformly by passing through very low, stable airflow between the filaments. The tow sags downward and loses tension with the flow of air. As air passes through the filaments in the downward direction from air duct to vacuum, it creates pressure difference around fibers and distributes them as shown in Figure 55a. The setup and

schematic of methodology to distribute the fibers are given in the Figure 55 a and b, respectively.

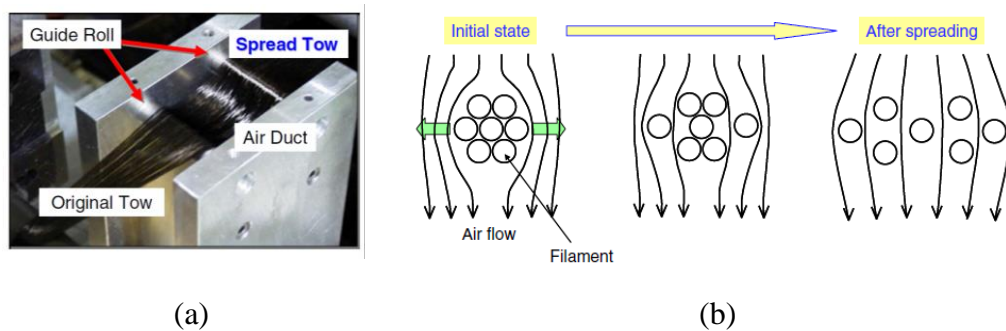
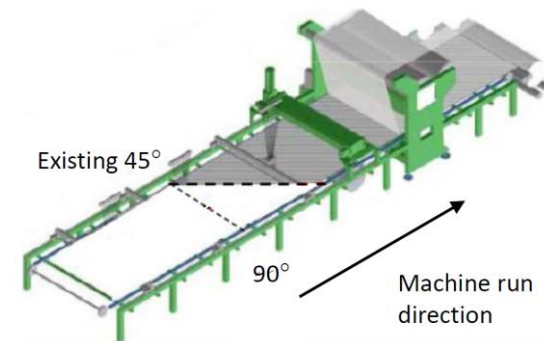


Figure 55 (a) Tow spreading device, (b) schematic of tow-spreading process [47]

*Ply forming:* In this part plies of non-crimp fabrics are formed. Main difference between conventional fabric and non-crimp fabrics is the ply forming phase. Instead of weaving the tows, NCF are formed by placing the spread tow UD plies on top of one another in the desired directions on a multiaxial machine. The schematic of the machine forming plies in the  $45^{\circ}$  direction are presented in Figure 56a and obtained thin plies and prepregs are presented in Figure 56b.



(a)



(b)

Figure 56 (a) The schematic of the machine forming plies in the  $45^{\circ}$  direction and (b) thin plies obtained with the tow spreading technology at Chomarar [35].

Combining: in this final part Non-crimp fabrics are formed by consolidating the thin UD plies in the desired direction. Plies are tied together with a very fine stitch as shown in the Figure 57. Stitching is a substantial part of the manufacturing process, very fine stitching is done in order to reduce the impact of foreign materials and the creation of voids as much as possible. Schematic representation of combining process of the NCF ply is shown in Figure 57.

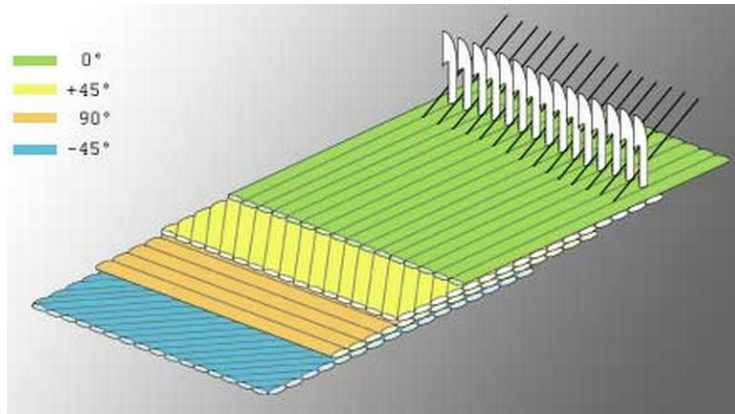


Figure 57 Ply combining process schematic of thin ply NCF laminates during manufacturing.

#### 4.1.2. Specimen Geometry

Both unidirectional and thin ply NCF fracture toughness test specimens were manufactured together and 4-point bending test specimens were manufactured separately. Specimen geometries of 4-point bending test and fracture toughness tests are shown in Figure 58a and b, respectively. Thin fiber non-crimp fabric specimens are in the  $(0/-45/45/0)_{12T}$  stacking sequence which corresponds 48 plies of thin fiber plies and 24 plies of  $[0/45]$  thin NCF plies with 3.5 mm thickness. Unidirectional specimens has 0.17 mm thick plies manufactured with  $(0/-45/45/0)_{6T}$  layup corresponding 24 plies with 3.5 mm thickness. L-shaped specimen's leg lengths were 100 mm and inner radius was 10 mm. Flat plates are 260 mm in length and approximately 150 mm wide having 63 mm and 50 mm pre-cracks for DCB and ENF test, respectively. Flat plates were cut using water jet and L-beams were cut by diamond saw cutting machine at METKON Company in BURSA using SERVOCUT 501.

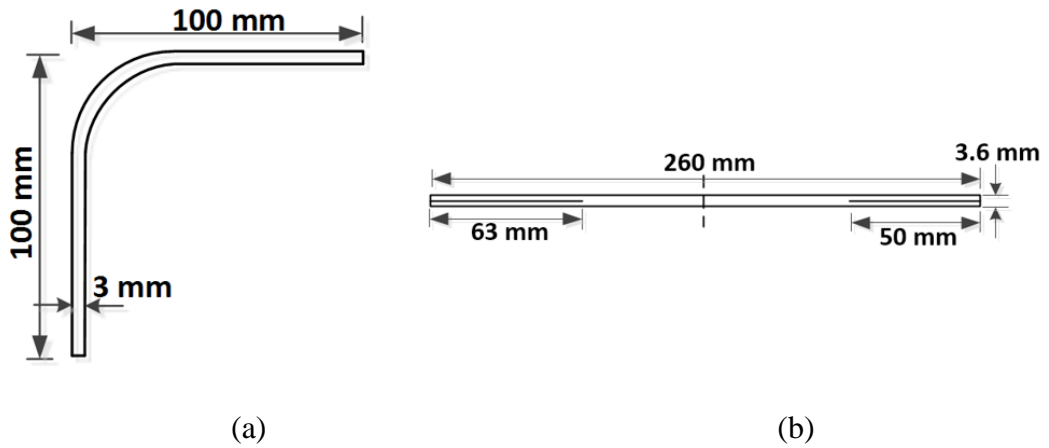


Figure 58 Specimen geometry of thin fiber NCF used for (a) 4-point bending tests and (b) fracture toughness tests.

#### 4.1.3. Manufacturing:

L-shaped specimens and flat plates were manufactured by hand lay-up technique in Sabanci University. Two types of tool was used in this manufacturing process. In Figure 59a first tool is presented which is made of steel. The surface quality of this tool was not sufficient, especially at the curved part. Since material was steel, the tool was very heavy and lay up process was very hard. The manufacturing quality of the specimens were not sufficient, so second batch for all types of specimens are manufactured with an aluminum tool same as the tool used for CNT studies.

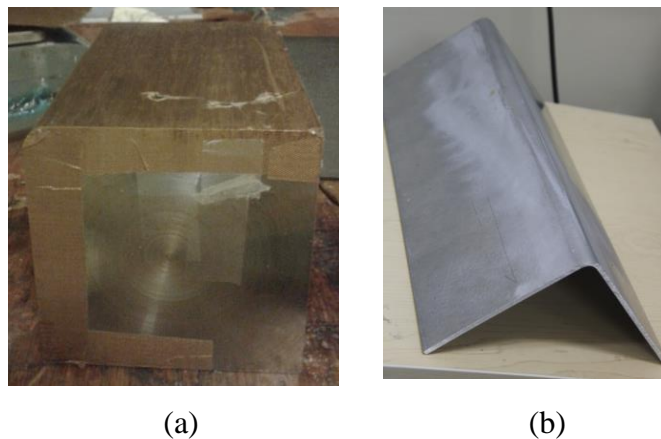


Figure 59 Tools used for manufacturing of (a) first batch, (b) second batch.



(a)

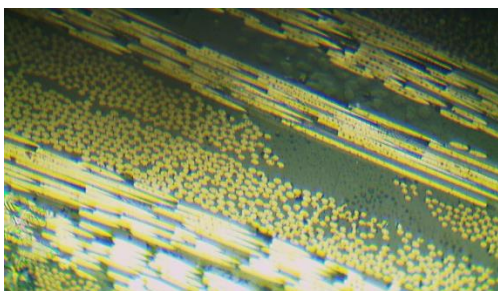


(b)

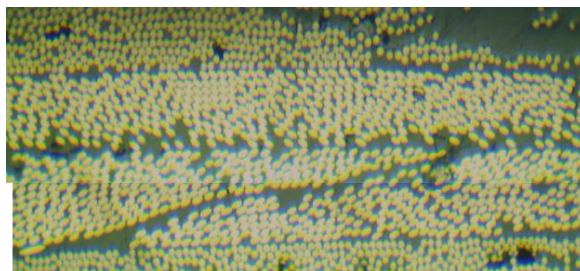
Figure 60 (a) Laid up thin fiber prepregs on the tool used for first batch, (b) oven used for curing process for laid up prepregs in vacuum bag.

Firstly tool was covered with the separator type then prepregs were laid up on the tool. After the layup process the tool was put into vacuum bag and just after it placed into oven at 135 C for 6 hours. After curing process L-shaped plates were cut by toothed diamond saw at Sabancı University.

Figure 61 a and b represents the microscopic view of thin-ply NCF material showing the stacking stitched thin UD plies in the direction of  $[0/45/-45/0]$  from thickness and width directions, respectively.



(a)



(b)

Figure 61 Microscopic view of  $[0/45/-45/0]$  thin ply NCF (a) in the thickness direction, (b) in the width directions.

## 4.2. [0] and [0/45/-45/0] Unidirectional Laminates

### 4.2.1. Mode-I Fracture Toughness

Load displacement behavior of [0] unidirectional specimens have very smooth behavior as shown in Figure 62a. In the first part of the experiment was stopped after 3 mm crack growth. After the unloading, specimen was loaded again up to 25 mm crack propagation. Load values stay nearly level as crack continuously propagates for the specimen [0] UD1. Stable delamination propagation is observed and maximum load value reaches 45N. First delamination propagation occurs at 43 N. Unstable crack growth was observed after 23 mm propagation. For the [0] UD2 and [0] UD3 specimens load displacement behavior is different than the [0] UD3 specimen. Initiation occurs at higher values very close to 55N. More unstable load drops are observed compared to [0] UD1 specimen. Moreover, load values stay nearly level as crack continuously propagates for the specimen [0] UD1, load value slightly increases for the [0] UD2 and [0] UD3 specimens.

Two load displacement curves of [0/45] UD specimens are presented in Figure 62b. High load drop occurred at the initiation at 40 N for both of the specimens. Slope of the curves and behaviors are exactly same, small deviation of the maximum displacement at the initiation is the only difference. Only at the initiation higher load drop is observed, then load decreases slightly as crack propagates for both of the specimens. Very stable delamination growth occurred for all tests. Load value could reach 37 N at most. Compared to [0] UD laminates, initiation occurs at lower load values for the [0/45] UD laminates. Load displacement behavior changes as layup s changed, for the [0/45] UD laminates at the initiation higher load drop is observed, then load decreases slightly as crack propagates for both of the specimens as More unstable load drops and slightly increasing load value are observed for the [0] unidirectional laminates in out of three tests.

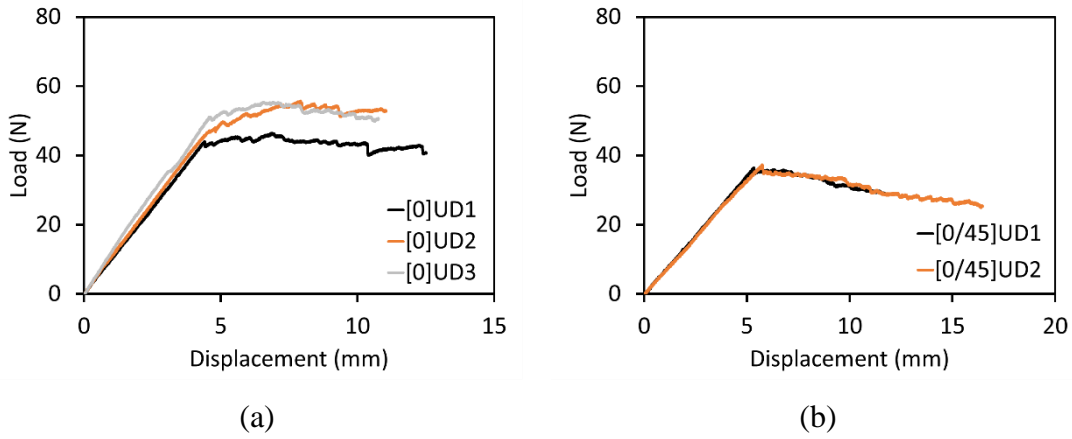


Figure 62 DCB load displacement curves of three tests of (a) [0] UD and two tests of (b) [0/45/-45/0] UD laminates.

Bar graph of Mode-I fracture toughness initiation and propagation values calculated by MBT, CC and MCC for [0] UD and [0/45] UD laminates are given in the Figure 63a and c respectively. Both initiation and propagation values obtained by these three methods are very close for the [0] UD and [0/45] UD laminates. Since toughness values are slightly changes with the method used for calculations, results and corresponding calculated Resistance curves are shown only for MBT. The corresponding resistance curves are presented in Figure 63 a and c for the [0] UD and [0/45] UD laminates, respectively. For both of the layup type R-Curve has very smooth behavior. Initiation value is very close to  $210 \text{ J/m}^{1/2}$  and propagation values goes up to  $290 \text{ J/m}^{1/2}$  for the [0] UD laminates. For the [0/45] UD laminates initiation and propagation values slightly decreases compared to [0] UD laminates. Initiation value is  $200 \text{ J/m}^{1/2}$  and propagation values increases up to  $250 \text{ J/m}^{1/2}$  and the difference between the initiation and propagation values are very low. Although delamination propagation interface is 0/0 for both types of UD laminates, low increase in the GIC propagation values are observed.

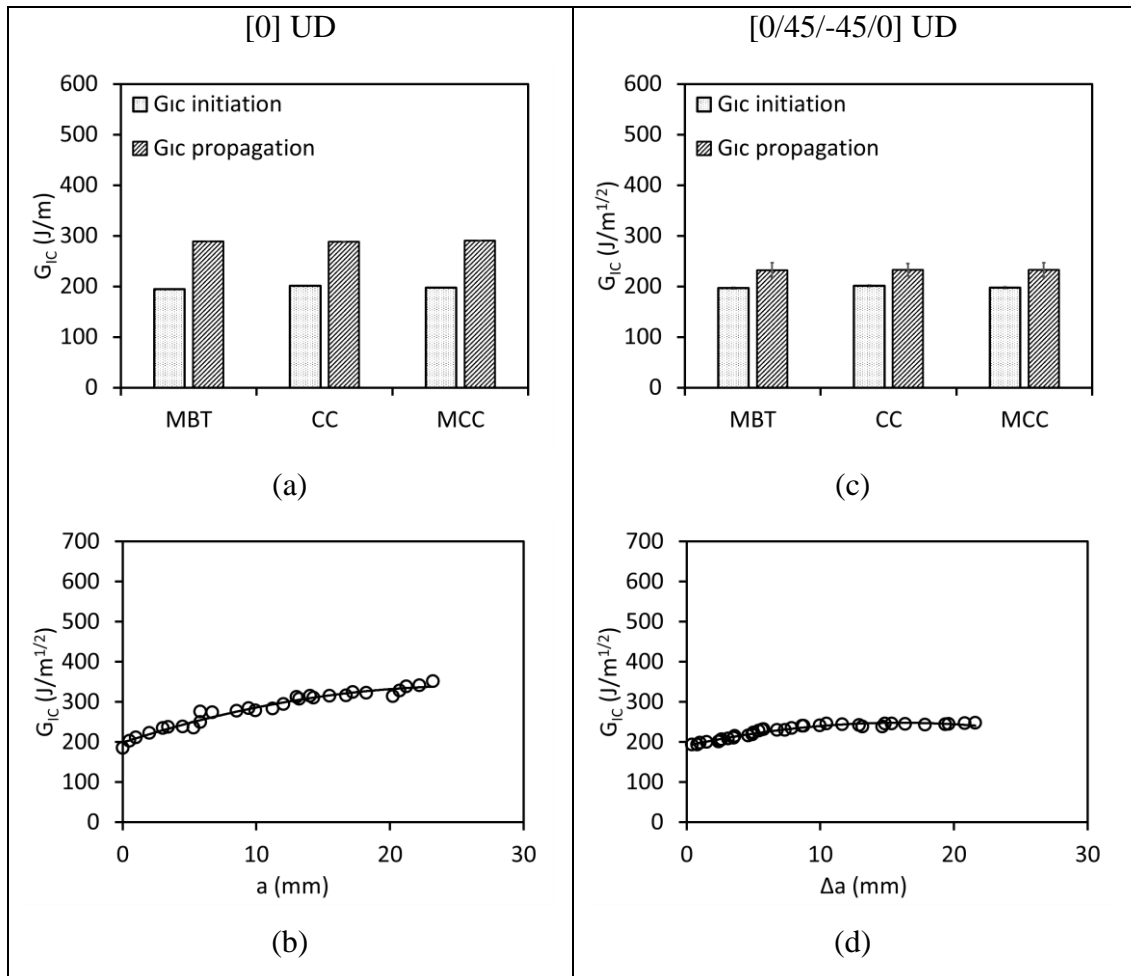


Figure 63 Bar graph of Mode-I fracture toughness ( $G_{Ic}$ ) initiation and propagation values obtained by MBT, CC and MCC methods (a) for [0] UD and (c) for [0/45] UD laminates, corresponding resistance curves obtained by MBT (b) for [0] UD laminates and (d) for [0/45] UD laminates.

#### 4.2.2. Mode-II Fracture Toughness

ENF test load displacement curves of [0] UD laminate, [0/45] UD laminate and [0/45] are in Figure 74a and b, respectively. Only one load drop is observed for all type of specimens. ENF test load displacement curves of [0] UD and [0/45] UD laminates have very similar behavior. Maximum load and deflection prior to failure are very close, effect of ply orientation does not noticed from the load displacement curves. High deviation in the stiffness of the curves are observed for the [0] UD and [0/45] UD laminates. For [0] UD laminate Maximum load remains around 750N, only maximum deflection at failure varies. For the [0/45] UD laminates variation of

both maximum load and deflection values prior to failure are seen as illustrated in Figure 74b. Maximum load of the [0/45] UD laminates changes from 650N to 750N.

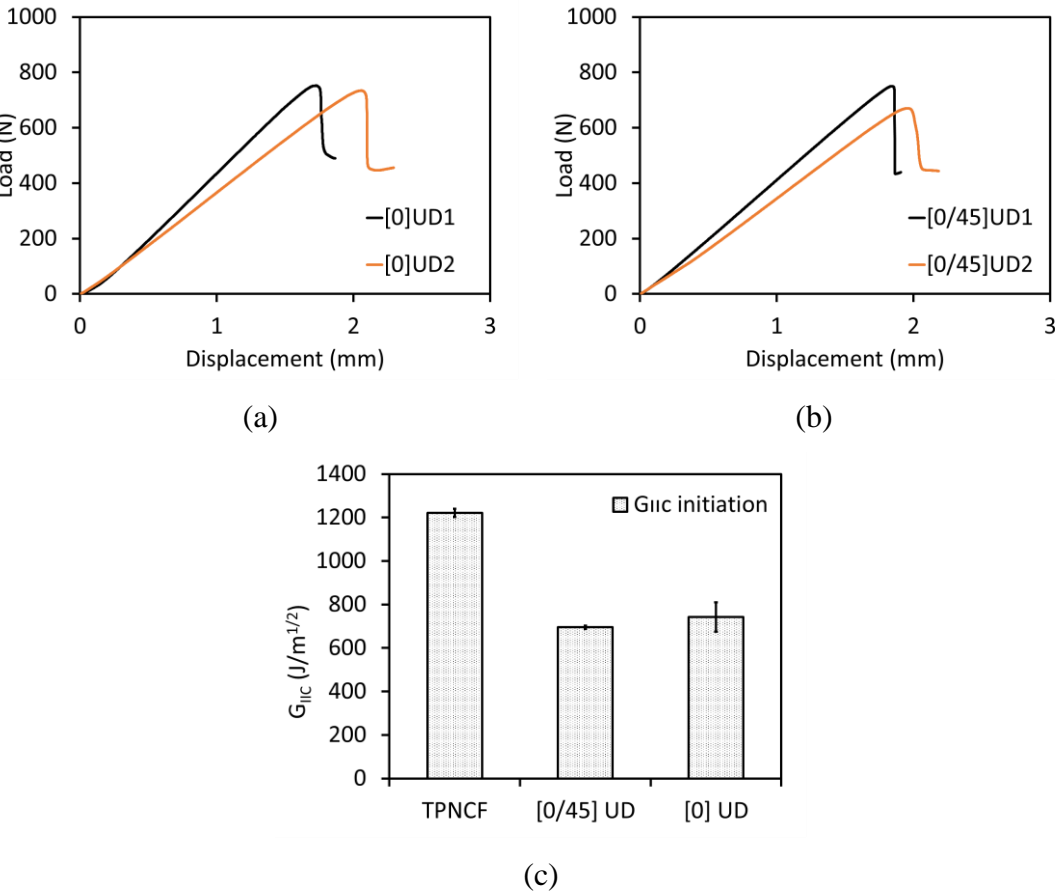


Figure 64 ENF test load displacement curves of (a) [0] UD laminates, (b) [0/45] UD laminates and (c) bar graph of Mode-II fracture toughness values for [0] UD and [0/45] UD laminates calculated by direct beam theory.

Bar graph of Mode-II fracture toughness values for [0] UD and [0/45] UD laminates calculated by direct beam theory is presented in Figure 74c. For the [0] UD laminates Mode-II fracture toughness ( $G_{IIc}$ ) value is found to be 742  $J/m^{1/2}$  and for the [0/45] UD laminates  $G_{IIc}$  value is around 695  $J/m^{1/2}$  which is about 7% less than [0] UD  $G_{IIc}$  value.

**4.2.3. Curved beam strength**

[0]<sub>28</sub> unidirectional laminates were manufactured with the first tool described in chapter 2 and manufacturing quality was not adequate. Four point bending test were conducted with these specimens in order to see the manufacturing effects on the curved beam strength and the failure of the curved parts. In order to see the details,

specimens are polished and no paint were applied to the surfaces. Failure was recorded by high speed camera system.

Load displacement response of [0] UD material have very unusual behavior as shown in Figure 65. There is no significant load drop. Only small load drops was observed during the test. Load continuously increases with these small drops. First load drop occurred at 400 N with 2 mm deflection. This behavior is directly related to the specimen manufacturing quality. Since specimen has initial defects, at every load drop either these initial defects propagated or crack growth occurred in the width direction as shown in Figure 65.

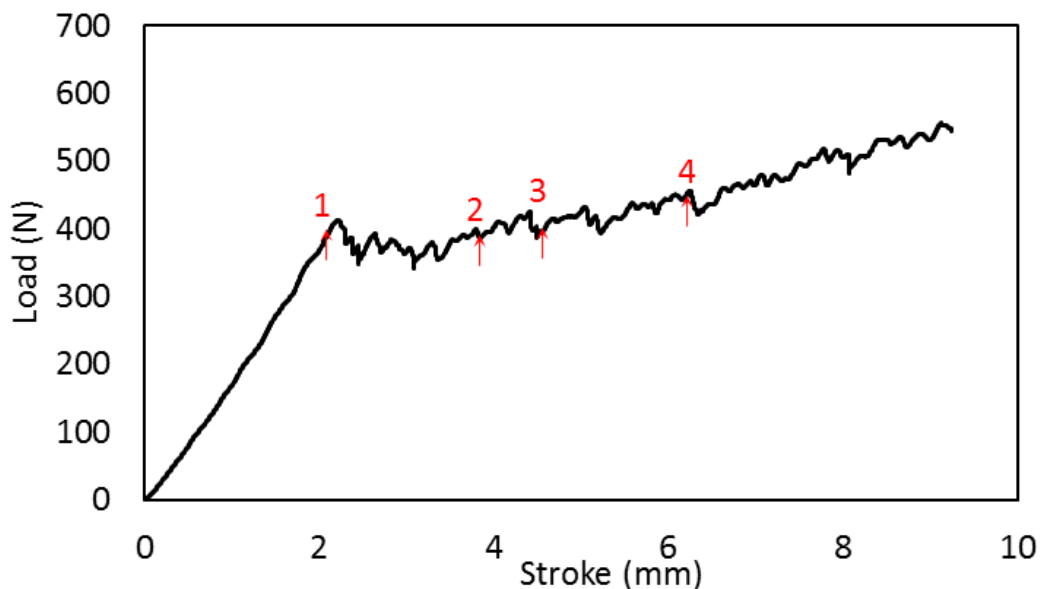


Figure 65 4-point bending test load displacement curves of [0] UD laminates.

High speed camera photos were taken at every load drop at the random trigger mode. In the Random trigger mode photos are taken one by one at any time. At every load drop and every cracking sound photos were recorded. High speed camera photos shows the failure sequence of [0] UD material in the Figure 66. And corresponding load values are marked in the load displacement curve (Figure 65). Initial defects are clearly seen in the first picture. In the second picture cracks propagated from the initial defects and new cracks are observed. It should be noted that although load drop occurred, in some photos no crack propagation or new cracks were observed. This observation is attributed to the idea that cracks might be propagated in the width

direction. Moreover, increase in the total load with small drops indicates that the cracks are not extend all through the width. In the last photo taken at 450 N with 6 mm deflection, the specimen looks like totally lost its load carrying capacity due to the multiple delaminations, specimen kept carrying load up to 550 N, after this point test was stopped. This observation also supports the idea that; propagated cracks seen in the pictures are not elongates through the entire width and at every propagation in both planes small loads drops were observed.

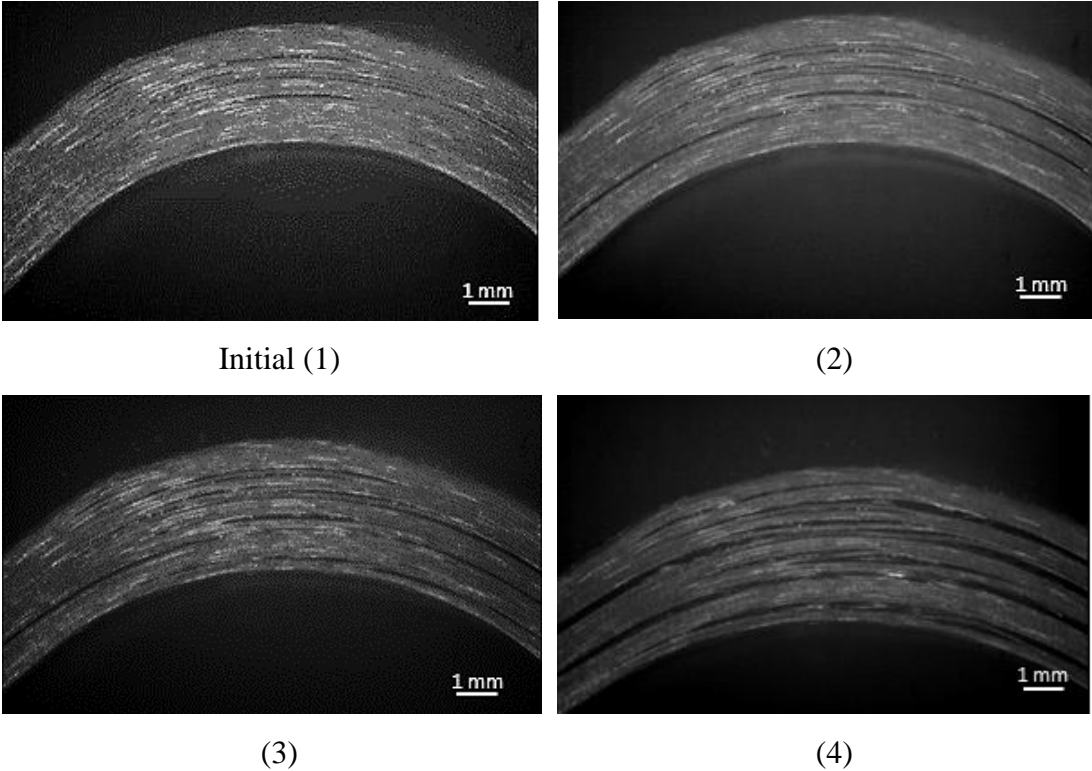


Figure 66 [0] UD specimen HSC photos corresponding to each load drop marked on the load displacement curve.

Two batches of [0/45]<sub>28</sub> unidirectional laminates were manufactured with the both of the tools described in chapter 2. Several initial defects in different locations were observed for all of the specimens. In order to see the details, specimens are polished and no paint were applied to the surfaces same as the [0] UD specimens for the first batch. Failure was recorded by high speed camera system.

Figure 67 represents 4-point bending load displacement curves of the [0/45] unidirectional laminates. In the four point bending load displacement curve of [0/45] UD specimens multiple load drops were observed. In third test failure occurs at much

lower load of 350 N in contrast to failure load of 700 N of 2nd specimen, however the specimen is still intact as seen by the same stiffness value as 1<sup>st</sup> and 2<sup>nd</sup> specimen. This might be due to failure occurring due crack tips increasing the stress concentration leading to earlier failure. In the third specimen only one initial defect was observed near the mid part, however the initial length of the crack is much smaller compared to second specimen (Figure 68). Two load drops occurred at the first and second test. For all of the tests after the load drop specimens can still carry load with the same slope before the drop for a while and then some nonlinearities appear.

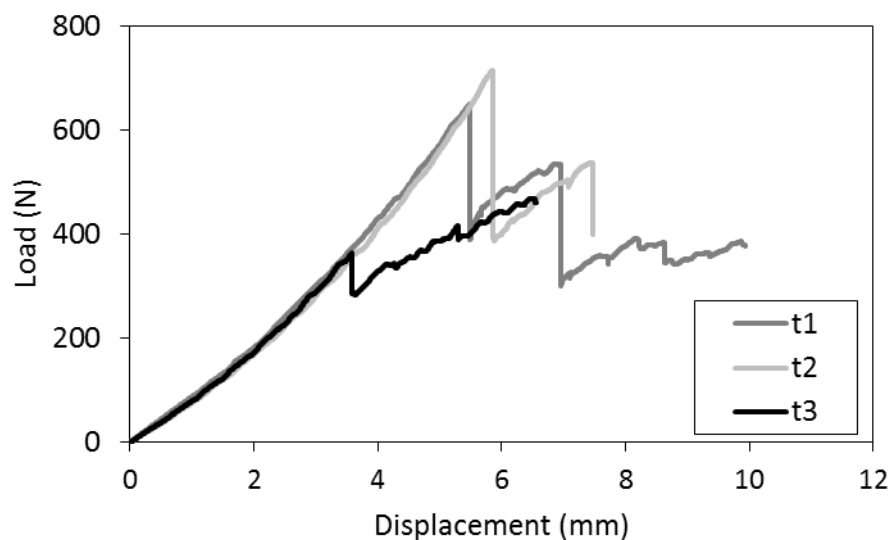


Figure 67 4-point bending test load displacement curves of [0/45] UD laminates.

Figure 68a and b presents the front and back side of the 2<sup>nd</sup> and 3<sup>rd</sup> specimens before and after test, respectively. At the front side a lot of small defects originated during manufacturing are seen while only one initial defect is observed at the middle part from the back view of the 2<sup>nd</sup> specimen. For the 3<sup>rd</sup> specimen when front and back sides are compared before and after the test, three small defects are observed only at the front side and at the back side there are only two small defects are seen at the middle part of the curved region before test. This indicates that the initial defects do not extend throughout the width of the specimen. When front and back side photos taken after the test are compared different delamination locations are observed for both specimens. For the 1<sup>st</sup> specimen it is clearly seen that at the front side three different delamination propagated from the initial defects and at the back side only

one delamination propagated from the initial defect at the middle of the specimen. Final pictures shows multiple delamination at different locations for the 3<sup>rd</sup> specimen. From pictures of the specimens after the test, it can be concluded that the initial defects originated during manufacturing process are the potential delamination nucleation points even though they do not extend throughout the width direction.

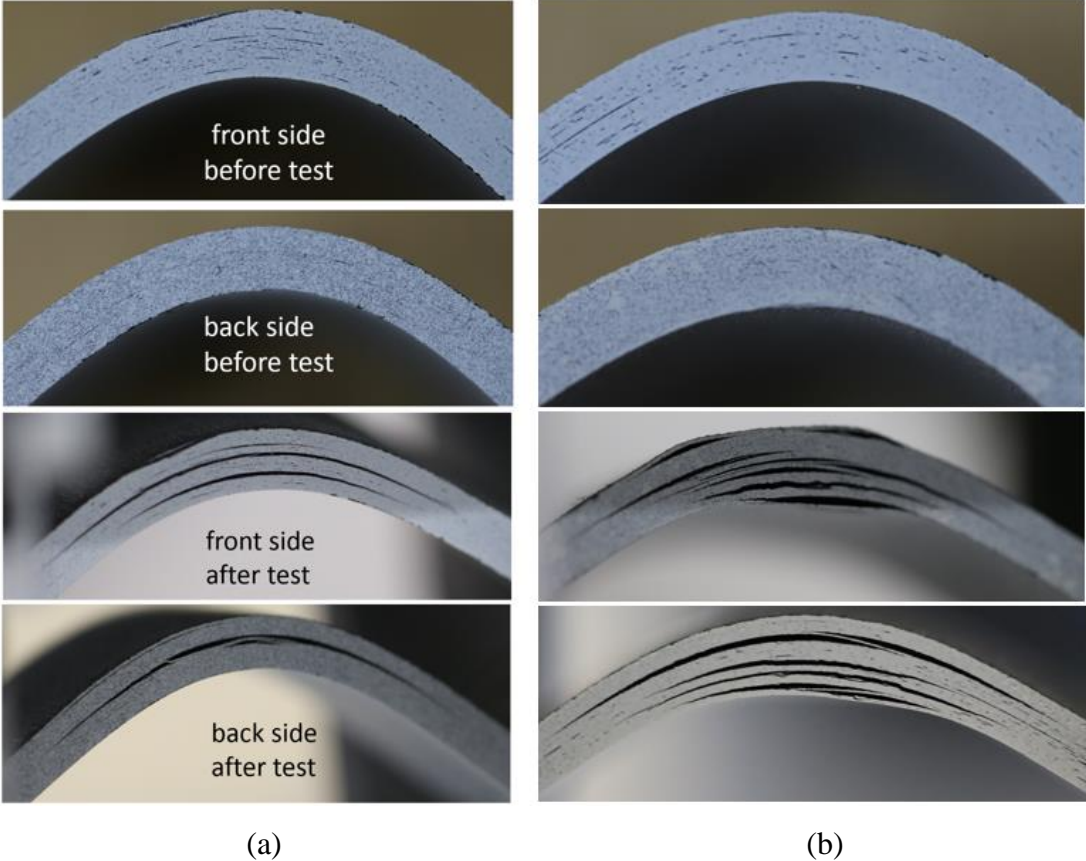


Figure 68 Front and back side photos of (a) 2<sup>nd</sup> and (b) 3<sup>rd</sup> specimen before and after test.

In the Figure 69a and b load displacement curve of test 1 and corresponding high speed camera photos taken at 35,000 fps are given, respectively. In the Figure 69 b the first picture shows initial state of the specimen 1 and white arrows indicate locations of initial defects. At the second picture specimen photo after first load drop is presented. Two delaminations were observed first one is at the mid part of the specimen and second delamination is located at four plies below the first delamination. It is seen that the second delamination propagates from the initial

defect. Third and fourth pictures represent the specimen photos after the second and third load drops, respectively.

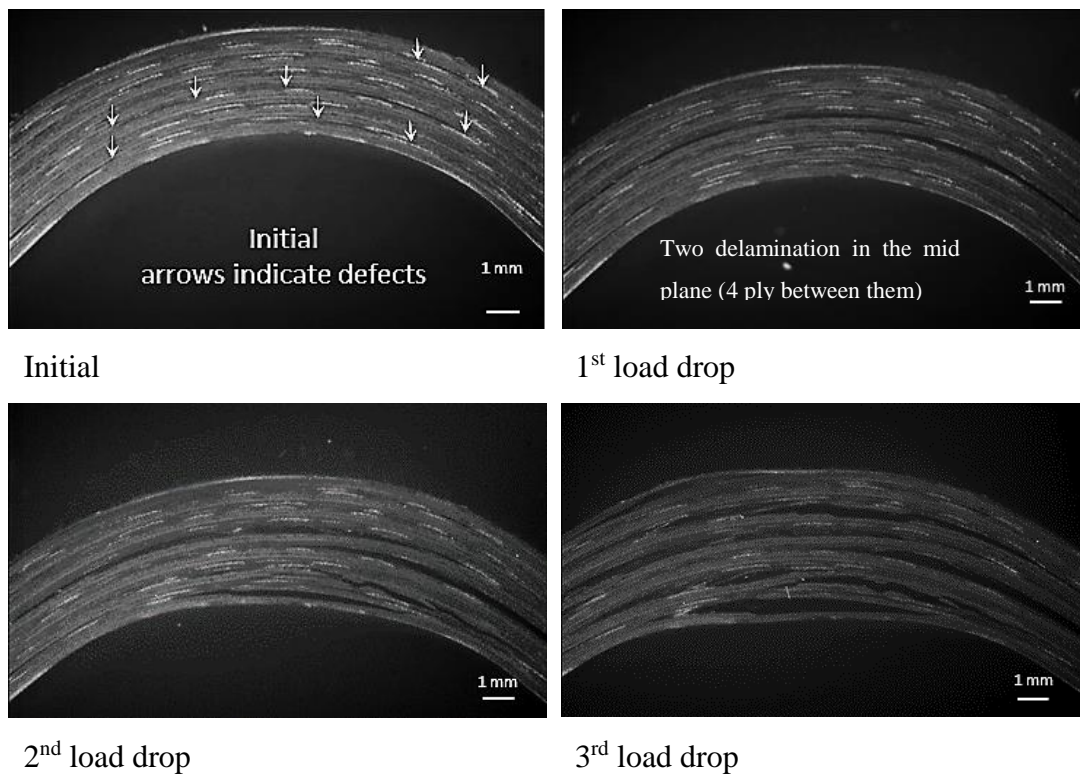
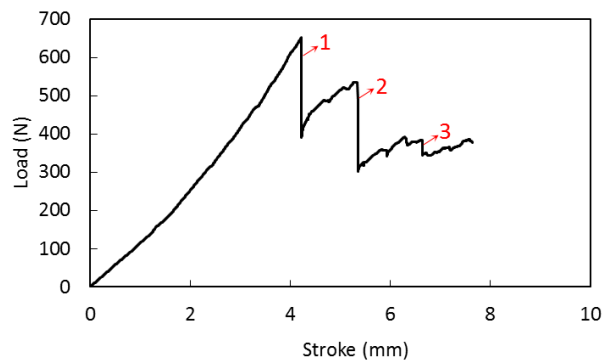
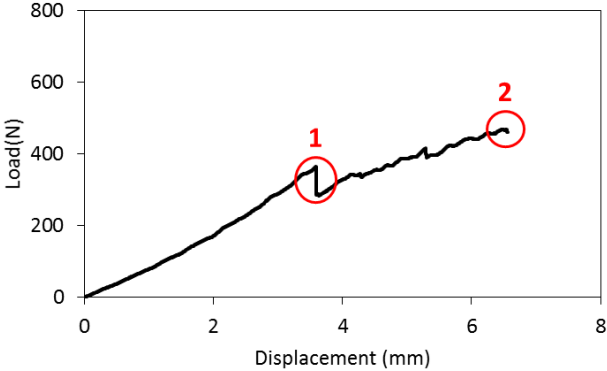


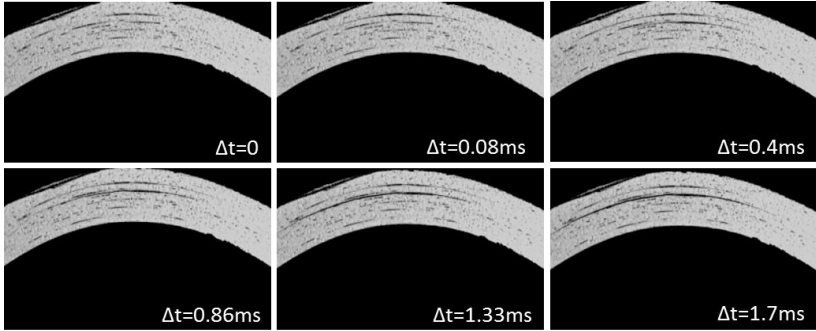
Figure 69 [0/45] UD specimen HSC photos taken at 35000 fps corresponding to each load drop marked on the load displacement curve.

Load displacement curve of test2 and high speed camera photos taken at 100,000 fps corresponding to each load drop are given in Figure 70a, b and c, respectively. First load drop occurs at 370 N and first picture in Figure 70b denotes the specimen prior to failure. Two delamination nucleates from the initial defects close to the upper radius and middle part. At the second load drop third delamination nucleates from

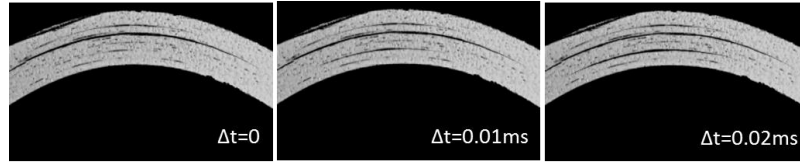
the initial defect below middle part close to inner radius. Whole process ends in 1.7ms and 0.02ms which are very stable compared to other type of laminates (Figure 66 and Figure 69). Load displacement curve of test 3 and high speed camera photos taken at 100,000 fps corresponding to each load drop are given in Figure 71a, b, c and d, respectively. 1st load drop corresponds to the extension of the initial defect that appeared during manufacturing to a delamination through the curved region. At the second region marked on the load displacement curve small delamination occurs at the left half of the specimen one ply above the first delamination. After a while as load increases at the third region on the load displacement curve small crack propagates at the left part of the specimen between first and second plies close to the outer radius. Small load drop occurs at the fourth region due to delamination propagation between last two plies close to the inner radius. At the 2nd load drop two delamination occurs in 960  $\mu$ s. crack kinking clearly seen in first crack. Last delamination occurs close to middle part just one ply below the first delamination.



(a)

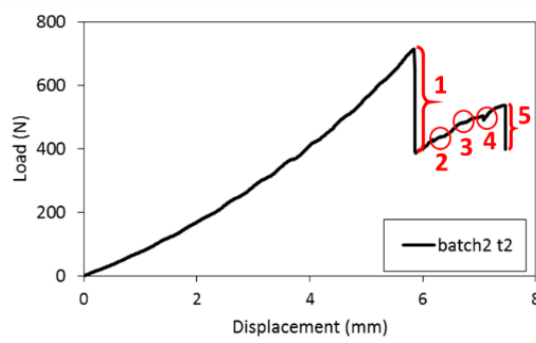


(b)

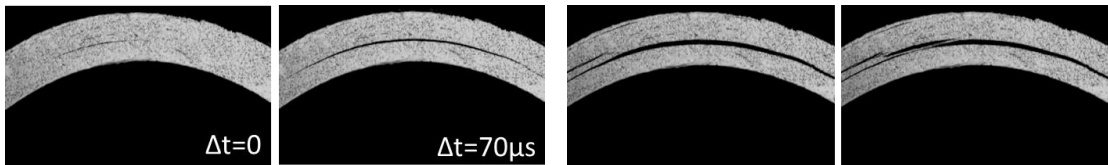


(c)

Figure 70 (a) 4-pt bending test load displacement curve of test1 indicating 1<sup>st</sup> and 2<sup>nd</sup> load drops, (b) and (c) corresponding HSC photos taken at 100,000 fps .

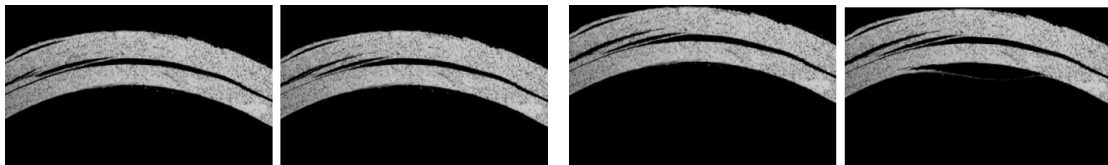


(a)



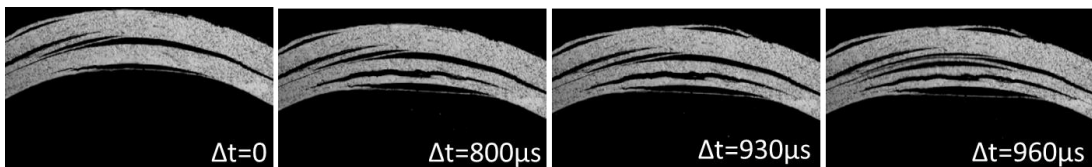
(b)

(c)



(d)

(e)



(f)

Figure 71 (a) 4-pt bending test load displacement curve of batch2 test2 [0/-45/45/0]7T UD and HSC photos corresponding to (b)1st load drop (1), (c) region 2, (d) region 3 e, (e) region 4 corresponding to small load drop, (f) 2nd load drop (5).

### 4.3. [0/45/-45/0] Thin Ply NCF

#### 4.3.1. Mode-I Fracture Toughness

Load displacement behavior of NCF material is different from the [0] UD and [0/45] UD laminates (Figure 62a and b) as shown in Figure 72. Slope of the curves are same for all three tests. At the initiation no significant load drop was observed. As crack continued to propagate rarely high load drops were seen. Load displacement curve response resembles fabric type material behavior (Figure 33). Maximum load at initiation reaches 55 N and maximum load value goes up to 68 N. For the TPNCF1 specimen load value remains nearly level while for TPNCF2 and TPNCF3 specimen load value slightly decreases as crack propagates.

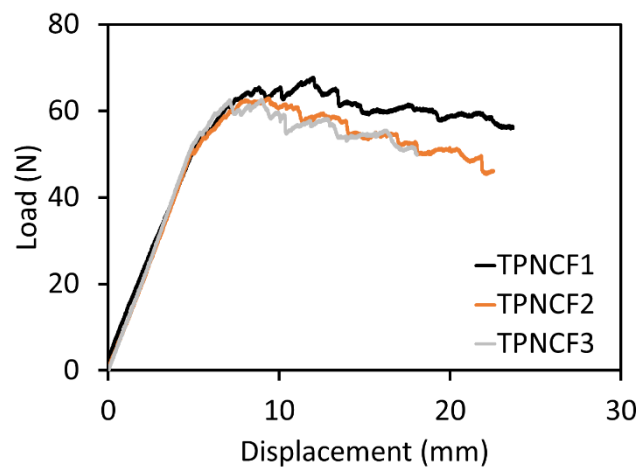


Figure 72 DCB load displacement curves of three tests for [0/45] thin ply NCF laminates.

Bar graph of Mode-I fracture toughness ( $G_{IC}$ ) initiation and propagation values obtained by MBT, CC and MCC methods for thin ply NCF laminates are given in Figure 73a. In the Corresponding R-curve shown in Figure 73 smooth distribution is observed. Initiation value is close to  $300 \text{ J/m}^2$  and propagation values goes up to  $680 \text{ J/m}^2$ .

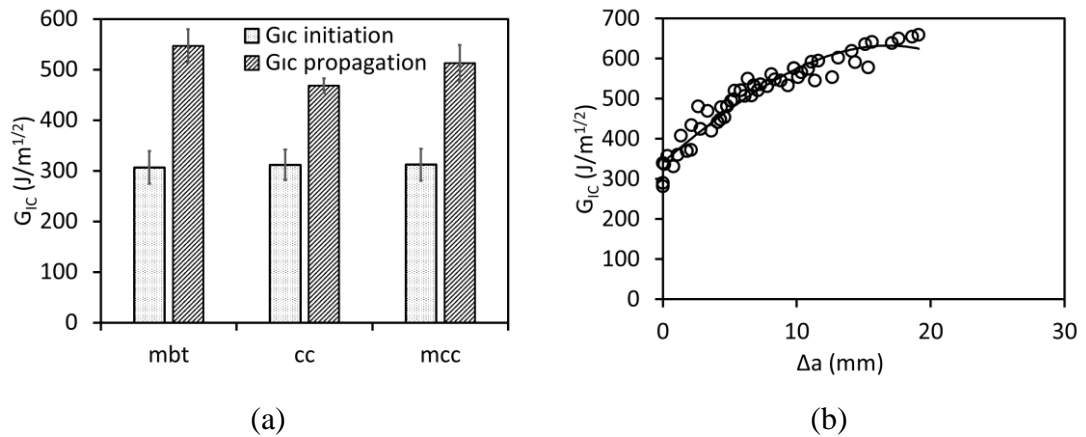


Figure 73 Bar graph of Mode-I fracture toughness ( $G_{Ic}$ ) initiation and propagation values obtained by MBT, CC and MCC methods for thin ply NCF laminates, (b) corresponding resistance curves obtained by MBT.

### 4.3.2. Mode-II Fracture Toughness

ENF test load displacement curves of thin ply NCF laminates are shown in Figure 74. Only one load drop is observed for both tests. For the thin ply NCF laminates stiffness of the curves, maximum load prior to failure are exactly same in two of the tests. NCF laminates can resist up to 965N. Bar graph of Mode-II fracture toughness values for TPNCFL laminates calculated by direct beam theory is presented in Figure 74b. Mode II fracture toughness value of thin ply NCF is found to be  $1220 J/m^{1/2}$ . Thin ply NCF type material configuration 75% and 64% of increase Mode-II fracture toughness value compared to [0] and [0/45/-45/0] UD laminates, respectively.

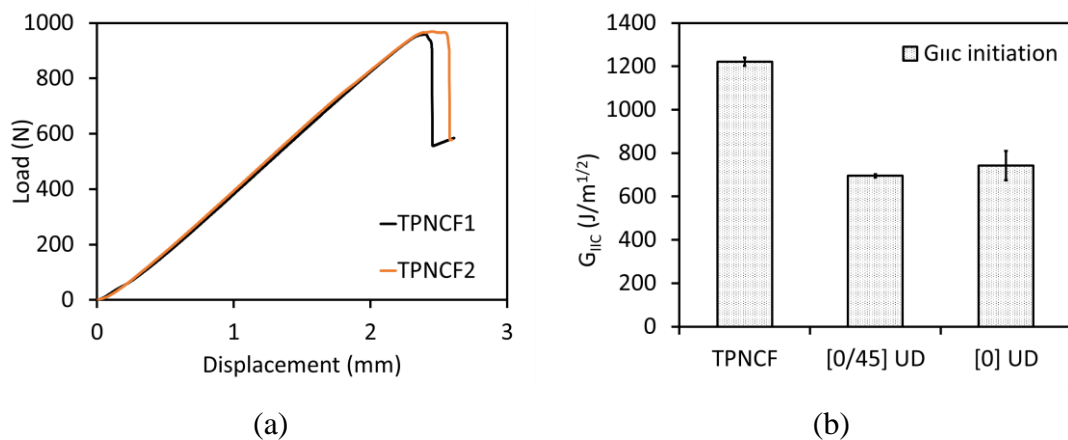


Figure 74 (a) ENF test load displacement curves of thin ply NCF laminates and (b) bar graph of Mode-II fracture toughness values for TPNCFL calculated by DBT.

### 4.3.3. Curved Beam Strength

Figure 75 represents 4-point bending load displacement curves of the [0/45] thin fiber NCF laminates with 3 mm thickness. No stiffness change is observed between 3 different specimens, only maximum load varies from 1700 N to 2100 N. Only one load drop occurs for all specimens and load decreases to nearly 500N, except the test1. Although specimens still can carry load with slightly lower stiffness, tests were stopped after 1000 N since no more delamination propagation occurred and failure is expected at the leg. In the first test first load drop occurred at 1200 N which is lower than the other three tests and stiffness is lightly lower. Specimen was loaded again after first load drop, and small load drop occurred at 800N. Third load drop occurred at 1600N at 16mm deflection.

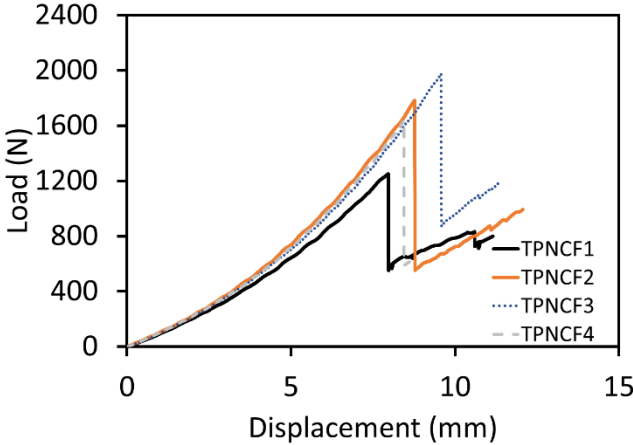


Figure 75 4-pt bending test load displacement curves of [0/-45/45/0]12T thin ply NCF 1st and 2nd batch together.

Figure 76a and b represents the front and back side of thin fiber NCF specimens before and after test, respectively. Only for the 3<sup>rd</sup> specimen small defects both at front and back side are observed and also Very small voids are observed for all specimens. Failure path seems similar for all three specimens. Two delamination propagated to the both arms are observed at the curved region. Locations of the cracks slightly change for the 1<sup>st</sup> specimen it is at the middle, for the 2<sup>nd</sup> specimen it is just below the middle and for the 3<sup>rd</sup> specimen just above the mid part.

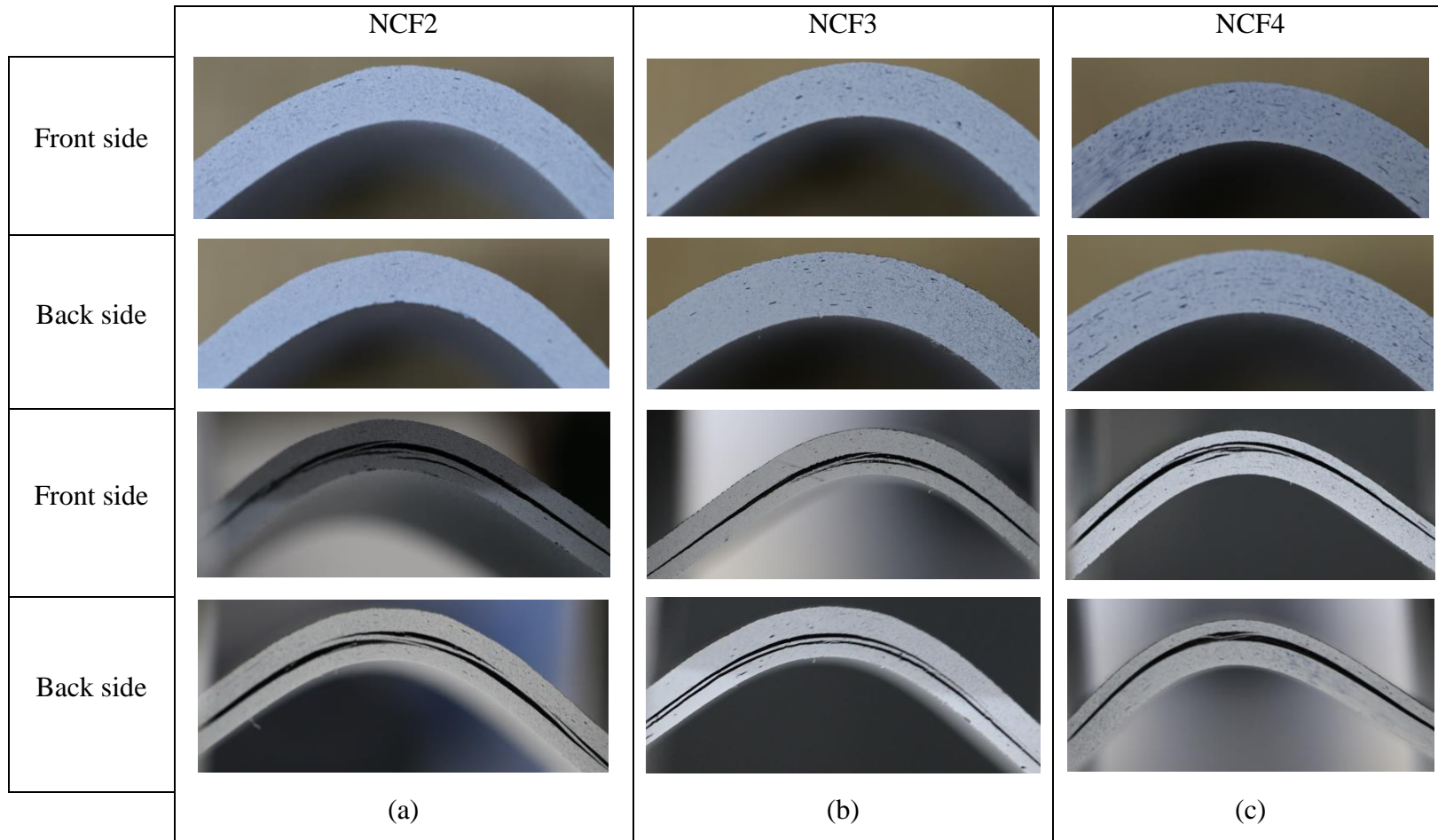


Figure 76 Front and back side photos of (a) 1<sup>st</sup> and (b) 3<sup>rd</sup> specimen before and after test

High speed camera photos of crack propagation taken at 42000 fps in test1 is given in the Figure 77. In the first photo two simultaneous delamination propagation at the mid plane can be seen. Finally, a third delamination propagates near to the inner radius at the right half of the specimen. Then it grows to the right arm.

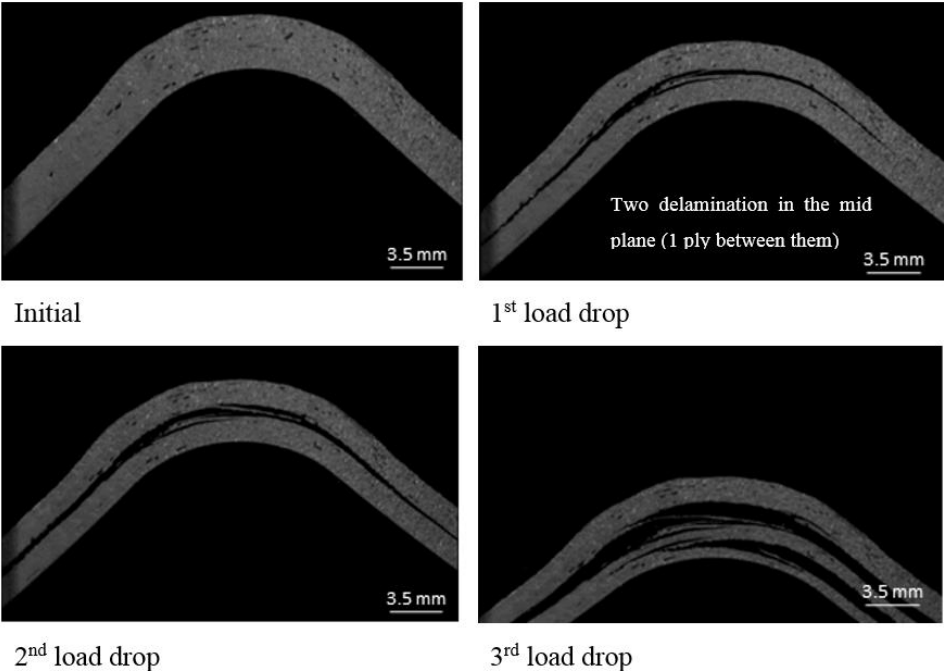


Figure 77 TPNCF1 specimen HSC photos taken at 42500 fps.

Figure 78 shows the failure sequence of thin fiber NCF laminates in one load drop captured by high speed cameras at 100,000fps and 300,000fps, respectively. In Figure 78 whole process takes 70  $\mu$ s which is highly unstable. First picture shows initial state. Three delaminations propagates simultaneously at the curved region two of them is at the same ply and third is one ply below them, fourth small delamination occurs between middle and inner radius at the right half of the curved region in first 10  $\mu$ s. in next 10  $\mu$ s first two delamination merges and new delamination growth is seen from the left side above the mid part and For the next 50  $\mu$ s it propagates to the curved part.

Figure 79 high speed photos shows the failure sequence of thin fiber NCF laminates at 300,000 fps. First four photos describes the first 10  $\mu$ s in detail. Two delamination initiates at the curved part in 3.5  $\mu$ s first crack is at the middle and second crack is at the left part of the curved region. There is only one ply between these two cracks. In next 3.5  $\mu$ s third crack initiates below the initial cracks and first two delaminations

propagates to the arms. At 36  $\mu\text{s}$  initial delamination at the left part starts to propagate to the left side of the curved region for the next 20  $\mu\text{s}$ , however it extends to just end of the curved part, does not grow to the left arm. Whole process ends up in 50  $\mu\text{s}$ .

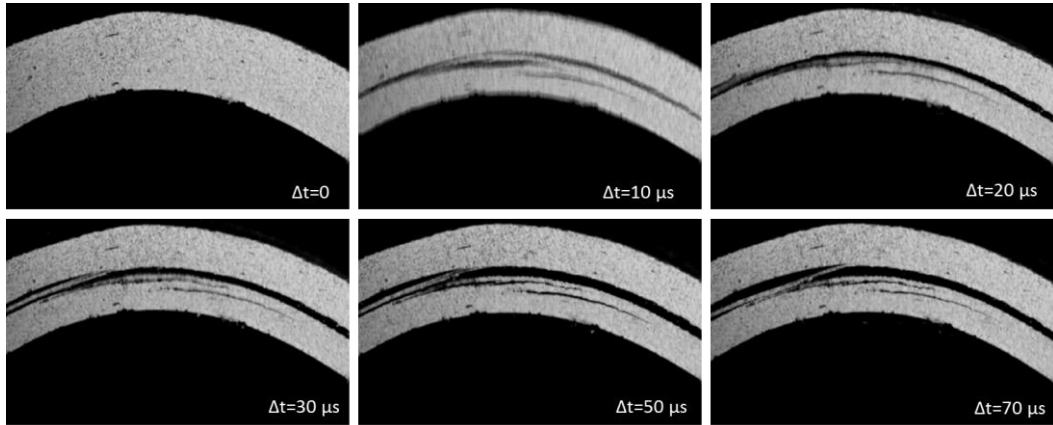


Figure 78 High speed photos of TPNCF2 specimen 2<sup>nd</sup> test (2<sup>nd</sup> batch), taken at 100,000 fps showing the failure sequence.

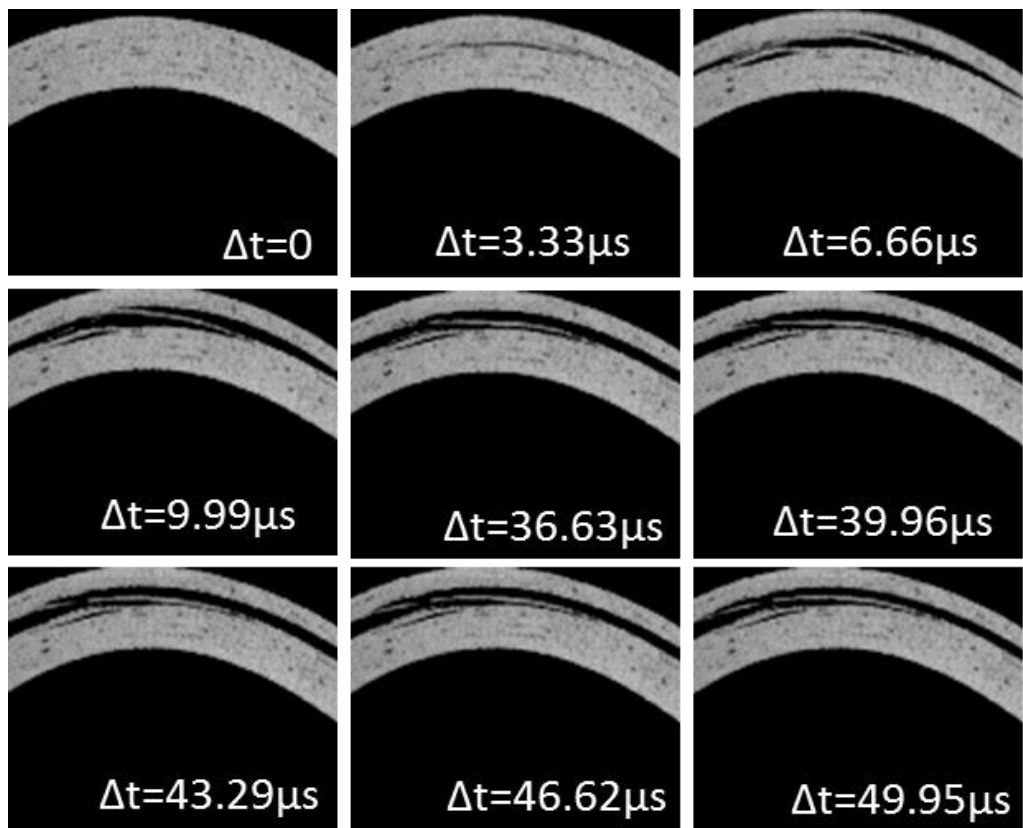


Figure 79 High speed photos of TPNCF3 specimen 3<sup>rd</sup> test (2<sup>nd</sup> batch), taken at 300,000 fps showing the failure sequence.

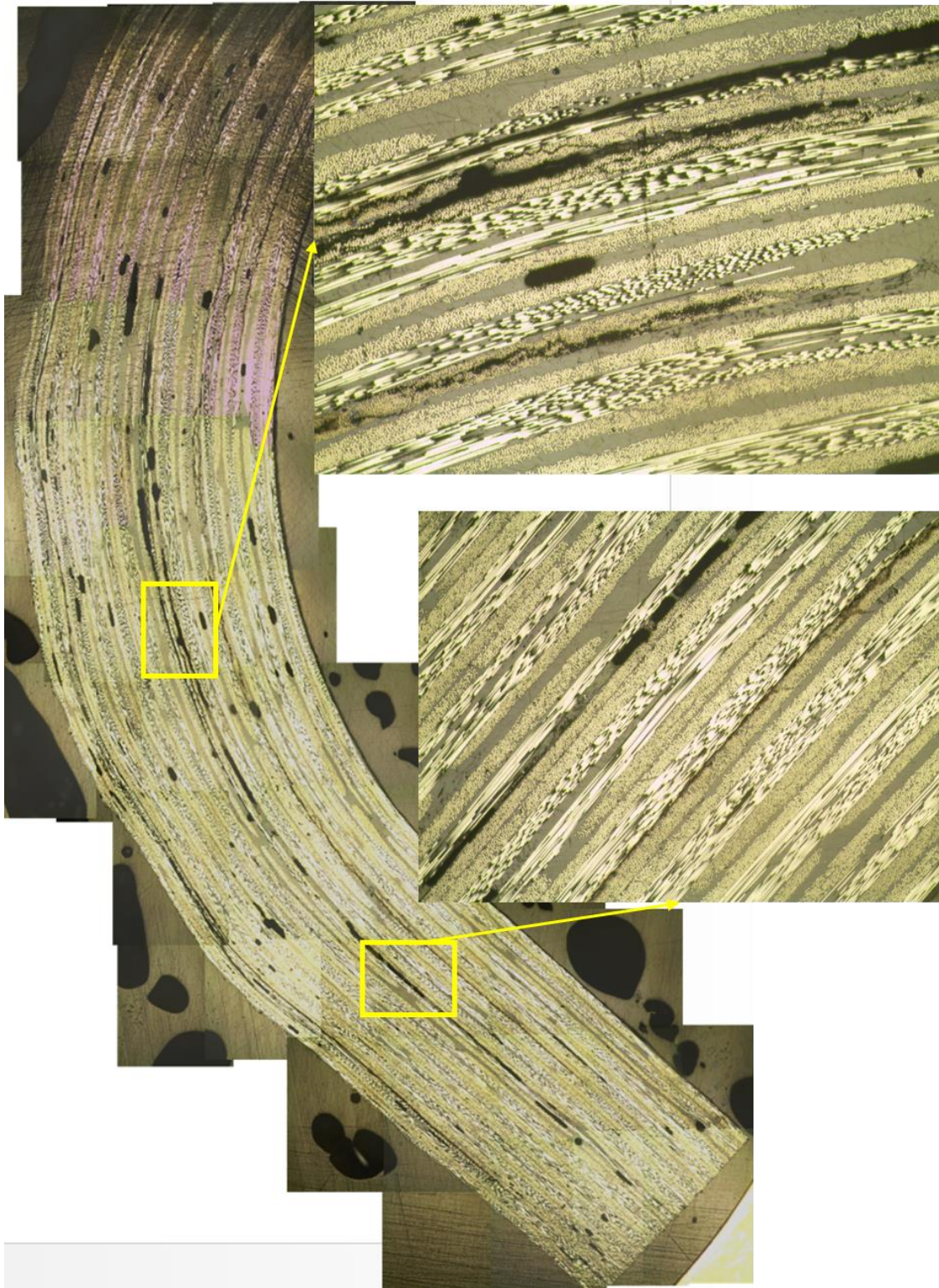


Figure 80 Micrograph of curved region of TPNCF1 specimen after 4-pt bending test.

## 4.4. Results and discussions

### 4.4.1. Fracture Toughness Results

Load displacement curves of three materials, obtained in the DCB tests, shows that both [0] UD and [0/45] NCF materials stiffer than the [0/45] UD material as shown in Figure 81a. Moreover, the weakest material is [0/45] UD. Crack propagation begins at 35 N for [0/45] UD material, while at 45 N initiation starts for [0] UD and at 55 N initiation starts for [0/45] NCF material. Load displacement behaviors of [0/45] and [0] material are similar. The main difference is that as load stays level for [0], load decreases slightly as crack propagates for the [0/45] material. Load displacement behavior of [0/45] NCF has different trend than the other two material. Load drops at the initiation is more stable, load increases up to 65 N, after 15 mm crack propagation sudden load drops are observed.

ENF test load displacement curves of [0] UD laminate, [0/45] UD laminate and thin ply NCF laminate are shown in Figure 81b. ENF test load displacement curves of [0] UD and [0/45] UD laminates have very similar behavior, effect of ply orientation does not noticed from the load displacement curves. High deviation in the stiffness of the curves are observed for the [0] UD and [0/45] UD laminates. For [0] UD laminate. For the [0/45] UD laminates variation of both maximum load and deflection values prior to failure are seen as illustrated in Figure 81b. for the thin ply NCF laminates stiffness of the curves, maximum load prior to failure are exactly same in two of the tests. NCF laminates can resist up to 965N.

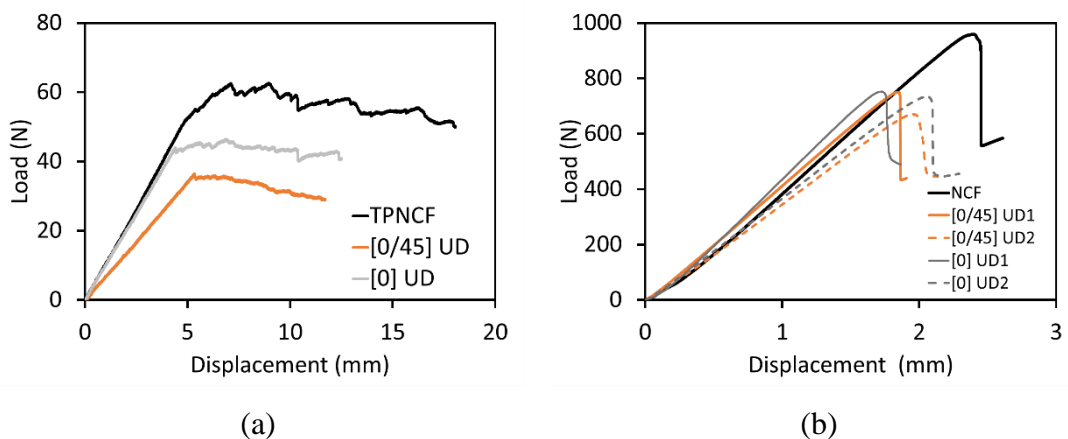


Figure 81 Load displacement curves of NCF, [0/45] UD and [0] UD laminates obtained (a) DCB tests and (b) ENF tests.

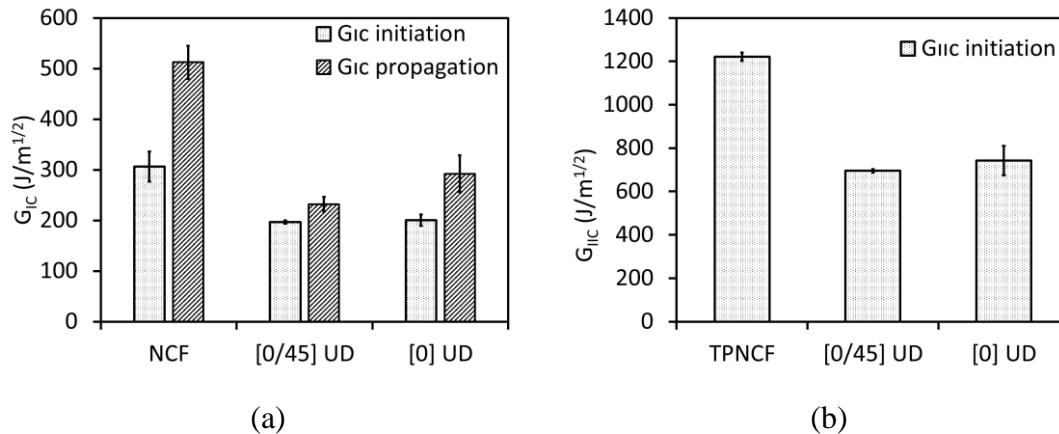


Figure 82 (a) Bar graph of Mode-I fracture toughness ( $G_{IC}$ ) initiation and propagation values obtained by MBT and (b) bar graph of Mode-II fracture toughness values calculated by direct beam theory for TPNCF, [0] UD and [0/45] UD laminates.

#### 4.4.2. Curved Beam Strength Results

Load displacement curves obtained from 4-point bending tests are presented in Figure 83 for all three type of material. [0] UD laminate very unusual behavior for a 4-point bending test. Stable load drops occur continuously indicating that the specimen has no overall stiffness to carry load. At every load drop cracks propagate in the either thickness direction or in the width direction. [0/45] UD laminates can resist up to 700N and two load drops occur. After the first load drop specimen can still carry load without changing the slope, which indicates that cracks do not extend all through the width of the specimen and specimen does not loss its load carrying capacity completely. High speed camera photos of the specimen before, during and after the test shows that the initial defects are the potential crack nucleation points and delamination initiation and propagation locations are different at back and front side of a specimen which is coherent with the observations of load displacement behavior as shown in Figure 84a and b. [0]UD1and [0/45]UD1 specimens have different failure surfaces at the front and back sides. Thin ply non-crimp fabric laminate load displacement behavior is different from UD laminates. Specimens can carry load up to 1800N and one load drop occurs. After the load drop load carry in capacity decreases to 500N, indicating that the failure occurs throughout the width direction and specimen loses its stiffness. In Figure 84c specimen photos before test

and after test are presented. Small voids are observed, however their presence is not fatal for the specimen, and neither load displacement curve nor failure pattern is affected. For all of the three of the tests two major delamination observed at the mid part from the front view and crack locations slightly change at the back side of the specimens.

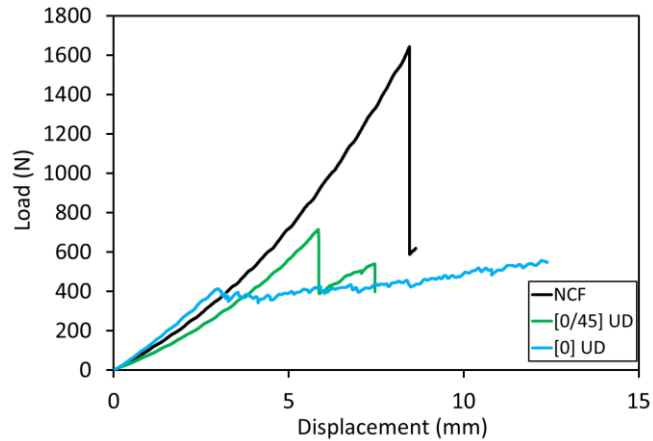


Figure 83 Four point bending load displacement curves of [0] UD, [0/45] UD and [0/45] thin fiber NCF laminates all together.

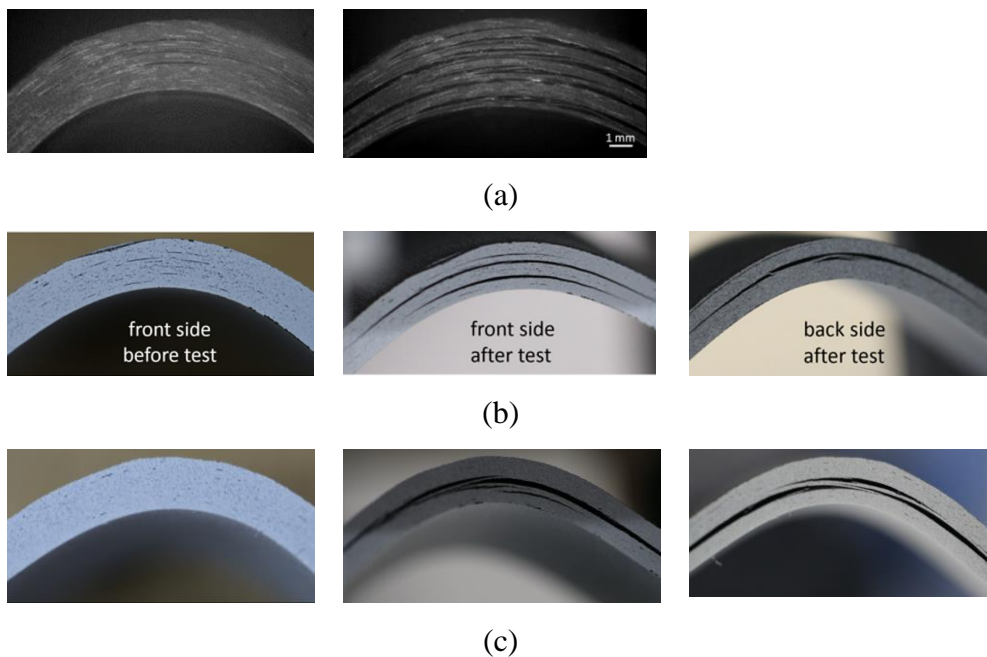


Figure 84 Specimen photos taken before and after test showing the front and back sides of (a) [0]UD specimens, (b) [0/45/-45/0]UD specimens and (c) thin ply NCF specimens.



## CHAPTER 5

### SUMMARY AND CONCLUSIONS

#### 5.1. Summary

In this thesis resistance against delamination failure and through the thickness tensile properties of curved carbon fiber reinforced plastics composites are investigated experimentally by conducting Mode-I and Mode-II fracture toughness tests and the curved beam strength tests. Effect of enhancements to the brittle matrix is investigated by comparing CNT added fabric type composite laminates with similar fabric composite laminates and effect of novel material thin ply non crimp fabric laminates on delamination resistance of carbon fiber reinforced plastics composites are investigated and presented in separate chapters. General information about the delamination problem and description of novel material are given in the introduction chapter. In order to determine the Mode-I, mode-II and through the thickness tensile properties of curved carbon fiber reinforced plastics composites, standard test methods are carried out, namely DCB, ENF and 4-point bending tests. The dynamic delamination propagation and failure sequences under bending is captured using Photron© Fastcam SA5 ultra high speed system.

In the CNT studies, 25% and 10% percent higher values are obtained in the Mode-I and Mode-II fracture toughness for the CNT-fabric type material, respectively. Although CBS and maximum radial stresses are found to be 50% and 64% less for the CNT-fabric material compared to prepreg-fabric material, plots multiple load drops are observed in the load displacement for the CNT-fabric materials. For both types of materials multiple delaminations are observed and the progress of delaminations are recorded. Higher scatter was seen in all tests for the CNT-fabric laminates compared to the prepreg-fabric laminates. This is attributed to the heterogeneity and local concentration of CNTs resulting in property variation between different specimens.

For the non-crimp fabric configuration compared with [0] and [0/45] UD laminates increase in the Mode-I and Mode-II fracture toughness and curved beam strength are obtained. It is observed that the initial defect originated due to manufacturing are the potential failure sides and directly affects the stiffness and the load carrying capacity of the material.

## **5.2. Conclusions**

*For the CNT added composite laminates:*

In comparison with prepreg-fabric material, Mode-I and Mode-II fracture toughness and stiffness is found to be higher for the CNT-fabric laminates, however, the failure load is found to be less in the 4-point bending tests for the CNT-fabric laminates compared to prepreg-fabric laminates. Prepreg-fabric laminates can stand up to 2700 N and failure occurs at one load drop. In contrast to prepreg-fabric laminates, two load drops are observed for the CNT-fabric laminates. At the first load drop initial delamination occurs close to the upper edge of the specimen and it continues carrying load up to the second load drop without changing slope. For the CNT-fabric laminates maximum load prior to failure is lower than the prepreg-fabric material, varying between 1500 and 1700 N. Scatter in the maximum load value of first and second load drop for the CNT added laminates is attributed to the non-uniform dispersion of CNTs during manufacturing leading to heterogeneous distribution and clumping of CNTs in the resin and property variation between different specimens.

However, decrease in the curved beam strength cannot be directly related to CNT effect in the resin since material properties of the two type of laminates are not exactly the same. As a second might be that hand layup manufacturing technique with dry fabrics might decrease the quality over the prepregs. In addition although thickness of the two type of laminate are very close, prepreg-fabric laminates consist of 12 plies while CNT added laminates consist of 8 plies. Even though these results cannot provide quantitative conclusions, however consistency in the two load drops behavior under moment loading and higher toughness values with smaller crack lengths for CNT added laminates provides qualitatively conclusions. In order to understand the effect of CNTs on the CBS of material, further investigations should be made with the same baseline material.

*Finally for CNT added composite laminates, it can be concluded that:*

- Higher fracture toughness values is attributed to observed CNT bridging of cracks in the resin.
- Total failure occurred in two load drops in contrast to one load drop for the prepreg-fabric material.
- Although the CBS and failure load is lower, the specimen becomes more resilient against failure – damage tolerance capacity increases.
- Higher scatter in CNT added laminates which can be attributed to heterogeneity and local concentration of CNTs resulting in property variation between different specimens.
- In order to understand the effect of CNTs on the CBS of material, further investigations should be made with the same baseline material.

*For the thin ply non-crimp fabric laminates:*

Non-crimp fabric configuration is found to increase the stiffness, maximum load and Mode-I, Mode-II fracture toughness of the material. Results of all of the three tests are very consistent for thin ply NCF laminates, while effect of ply orientation cannot be noticed from the load displacement curves of ENF test since curves have very similar behavior for [0] UD and [0/45] UD laminates. In addition Mode-I fracture toughness decreases with changing stacking sequence without changing the interface 0/0 configuration.

Effect of manufacturing quality on the strength of curved composite laminates is observed for [0] UD and [0/45] UD laminates. Initial defects are the potential crack nucleation points. For the [0] UD laminates stable load drops occurred during the test which can be concluded that the specimen has enough stiffness to carry load. [0/45] UD laminates can resist up to 700N and two load drops occurred, however cracks were nucleated where initial defects are seen. The argument that cracks do not extend all through the width of the specimen and specimen does not loss its load carrying capacity completely after the load drop is attributed to the different failure surfaces at the front and back sides.

For the thin ply non-crimp fabric laminates one load drop occurs and after the load drop specimen lose their stiffness load carrying capacity. Delamination occurs between 0/45 and 45/-45 plies inside the stitch meandering in 45<sup>0</sup> plies during propagation. In the with direction crack meandering is also seen clearly which results in slight difference at the front and back sides of the specimens.

*Finally for the thin ply non-crimp fabric laminates, it can be concluded that:*

- Changing the layup but keeping the delamination interface to be 0/0 interface decreases fracture toughness of the laminate.
- Non-crimp fabric configuration increases the both Mode-I and Mode-II fracture toughness values.
- Initial defects originating from the manufacturing directly affect the failure load, location and sequence. Although no effect was seen on the elastic part of the load displacement curve, these initial defects become the nucleation sources for delamination.
- Non-crimp fabric type material increases the curved beam strength since stitching provides extra strength and also thin fiber provides more homogeneity resulting in increased properties.
- Non-crimp fabric type material is found to be easy to process than the UD laminates under the same manufacturing steps, and more suitable for production of complex geometries.

### **5.3. Future Work**

In the future following items should be considered:

- Same manufacturing technique and same material for the prepreg-fabric and CNT added laminates should be carried out in order to isolate the effect of CNT addition.
- Basic property tests can be done by producing test specimens with CNT addition. Finite element analysis can be done to study micromechanics of CNT added laminates.

- Thin ply non-crimp fabric studies can be continued by increasing the manufacturing quality in order to have better understanding of the effect of non-crimp fabric configuration on the strength of laminates and finite element analysis can be done to understand the phenomena completely.



## REFERENCES

1. Kaw K.A., Mechanics of Composite Materials, CRC Press Taylor & Francis Group, Boca Raton/London/New York, 2006.
2. Daniel I.M., Isai O., Engineering mechanics of composite materials, Oxford University press, 1994.
3. Reddy J.N., mechanics of laminated composite plates and shells theory and analysis, CRC Press, Boca Raton/London/New York/Washington D.C., 2004.
4. Staab G.H, Laminar Composites, Butterworth-Heinemann, Boston/Oxford/Auckland/Johannesburg/Melbourne/New Delhi, 1999.
5. Niu MCY., Composite airframe structures, AD Adaso/Adastra Engineering LLC, 1989, ISBN 978-962-7128-11-3.
6. 787 Dreamliner Fact Sheet, Boeing Company (2009), Retrieved October 15, 2013 from <http://www.boeing.com/boeing/commercial/787family/programfacts.page> .
7. Niu MCY. Airframe Structural Design. 2nd Edition. Hong Kong Conmilit Press Ltd, 2002, ISBN 962-7128-09-0.
8. Sørensen BF, Jørgensen E, Debel CP, Jensen FM, Jensen HM, Jacobsen TK, Halling KM. Improved design of large wind turbine blade of fibre composites based on studies of scale effects (Phase 1) - Summary Report. Risø National Laboratory Denmark, 2004, Risø-R-1390(EN).
9. Vanttinen, A., Strength prediction of composite rib foot corner, Helsinki University of Technology, 2008.
10. Edwards T., Thompson J., "Spar Corner Radius Integrity for the A400M Wing," Applied Mechanics and Materials, Vols. 3-4, pp. 197-204, 2005.
11. O'Brien T K. Composite Interlaminar Shear Fracture Toughness, GIIC: Shear Measurement of Sheer Myth?. ASTM-STP 1330, American Society for Testing and Materials, 1998:3-18.
12. Lekhnitskii SG. Theory of elasticity of an anisotropic body. Mir Publishers. Moscow. 1981. Print.
13. ASTM Standard D6415/D6415M, 2006. Standard test method for measuring the curved beam strength of a fiber-reinforced polymer-matrix composite. ASTM

- International, West Conshohocken PA, 2006, DOI: 10.1520/D6415\_D6415M, www.astm.org.
14. Sridharan, S., Delamination behavior of composites, CRC Press LLC, 2008.
  15. ASTM Standard D5528, 2007. Standard Test Method for Mode I Interlaminar Fracture Toughness of Unidirectional Fiber-Reinforced Polymer Matrix Composites. ASTM International, West Conshohocken PA, 2007, DOI: 10.1520/D5528\_D5528M, www.astm.org.
  16. ASTM Standard WK22949. New Test Method for Determination of the Mode II Interlaminar Fracture Toughness of Unidirectional Fiber-Reinforced Polymer Matrix Composites Using the End-Notched Flexure (ENF) Test. ASTM International, West Conshohocken PA, www.astm.org.
  17. New Cracks Found in the Wings of Some Airbus Planes, The New York Times, 20.01.2012. Retrieved February 22, 2012 from:  
[http://www.nytimes.com/2012/01/20/business/global/a380-jets-may-get-closer-inspections.html?\\_r=1&adxnnl=1&adxnnlx=1330264957-YWtr4fefgIvKExc6rrqAtA](http://www.nytimes.com/2012/01/20/business/global/a380-jets-may-get-closer-inspections.html?_r=1&adxnnl=1&adxnnlx=1330264957-YWtr4fefgIvKExc6rrqAtA)
  18. Hao W, Ge D, Ma Y, Yao X, Shi Y. Experimental Investigation on Deformation and Strength of Carbon/Epoxy Laminated Curved Beams, Polymer Testing 2012;31: 520–526.
  19. Sun CT and Kelly SR. Failure in Composite Angle Structures Part II: Onset of Delamination. Journal of Reinforced Plastics and Composites 1988 7:233-244.
  20. Rodini Jr BT, Eisenmann JR., An analytical and experimental investigation of edge delamination in composite laminates. In: Proceedings of the 4th conference fibrous composites, San Diego, CA; November 1978.
  21. Seyhan T., Tanoglu M., Schulte K., Mode I and mode II fracture toughness of E-glass non crimp fabric/carbon nanotube (CNT) modified polymer based composites, Engineering Fracture Mechanics 2008; 75: 5151–5162.
  22. De Volder F. L.M. et al., Carbon Nanotubes: Present and Future Commercial Applications, Science 2013; vol339: 535 – 539
  23. E.T. Thostenson, T.W. Chou, J. Phys. D Appl. Phys. 36 (2003) 573.
  24. Tjong S.C., Structural and mechanical properties of polymer nanocomposites, Materials Science and Engineering 2006; R 53:73–197.

25. Arai M., Noro Y., Sugimoto K., Endo M., Mode I and mode II interlaminar fracture toughness of CFRP laminates toughened by carbon nanofiber interlayer, *Composites Science and Technology* 2008; 68: 516–52.
26. Garcia E.J., Wardle B.L., Hart A.J., Joining prepreg composite interfaces with aligned carbon nanotubes, *Composites: Part A* 2008; 39: 1065–1070.
27. Kepple K.L., Sanborn G.P., Lacasse P.A., Gruenberg K.M., Ready W.J., Improved fracture toughness of carbon fiber composite functionalized with multi walled carbon nanotubes, *CARBON* 2008; 46: 2026 –2033.
28. Godara A., Mezzo L., Luizi F., Warriar A., Lomov S.V., van Vuure A.W., Gorbatiikh L., Moldenaers P., Verpoest I., Influence of carbon nanotube reinforcement on the processing and the mechanical behavior of carbon fiber/epoxy composites, *Carbon* 2009; 47: 2914-2923.
29. Thakre P.R., Lagoudas D.C., Riddick J.C., Gates T.S., Frankland S.J.V., Ratcliffe J.G., Zhu J. and Barrera E.V., Investigation of the effect of single wall carbon nanotubes on interlaminar fracture toughness of woven carbon fiber–epoxy composites, *Journal of Composite Materials* 2011; 45(10): 1091–1107.
30. Davis D.C., Wilkerson J.W., Zhu J., Hadjiev V.G., A strategy for improving mechanical properties of a fiber reinforced epoxy composite using functionalized carbon nanotubes, *Composites Science and Technology* 2011; vol. 71: 1089-1097.
31. Williams J., Graddage N., Rahatekar S., Effects of plasma modified carbon nanotube interlaminar coating on crack propagation in glass epoxy composites, *Composites: Part A* 2013; 54: 173–181.
32. Lyashenko T., Lerman N., Wolf A., Harel H., Marom G., Improved Mode II delamination fracture toughness of composite materials by selective placement of protein-surface treated CNT, *Composites Science and Technology* 2013; 85: 29–35.
33. Avalon S.C., Donaldson S.L., Strength of composite angle brackets with multiple geometries and nanofiber-enhanced resins. *Journal of Composite Materials* 2010; 45(9):1017–1030
34. Bibo G.A., Hogg P.J., Kemp M., Mechanical characterization of glass- and carbon-fibre-reinforced composites made with non-crimp fabrics, *Composite Science and Technology* 1997; 57: 1221-1241.

35. Arteiro A.J.C., Technology development and structural mechanics of composites built of spread tow thin-ply technology, Ms thesis, University of Porto (UP), 2012.
36. A. Petriccione, D. Annicchiarico, V. Antonucci, M. Giordano, A. Riccio, and F. Scaramuzzino. A stiffness volume averaging based approach to model non-crimp fabric reinforced composites. *Compos Sci Technol*, 72:360–369, 2012
37. Thomas Roure and Philippe Sanial. C-PLY™, a new structural approach to multiaxials in composites. *JEC Composites Magazine*, No68:53–54, October 2011. Special JEC Asia 2011
38. Shin S., Kim R.Y., Kawabe K., Tsai S.W., Experimental studies of thin-ply laminated composites. *Composites Science and Technology* 2007; 67: 996-1008.
39. Innovative technology for carbon and aramid, May 2005 – JEC Magazine #17 Retrieved January 8, 2014 from:  
<http://www.jeccomposites.com/news/composites-news/innovative-technology-carbon-and-aramid>
40. Chormat press release 28,11,2012. Retrieved December 22, 2013 from  
<http://www.chomarat.com/wp-content/uploads/2012/02/chomarat-new-composite-Reinforcement-FRGB-DE.pdf>
41. AS4/8552 Product Data Retrieved March 1, 2012 from:  
[http://www.hexcel.com/Resources/DataSheets/Prepreg-Data-Sheets/8552\\_eu.pdf](http://www.hexcel.com/Resources/DataSheets/Prepreg-Data-Sheets/8552_eu.pdf)
42. G0926 product data retrieved March 1, 2012 from from:  
<http://www.hexcel.com/Resources/DataSheets/Fabrics-Data-Sheets/AH370-5H.pdf>
43. Hunstman Araldite LY 5052 product data retrieved March 1, 2012 from:  
<http://www.aerosol.co.il/files/article/1315851066y66Ws.pdf>
44. Epon 828 product data retrieved February 8, 2013 from from:  
<http://www.momentive.com/Products/TechnicalDataSheet.aspx?id=3942>
45. Nanocyl CNT product data retrieved February 8, 2013 from:  
<http://www.nanocyl.com/en/Products-Solutions/Products/Nanocyl-NC-7000-Thin-Multiwall-Carbon-Nanotubes>
46. Nanocyl EPOCYL product data retrieved February 8, 2013 from:  
<http://www.nanocyl.com/en/Products-Solutions/Products/EPOCYL2>

47. Tsai SW, Nettles AT. Representative test data on bi-angle thin-ply NCF. JEC Compos Mag 2011;68:62–3.
48. Toray T800 prepreg product data retrieved January 15, 2014 from:  
<http://www.toraycfa.com/pdfs/T800HprepregsDataSheet.pdf>
49. Toray T800 tow product data retrieved January 15, 2014 from:  
<http://www.toraycfa.com/pdfs/T800HDataSheet.pdf>
50. Russel A.J., On the Measurement of Mode II Interlaminar Energies., Defense Research Establishment Pacific , Materials Report-82., Department of National Defense, Canada, 1982.
51. Brunner A.J., Experimental aspects of Mode I and Mode II fracture toughness testing of fibre-reinforced polymer-matrix composites, Comput. Methods Appl. Mech. Engrg.2000; 185: 161±172
52. Personal communication with Can Muyan.